DISS. ETH NO. 2193

POLYMERIC OPTICAL FIBRES FOR BIOMEDICAL SENSING

A thesis submitted to attain the degree of

DOCTOR OF SCIENCES of ETH ZURICH

(Dr. sc. ETH Zurich)

presented by

MAREK PIOTR KREHEL

MSc in Technical Physics – Biomedical Engineering,
Wroclaw University of Technology, Poland

born on 20.12.1985

citizen of
Poland

accepted on the recommendation of

Prof. Dr. Gian-Luca Bona examiner
Prof. Dr. Martin Wolf co-examiner

2014

Table of Contents

1. Abstract

In this thesis we focus on the integration of optical fibres in textiles to create wearable sensing systems. In the introduction (Chapter 3) we describe the basics of light guiding in optical fibres and methods of lateral light coupling. Subsequently, a literature review and motivation are presented. Afterwards two main parts can be differentiated. In the first one (Chapters 4, 5) a new method of continuous extrusion of optical fibres and their medical sensing application using photoplethysmography (PPG) is described. In the second part (Chapters 6 and 7) we present an optical fibre based force sensor, and demonstrate its application in respiratory monitoring.

Commercially available optical fibres are not suitable for integration into textiles for two main reasons. These are: low flexibility in bending the fiber and relatively high price. Thus, a new type of Polymeric Optical Fibres (POFs) was developed in Empa St. Gallen. These fibres have enhanced strength and flexibility (0.027 GPa for in-house produced POF vs 2.6-3.5 GPa for commercial POF). Additionally, these optical fibres where produced by means of melt spinning, which increased significantly the production speed (400 m/min) and thus potentially reduce the price of these POFs. Cyclo-olefin polymer (COP) (Zeonor n=1.5) was used as a core material and THV fluoropolymer (THVP, n=1.35) as a cladding. These produced POFs features propagation loss at the level of 9 dB/m at 652 nm. These optical fibres were embroidered into textiles such that out-coupling and in-coupling of light at narrow bends in the fiber was possible and the efficiency was improved by one order of magnitude (0.07 % vs formerly achieved 0.008 %). These flexible POFs served to manufacture a textile-based PPG monitoring system. The sample featuring the best coupling efficiency was used to measure heart rate and oxygen saturation (SpO_2). Obtained results were compared with a hospital standard device and showed very good correlation.

Moreover, the system was adapted to work in reflection mode which makes the sensor more versatile.

In the second part of the thesis we present a new type of polymeric optical fibre for applications in force sensing systems in textile fabrics. The detectable force ranges from 0.05 N to 40 N (applied on 3 cm of fibre length) and can be adjusted beyond these limits. The fibres have attenuation parameters between 0.16 - 0.25 dB/cm at 652 nm and the yield strength ranging from 3.9 to 5.4 MPa. Additionally, these optical fibres where employed to develop a textile-based respiratory sensing system. Fibres with different sensitivity together with different setups were evaluated. The results obtained from the textiles based system were compared with commercial standards and showed good correlation. Furthermore, we showed that such a wearable system is able to differentiate the type of breathing (diaphragmatic, upper costal and mixed) when the sensor is placed at different torso positions.

Overall, we demonstrated that the new types of POFs exhibit great potential in the sensing textile applications. Moreover, the proposed production technique of POFs is fast, and thus the price of the POFs can be lowered, and therefore accepted by the textile industry.

2. Zusammenfassung

In dieser Dissertation konzentrieren wir uns auf die Integration optischer Fasern in Textilien für den Aufbau von tragbaren Messsystemen. In der Einleitung (Kapitel 3) werden die Grundlagen der Lichtleitung in optischen Fasern und die Methoden der lateralen Lichteinkopplung beschrieben. Anschliessend folgen eine Literaturzusammenfassung sowie die Motivation zu dieser Arbeit. Danach kann in zwei Hauptteile unterschieden werden. Im ersten Teil (Kapitel 4 und 5) werden eine neue Methode der kontinuierlichen Extrusion von optischen Fasern und ihre medizinischen Messanwendungen mit Photoplethysmografie (PPG) beschrieben. Im zweiten Teil (Kapitel 6 und7) wird ein Kraftsensor basierend auf optischen Fasern präsentiert und mit seiner Anwendung in der Atmungsüberwachung demonstriert.

Kommerziell erhältliche optische Fasern sind durch zwei Hauptgründe nicht geeignet für die Einbettung in Textilien: Diese sind die geringe Flexibilität der Fasern und der relativ hohe Preis. Daher wurden neue polymere optische Fasern (POF) an der Empa St. Gallen entwickelt. Diese Fasern haben eine erhöhte Festigkeit und Biegsamkeit (0.027 GPa für intern produzierte POF im Vergleich zu kommerziellen POF mit 2.6-3.5 GPa).

Zusätzlich werden diese optischen Fasern durch Schmelzspinnen produziert, was die Produktionsgeschwindigkeit (400 m/min) signifikant erhöht und dadurch den Preis dieser POFs potentiell reduziert. Ein cycloolefinisches Polymer (COP) (Zeonor, n=1.5) wurde als Kern benutzt und ein THV-Fluoropolymer (THVP, n=1.35) als Mantel. Diese produzierten POFs zeigten eine Lichtdämpfung in der Grössenordnung von 9 dB/m für eine Wellenlänge von 652 nm. Diese optischen Fasern wurden dafür in Textilien eingestickt, sodass das Aus- und Einkoppeln von Licht an engen Krümmungen möglich war und die Effizienz um eine Grössenordnung gesteigert wurde (0.07 % verglichen mit zuvor erhaltenen 0.008 %). Diese flexiblen POFs dienten der Fabrikation eines textilbasierten

PPG-Überwachungssystem. Die Probe mit der besten Kopplungseffizienz wurde für Messungen der Herzrate und Sauerstoffsättigung (SpO2) benutzt. Resultate wurden mit einem herkömmlichen Krankenhausmodell verglichen und zeigten eine sehr gute Korrelation. Weiterhin wurde das System auf eine Benutzung im Reflektionsmodus angepasst welches den Sensor breiter einsetzbar macht.

Im zweiten Kapitel der Dissertation wird eine neue Art polymerer optischer Faser für Anwendungen im Bereich textiler Kraftsensorsysteme vorgestellt. Die detektierbaren Kräfte spannen von 0.05 bis 40 N (belastet auf einer Faserlänge von 3 cm) und kann über diese Grenzen angepasst werden. Die Fasern zeigten einen Dämpfungskoeffizienten von 0.16-0.25 dB/cm bei 652 nm und eine Streckgrenze zwischen 3.9-5.4 MPa. Zudem wurden diese Fasern für die Entwicklung eines textilbasierten Atmungssensorsystems benutzt. Fasern mit variierender Sensitivität und in verschieden Aufbauten wurden ausgewertet. Die Resultate des textilbasierten Systems wurden mit kommerziellen Standards verglichen und zeigten eine gute Korrelation. Zusätzlich konnten wir zeigen, dass ein solches tragbares System zwischen verschiedenen Atmungsarten (Zwerchfell-, Brust- und Bauchatmung) über die Positionierung des Sensors unterscheiden kann.

Insgesamt haben wir demonstriert dass die neuen Arten POFs grosses Potential für textile Messsysteme bergen. Zudem ist die vorgeschlagene Produktionsweise der POFs schnell und somit kostengünstiger. Dies erhöht die Akzeptanz in der Textilindustrie.

3. Introduction

In this thesis we focus on optical fibre based sensors. The sensing in our system is relays on light out-coupling from the POFs. Therefore, it is essential understand basic of light guiding and light coupling in the optical fibres.

3.1 Refraction and Light Guiding Principles

3.1.1 Light Refraction.

Light refraction is a change in direction of a light wave connected to its velocity change, when it changes propagation medium. This change is caused by a change in wavelength while the frequency stays the same. Thus the speed of the light in media with different refractive indices is as following [1]:

$$\boldsymbol{v_1 = \frac{c}{n_1}, v_2 = \frac{c}{n_2}} \quad (1)$$

Where c is the speed of light in vacuum, v1 and v2 are the speed of the light in propagation media, and n_1 and n_2 are refractive indices.

- Snell's Law

The time of the journey of the light is equal to distance traveled divided by the speed:

$$\boldsymbol{T = \frac{d_1}{v_1} + \frac{d_2}{v_2}} \quad (2)$$

As shown in Figure 1 and from Pythagorean's theorem it can be observed that:

$$T = \frac{\sqrt{x^2 + a^2}}{v_1} + \frac{\sqrt{b^2 + (l - x)^2}}{v_2} \qquad (3)$$

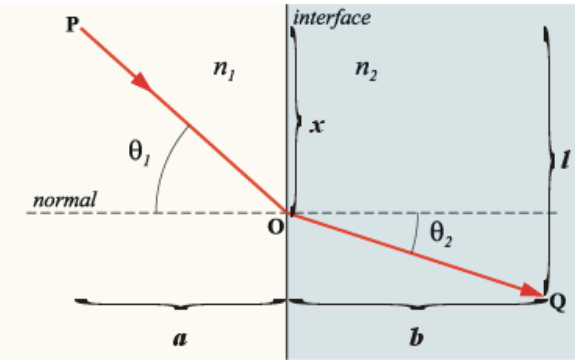

Figure 1. Derivation of refraction law/Snell's law. Used with permission from Ref. [2].

Fermat's Principle states that the light path between two points is the path that can be traveled within the least time [3]. Appling this to the equation (3) means that the derivative with respect to x must be equal to zero:

$$\frac{dT}{dx} = \frac{x}{v_1\sqrt{x^2 + a^2}} + \frac{-(l - x)}{v_2\sqrt{(l - x)^2 + b^2}} = 0 \qquad (4)$$

From Figure 1 and equation (4) it can be observed that:

$$\frac{dT}{dx} = \frac{sin\theta_1}{v_1} - \frac{sin\theta_2}{v_2} = 0 \qquad (5)$$

And thus we obtain a relation of refractive indices and the incidence angles:

$$n_1 sin\theta_1 = n_2 sin\theta_2 \qquad (6)$$

3.1.2 Total Internal Reflection and Critical Angle

The critical angle can be defined as an angle above which all the light will be reflected back and total internal reflection occurs. If a light ray that travels in an optically transparent medium with a refractive index n_1 encounters the other optical medium with different refractive index n2, refraction (as described in chapter 3.1.1) takes place (schematically presented in Figure 2a) and the light ray will change its direction of propagation. Assuming that n1 is greater than n2 the light ray would need to escape with an angle equal to 90º (Figure 2b). Including this angle value to the equation (6) the following equation for critical angle can be obtained:

$$\boldsymbol{\theta_c = arcsin\left(\frac{n_1}{n_2}\right)} \qquad (7)$$

All lightincident above the angle calculated from equation (7) will be back reflected and total internal reflection will occur, as presented in Figure 2c.

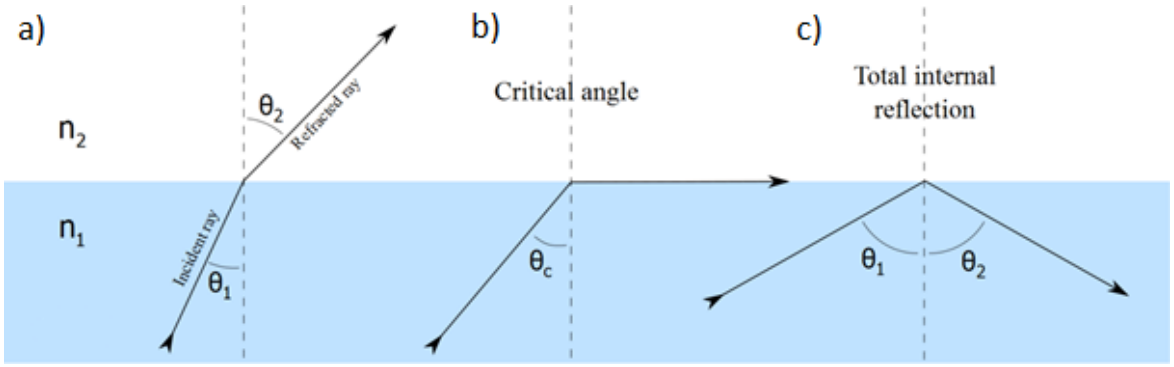

Figure 2. Refraction, critical angle and total internal reflection. Used with permission from Ref. [4]

- Optical fibres

Optical fibres utilise the total internal reflection effect. The light can be trapped inside the optical fibre when it is directed into the fibre within the acceptance angle. When the light is

directed into the optical fibre it will be firstly refracted and certain light rays will propagate above the critical angle and thus will be trapped within the core optical fibre. This phenomenon is schematically presented in Figure 3.

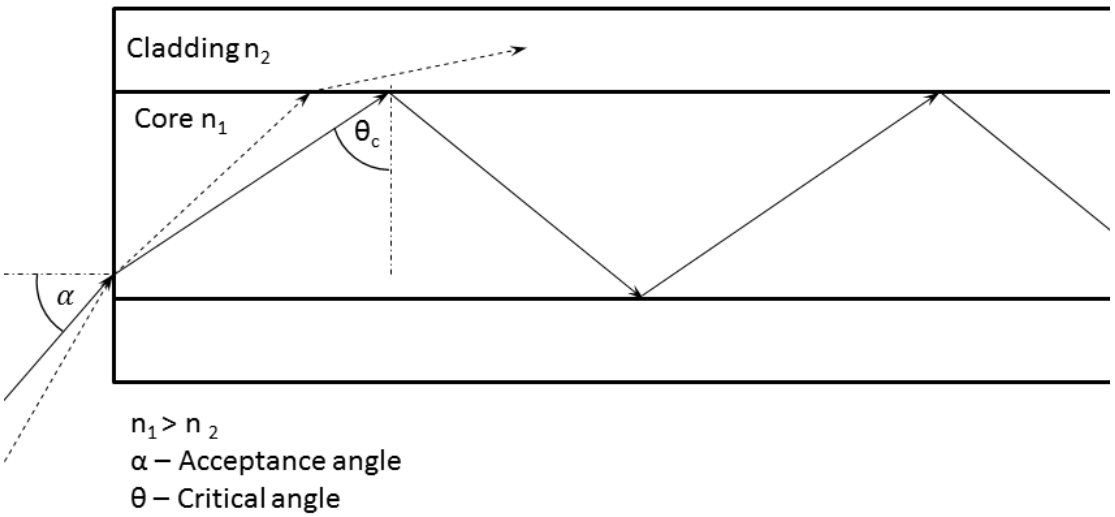

Figure 3. Sketch presenting idea of acceptance and critical angle. Light propagation in the optical fibre.

Optical fibre consists of core (with higher refractive index) and cladding (with a lower refractive index). Placing cladding on top of core optical fibres has a multiple functions. Firstly it gives the possibility to manipulate the acceptance angle. The other important reason is the protection of the core (from dust, scratches, etc.) where the light guiding takes place. Claddings can be also used to allow only one mode to propagate in the optical fibre and form so called single mode optical fibres. Examples of other specialty optical fibres are graded index optical fibres, photonic fibres and hollow core optical fibres[1].

[1] Speciality optical fibres are not considered in this report for details please consider ref [5].

- Light Attenuation Sources

When light travels inside the optical waveguide its signal is continuously attenuated. This attenuation or so called optical light losses can be separated into two main types. The first, intrinsic losses, come from material properties and are process independent. There are many sources of intrinsic losses for example light scattering and absorption by harmonics of hydrogen atoms. There are a huge amount of sources of extrinsic light losses. They can originate from impurities, irregularities, cracks, air bubbles, bends, etc, all of which can refract the light out of the core.

3.2 Light Coupling from Optical Fibres

In this work, mechanisms of extrinsic losses were used for light coupling in and out from the optical fibres. Two light coupling mechanisms were studied. The first is schematically presented in Figure 4. In this scenario the optical fibre underwent mechanical perforation (cladding and core). The light that traveled within the acceptance angle inside the optical fibre encountered the irregularities and the light was either reflected at the angle that exceed the acceptance cone (red light path) or it encountered the roughened surface above critical angle and thus was outcoupled from the waveguide.

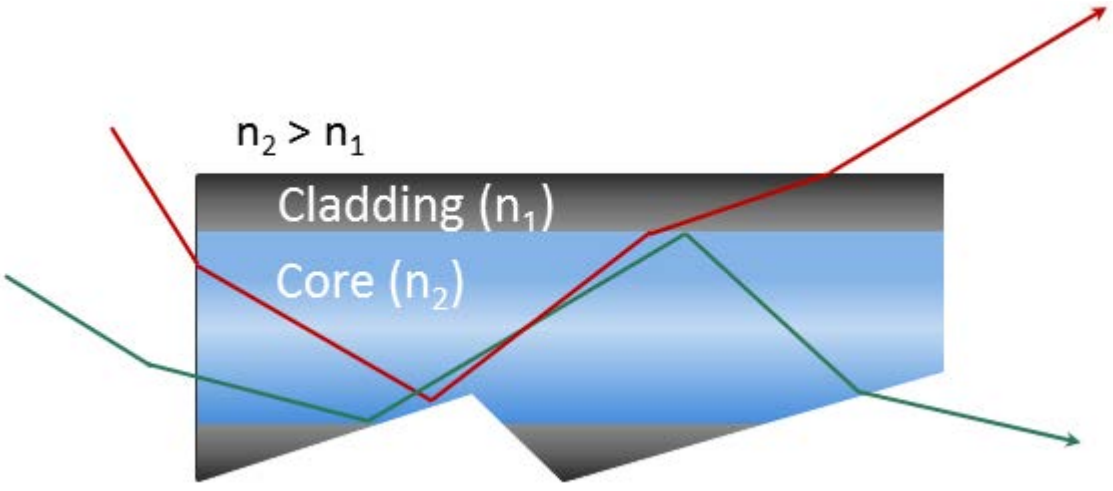

Figure 4. Schematic drawing for light coupling by a rough surface.

The second scenario regarding coupling light in optical fibres that was studied relied on bending the fibres with a very small radius (r = 150-200 µm). In such a situation light rays can be guided out of the waveguide (red light pathway in Figure 5) due to the same reason as the green light pathway in Figure 4 (the light ray encounters the bent border of the optical fibre above acceptance angle).

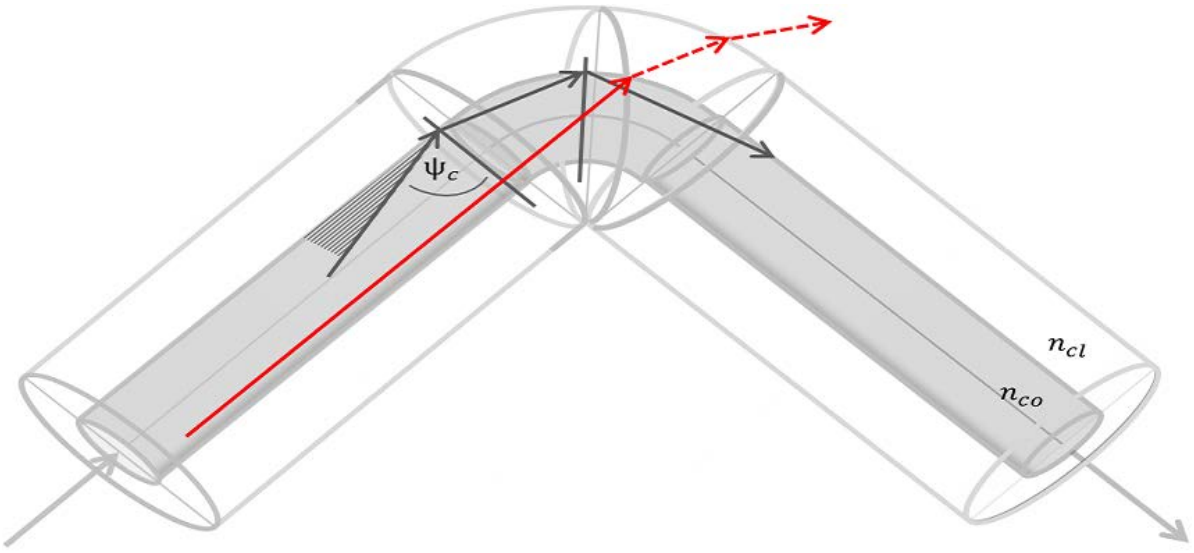

Figure 5. Schematic drawing that presents light coupling by bending. The red light ray is out-coupled due to the small bending radius. The dark grey light ray is still guided in the fibre. To be published.

If one considers the light ray travelling in the opposite direction to the one that was out coupled, it will be coupled into the optical fibre and trapped inside.

3.3 Existing Optical Fibre Based Biomedical Sensing Systems.

Optical fibres have been used in numerous biomedical sensing systems. This is due to their small size, flexibility and immunity to electromagnetic radiation [5, 6]. Numerous applications can be found in the existing literature. However, most of them are not close to application either due to the sophisticated electronic that highly elevates the costs or due to

the small signal to noise ratio. The systems that have overcome those problems and are close to application system can measure various vital parameters. This includes skin temperature, breathing rate and volume, heart rate and blood pressure [7, 8]. Additionally blood oxygenation (described in chapter 7) as well as perfusion (velocity and concentration of erythrocytes) [9, 10]. Monitoring of human body movement is also well documented. Researchers were also able to monitor the wound healing process. This indirect measurement could be conducted by means of assessing sweat, humidity and pH values [11-13]. In the following paragraphs the techniques that are in their most advanced stage are discussed in more detail.

3.3.1 Monitoring of Respiration and Oxygen Saturation

- Respiration monitoring

One very important task in healthcare patient monitoring is respiration control. The automatic act of breathing is controlled by the medulla oblongata with other automatic functions [14]. The medulla oblongata, in its respiratory duty, controls the respiratory rate and the amount of inhaled air based on the amount of oxygen, carbon dioxide and carbon oxide in the blood. The other parameter that can be measured by means of respiratory rate monitor is the psychophysiological state of the patient [15] e.g. deep and long breath together with a reduced level of skin conductivity indicate the patient is relaxed. Thus the respiratory monitoring is of great importance in critical and neonatal care. The next application is monitoring respiration during sleep in order to assess the sleep apnea syndrome. Patients suffering from this syndrome demonstrate episodes of shallow and irregular breathing during sleep. The sleep apnea syndrome causes effects such as slower reaction time, vision problems, fatigue and excessive daytime sleepiness. It may be unnoticed by patients for years. An important requirement for the sleep supervision is that it can distinguish between rollover / sleep movement effects and the respiration.

Two independent, optical fibres based, systems were used for respiration monitoring. The first of them employed analysis of Photoplethysmography (PPG) signals. PPG is a plethysmogram that was optically acquired from a measured organ. A widely used example is pulseoximetry where changes in light absorption are used to measure heart rate and blood oxygenation. The PPG signal contains two components. AC which corresponds to changes in blood volume and blood flow, and DC which reflects the total blood volume and light scaterring. Variations in these signals can be used to extract respiration values [17].

The second system uses microstructure optical fibres that are highly sensitive to applied strain [18]. Examples of this system are: Optical Time Domain Reflectometry (OTDR), Optical Frequency Domain Reflectometry (OFDR), and Fibre Bragg Gratings sensors (FBG) [19]. M. Nishyama *et al.* proposed a system where sensors were built with single mode optical fibres, and thus less affected by external factors. Therefore it functioned independent of temperature variations [18]. Another example of breathing monitoring is the European project OFSETH. Within this project a textile to measure costal and abdominal movements was developed. Several configurations were evaluated: macro bending, FBG sensors and OTDR sensors [19, 20]. The best correlation was present in the OTDR sensor systems. In macro bending systems mode coupling interfered with the results. FBG sensors on the other hand showed shifts in wavelength related to stress present from embedding into the textile.

- Oxygen Saturation

Oxygen is essential for human beings, when it is inhaled to the lungs it is delivered to the blood, which transports it to all organs. Blood gas measurements can provide crucial oxygen content information. One way of assessment of blood gas content is taking an arterial blood sample from a patient and performing arterial blood gas (ABG)

measurements with blood gas analyzer. Modern gas analyzers can provide information on pH, carbon dioxide, hemoglobin, bilirubin and other important parameters[21]. Nevertheless, measurements conducted with these apparati deliver only information about the patient's status at the time when the blood sample was taken. Consequently, a continuous measurement of oxygenation is impossible with ABG devices and thus the information regarding changes in blood oxygenation might be noticed too late in some situation. Pulse oximeters, on the other hand, are devices that are able to continuous measure the amount of oxygenated hemoglobin in blood by means of absorption measurements.

The first optical measurements of oxygen saturation were reported by the German physician, Karl Matthens. To conduct the measurements he used red and green filters[22].

Between 1930s-1940s a method called "bloodless zero" was attempted in order to conduct first absolute measurements. This concept relayed on evacuating all blood from the tissue under test (in this situation ear lobe). Once the blood was not anymore present in the tissue the light intensity was measured. Afterwards, when the blood was present in arteries the next measurement was taken.[23] The Waters Company was one of the first companies that successfully employed the bloodless method. Their system relied on emptying the tissue by means of an inflatable cuff. Currently used pulse oximetry does not employ this technique since it takes advantage of the arterial blood pulsation. Between 1960s and 1970s Hewlett Packard developed first oximeter for which one did not have to obtain bloodless state. This self-calibrating system required measurement at 8 wavelengths [23]. In 1970s a Japanese researcher, Takuo Aoyagi, was working on a method to assess the cardiac output by employing cardiogreen dye and a light absorption trough an ear. He noticed that light absorption varies accordingly to the pulsation, this made it impossible to measure cardiac output. However, he realised that this behavior can be used to estimate the arterial blood

oxygenation[24]. Simultaneously another other Japanese researcher was developing a similar system which led to a patent approval in the USA. Substantial improvements towards two wavelengths pulse oximetry were performed by the company Biox Corporation. They decided to use red and infrared LEDs for measurements and directed their devices for the medical use.

Nowadays most of the pulse oximeters measure the arterial oxygen saturation (SpO_2) by means of ratio of absorptions at two wavelengths. Afterwards the modified Beer-Lambert law is employed to estimate the SpO_2 [25]. Normally these absorption values are measured in transmission, thus only parts of the body such as fingers, toes, and earlobes can be used for measurements. Reflection mode systems exist, but are under development, and due to huge differences in LED power and AC/DC relations they have to be adapted [26].

- Limitations

One limitation of pulse oximeters are motion artefacts: as they may influence the measurements, when a patient moves the part of his body on which the pulse oximeter was attached because the amount of blood in arteries will vary. This in turn can be misinterpreted by the device as pulsatile and lead to improper estimation of SpO_2 and a heart rate [27]. Nowadays, pulse oximeters are considerably motion artefact resistant by usage of accelerometers or algorithms [28]. Other parameters that hinders the application of SpO_2 devices is low perfusion, as it is crucial factor for measuring the arterial oxygen level. Since the pulse oximeter devices need to differentiate the pulsatile from nonpulsatile components, it can become impossible when low perfusion.

It was found that the presence of MetHb can influence SpO_2 values as well. Particularly high levels of MetHb caused an overestimation of SpO_2 level. Therefore, the SpO_2 values should be read with attention while MetHb may be present[29]. Similar overestimation effects can be caused by Carbooxyhemoglobin (COHb). Barker et. al, conducted

experiments of dogs in which the COHb level was raised up to 70%, during this time the pulse oximeters showed value of 90 % while the actual O2Hb was below 30%.[30]

- Medical significance

Besides all the limitations mentioned above, pulse oximeters attracted a lot of attention in the last decades. Its acceptance was mostly possible as a result of development in the other fields of technology. For instance new light sources/detector, microprocessors, data processing and sensors design. Nowadays, pulse oximeters are of wiedly use and can be find virtually in every live threatening situation, for instance in: intensive care units, neonatal care, medical transportation, diagnostic, home care and others.

3.3.2 Human Vital Values – Heartbeat, Heart Rate, Blood Flow Velocity, Cardiac Output, Blood Pressure, Perfusion.

Contraction of the heart muscle, also called the cardiac cycle, or heartbeat, together with its frequency is a very significant indicator of human health. The human heart acts as a pump for whole blood circulation system and ensures that blood is delivered to all organs. The pulse provides information about human body condition, it rises when sport are performed or when stressful situations occur. The other important parameter of the cardiac cycle is how much blood can be pumped in one ‘stroke’ of the heart, indicating the ‘strength’ of the heartbeat. Under regular circumstances cardiac output is approximately 5.6 liters.min^{-1} for males and 4.9 liters.min^{-1} for females [31, 32]. This value can be reduced due to for instance cardiovascular diseases. Monitoring of the pulse and the heartbeat can be performed with PPG analysis [26, 33]. These parameters could also be used to detect sleep apnea [33]. Devices that measure the signal in ears have the advantage of functioning even when blood is absent from the extremities (fingers, toes, etc.) and therefore attract a lot of attention [26].

When discussing pulsation measurements one has to point out an interesting difference between electrical and optical measurements. Electrical measurements produce the value without any delay, however while performing optical measurements and collecting PPG signals one measures values that corresponds to pulse rate but not to heart rate [34]. When measuring PPG signals, on for instance a toe and a finger, different delay times should be observed. This effect can be employed to estimate blood flow velocity as a function of distance between measurement points [35]. Measurements of cardiac output are not as straightforward as the heartbeat measurement. However, it can be estimated from PPG signals using a method called pulse contour, which was for the first time proposed in 1904 by Erlanger J. *et al.* [31, 36].

Blood Pressure (BP) is one of the main vital parameters. It refers to two numbers: the first , a maximum, 'systolic' value and the second, the minimum diastolic value. Normal blood pressure values differ depending on gender, age, fitness state, emotional state, environmental factors, etc. However, relative values have been established for all of the above mentioned subgroups, and thus it is possible to use these values for physiological state evaluation [37]. In standard sphygmomanometer (cuff measurement take on the upper arm) blood pressure is found by acoustical evaluation with a stethoscope. At first a total occlusion has to be applied and the blood flow stops, subsequently the pressure is decreased and the blood starts to flow, which corresponds to systolic value. This leads to acoustic signs. The lower value, when the blood fully flows and no acoustical signs can be detected, corresponds to the diastolic pressure. The Pulse Pressure (PP) is the difference between systolic and diastolic value. The PP number is straight forward correlated to the strength of the heartbeat (cardiac output). Researchers were able to prove that PP values have a connection with heart attacks [38]. In order to compete with currently existing devices, the newly developed devices have to be at a level of at least similar accuracy and

better comfort which would allow long term monitoring. The required accuracy is defined by the Association for the Advancement of Medical Instrumentation (AAMI). The higher comfort could be achieved by developing a device which would not require a cuff. Fortino and Giampà describe two PPG based systems for noninvasive and continuous BP measurements [39]. These systems can be categorised into pure PPG based methods [40, 41] and systems that require simultaneous measurements of PPG and electrocardiography (ECG) [42]. In one of the PPG based systems it was proposed that blood pressure can estimated from pulse wave velocity (PWV) by means of circulatory waveform signal measured from two PPG sensors placed at a known distance (see Figure 6) [39].

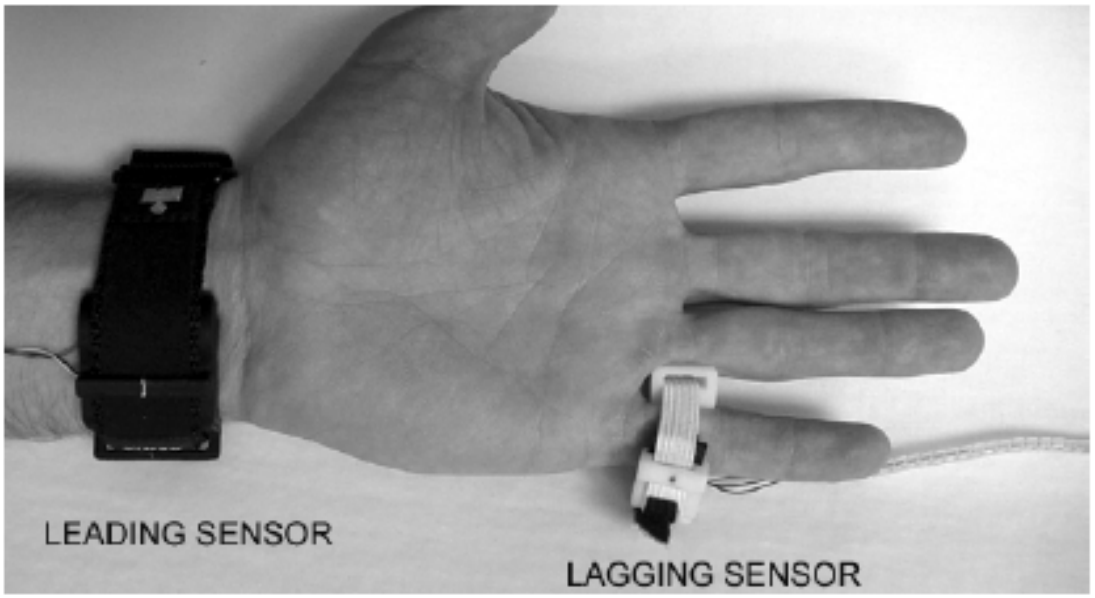

Figure 6. PPG Sensor with positioning to measure the PWV. Used with permission from ref. [39].

In the second system, which requires measurements of PPG and ECG simultaneously the advantage from the linear relationship between pulse wave transfer time (PWTT) and BP was taken (PWTT is inversely proportional to BP) [43]. PWWT can be defined between two points on ECG and PPG, which is the R peak of the ECG signal and the minimum point of the PPG waveform as schematically presented in Figure 7.

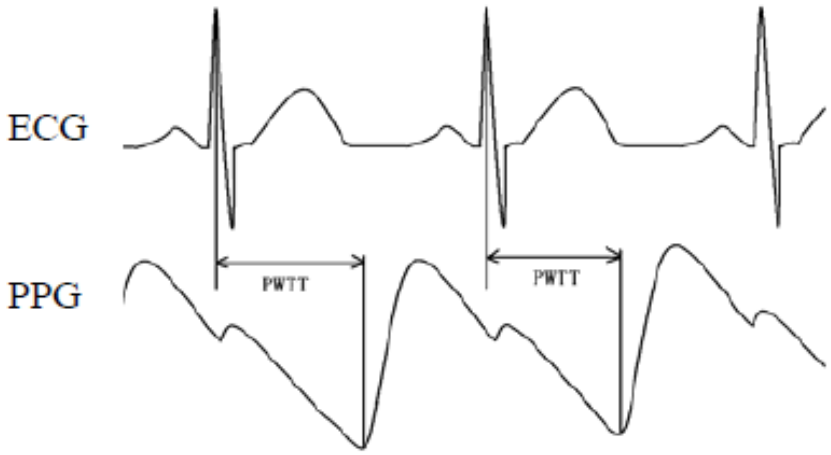

Figure 7. The description of PWWT that can be used for blood pressure estimation. Used with permission from ref. [43].

3.3.3 Pressure on tissue – decubitus ulcers prevention

Decubitus ulcers (also named as pressure ulcers or bedsores) are dangerous wounds occurring as a consequence of friction from long time applied pressure. Human tissue can tolerate high pressures but an extended time of inhomogeneous blood supply can cause degradation of tissue which leads to the occurrence of wounds. The other potential danger that is mentioned in the literature is the occlusion of the lymphatic system [44]. Values of 4.3 kPa were proposed as characteristic capillary blood pressure that microvasculature can resist the external pressure while maintaining the supply of oxygen and nutrients [44].

The origin of the pressure wounds is not fully understood yet, thus mechanisms that can cause pressure ulcers are studied. One of the approaches is to map the pressure distribution to give an overview which areas of the human body are endangered. It has been reported that paraplegic patients distribute their weight with pressure points that are placed on tier convexities, and since they are do not feel pain lack of oxygen can be undetected. The lack of oxygen in turn can be a reason for decubitus ulcers [45-47]. Therefore a continuous, long term monitoring is of a great importance. Additionally, real time measurements of blood flow is can be helpful to ensure healing of existing wounds [48].

Techniques such as PPG, Laser Doppler Flowmetry (LDF) and Near Infrared Spectroscopy (NIRS) were reported as useful for blood flow assessment [9]. Thanks to these methods one can assess whether the applied pressure hinders the blood flow. PPG utilizes AC and DC parts of the signal. AC signals change with the change of pulsatile and pressure differences, while DC gives the overview of total amount of blood. Measurement depth can be easily adapted by changes of the wavelength used for the measurement and adjustment of the distance between light source and detector [9]. Even though it is not proven that obesity increases risk of ulcers, it is clear that extraordinary weight increases pressure. Thus, additional risk assessment can be obtained from the patients' weight.[45].

FBGs are a type of reflector which selectively reflects wavelengths. This happens due to the Bragg reflector inside of optical fibre (periodic changes of refractive index). Reflected wavelength changes together with to changed geometry, and thus can be employed for pressure or strain measurements FBGs. A matrix of crossing of optical fibres along with parallel strands of sensors have been reported [49]. However, depending on the material in which the FBGs where embedded, different hysteresis shape can be observed [50]. Besides the FBGs two other main systems are in use, in this systems measurements relies on intensity or phase modulation. In the intensity based system light losses induced by pressure are measured. Phase modulated systems measure the applied force by means of interferometric effects that take place inside of the optical fibre [51].

The measurement system for monitoring the paraplegic patients has to be soft, flexible and with good haptic, not to cause decubitus ulcers itself [52]. Therefore optical fibre based systems fit very well, as they are small in size can be flexible – particularly polymeric ones. Moreover, they are immune to electromagnetic fields which is of high importance in hospitals, where strong electromagnetic fields are present.

3.3.4 Wearable monitoring devices

In order to perform long term monitoring of human vital parameters, the wearability / comfort of the measurement system should be very high, and thus textile based wearable systems with enhanced haptics are a perfect fit. It is also of great importance in sport performance measurements where uncomfortable devices would hinder the activity [53]. Taken together, comfort is a very important criterion since even a very reliable sensor, can be rejected due to discomfort. Therefore, an efficient way of introduction of optical fibres into the textiles is essential. Sensing systems produced with optical fibres are light weight, water and corrosion resistant, and feature enhanced haptic. To maintain high comfort, factors such as fibre thickness, evenness and the number of faults are crucial [54]. However one has to keep in mind that parameters such as the numbers of loops, wavelength, and the length of the textile can decrease the signal quality due to light losses. When optical fibres are used in garments for sensing they have to contact the skin to deliver the light to the human tissue. The intensity of the emitted light from the garment is another important parameter of luminous textiles. Parameters such as the type of carrier fabric, thickness of optical fibres, method of integration into textile, textile curvature and a power of a light source play an important role [55, 56]. Additionally, heat and pressure treatment to textiles with integrated polymeric optical fibres can be applied to vary the light out coupling properties. Sandblasting and chemical treatment was also applied to increase the lateral light coupling [57]. Taken together, a vast number of parameters have an influence on wearability of the the monitoring devices and they have be thoroughly studied prior to design.

3.4 Scope of the thesis

Optical fibre based health monitoring systems integrated in textiles are an increasing field of research. This is due to their advantages over intrusive measurements, such as high wearing comfort and thus the possibility of long term monitoring. As described in the Chapter 3.3.1 a vast number of human vital parameters can be measured or at least estimated by analysis of the PPG signal. However, most of the existing systems operate in transmission mode, thus limiting the measurements to places such as fingers, ear lobes or toes. It is not only the comfort that is affected when working in transmission mode, but also the reliability of the measurement itself. In extreme conditions blood supply to extremities can be affected. Thus it might be impossible to obtain a PPG signal. Therefore usage of reflective mode systems is required. Moreover, to perform long term monitoring, high comfort has to be sustained. This can be obtained with optical fibres integrated into textiles. However, most of the existing optical fibres, even polymeric ones, are not flexible enough for integration into textiles with industrial stitching machines. Additionally their relatively high price hinders usage by the textile industry. Hence in the first part of this work a new method of the production of optical fibres is described. In Chapter 4 we intended to produce the optical fibres with continues extrusion method in order to make them relatively cheap and thus acceptable by textile industries. The other challenge that researchers have faced while integrating optical fibres into textiles is their flexibility. Thus, we propose the extrusion of the fibres out of new, more flexible, polymers thanks to which it is possible to integrate them in the textile.

In Chapter 3.3.3 the importance of tissue pressure monitoring in the prevention of decubitus ulcers is described. Most of the systems that could monitor the pressure or force on tissues are rigid and cause decubitus ulcers themselves. Therefore, we aimed to develop a sensing system that would not leave relevant pressure marks on the human tissue. In

order to manufacture such a system we developed, an extremely flexible force sensing POF. This optical fibre was extruded from block copolymer of soft part Polydimethylsiloxane (PDMS) and hard part Polyurethane (PU). Thanks to the flexibility of these sensing optical fibers they do not cause pressure ulcers themselves. Moreover, it allowed us to integrate them into textiles.

In the subsection respiratory monitoring of Chapter 3.3.1 we explained the significance of measurements of human breathing system. It was also described that long term monitoring is of a great importance, however currently existing system are of very low comfort and thus not favorably used by patients for a long term. Thus, a medical textile that features the haptic of regular textiles was developed. This wearable system, described in Chapter 6, was developed by means of the flexible POFs developed force sensing applications. Additionally in Chapter 7 another feature of this system is reported – respiratory rate monitoring with this fibre incorporated into textiles.

4. Production of Optical Fibres and Production with Spider Plant Method.

There are two main processes of production of polymeric optical fibres: continues extrusion and drawing process. Continues extrusion process is used for production of step index optical fibres since the core of the waveguides is relatively large and thus variations in manufacturing methods are not crucial. Specialised optical fibres (graded index, single mode and photonics fibres) are mostly produced by drawing a prefabricated preform since in this system production parameters can be better controlled [58]. Since this reportes do not cover the second types of the optical fibres producing and drawing a preform is not described here and can be found elsewhere [58].

4.1 Continues Extrusion of Optical Fibres.

In Figure 8 the continues extrusion process is presented. Materials are supplied into the reaction chamber (top left part) where the monomers are polymerized. Afterwards the polymer, as a thick fluid, is extruded. On the right side of Figure 8, a similar system with simultaneous cladding deposition is presented. Continues extrusion is a very economical method due to the capability to produce high volumes in a short period of time. One disadvantage of this system is the difficulty to control the polymerization reaction in such a system, hence not all the monomers are fully polymerized. Therefore large quantities of monomers can still be present in the end product. Where remaining monomers are not desired, melt spinning systems should be used.

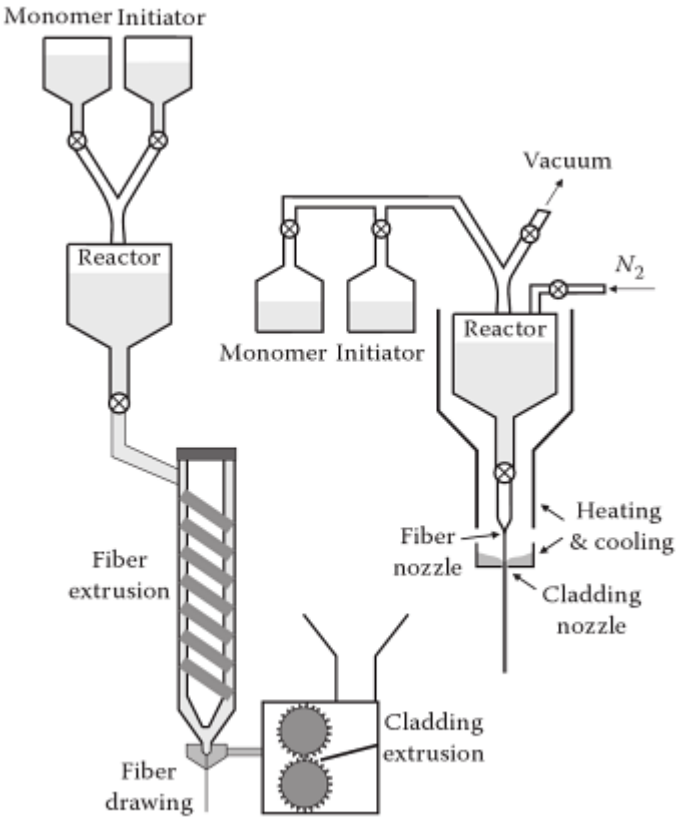

Figure 8. Continues extrusion process. Adapted from ref. [59] with permission of the American Institute of Physics.

- Melt spinning

The extrusion of polymers that were heated and melted under friction in the screw extruder, followed by pressing through the spinneret to form a filament can be defined as melt spinning extrusion. This kind of fibre extrusion has a couple of advantages over other available systems. As mentioned above, the direct use of polymers avoids the occurrence of monomers in the end product. In Figure 9, such a continues extrusion plant capable to extrude a wide variety of commercially available polymers is presented. Thanks to that, the commercial polymers in form of granulates are fed into the screw or piston extruder (top part of Figure 9) and thus there is no need to control any kind of polymerization reaction. Moreover, since the material was polymerized in commercial plants no or only traces of monomer leftovers are present in the starting material. Additionally, two screw extruders can be combined with a specially prepared spinneret such that the production of bi-component fibers is possible.

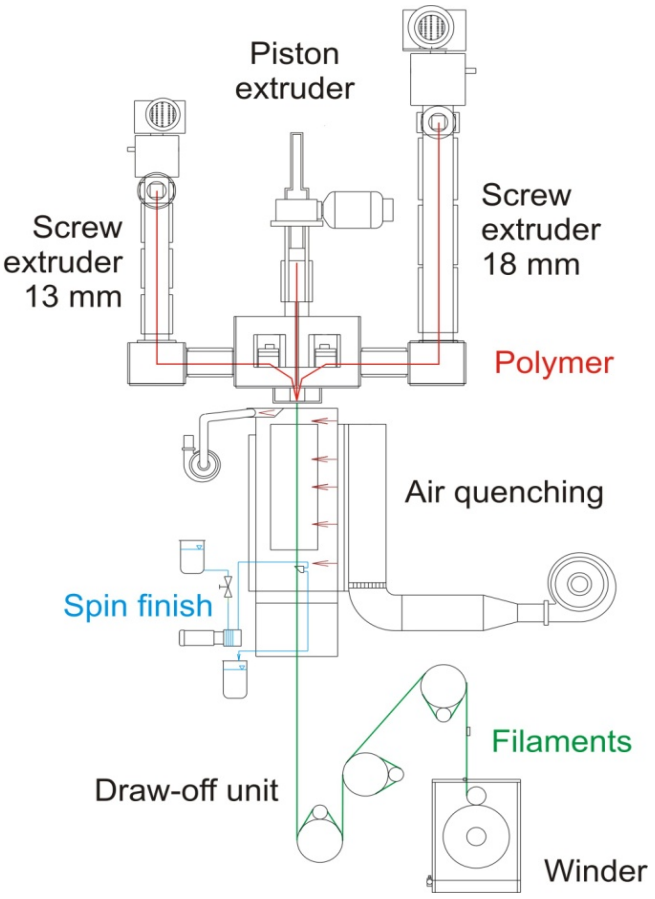

Figure 9. Sketch of bicomponent melt spinning plant developed at Empa St. Gallen.

In Figure 10 a sketch of the spinneret used for our extrusion experiments. On top of this drawing two separate inputs for the melted polymers are presented. Once the polymers flow through the channels of the die, they form bi-component fibres consisting a core-sheath geometry. The extrusion of bi-component filaments was the basis to form optical fibres in a very fast and efficient way. However, the two polymers have to be chosen with great caution.

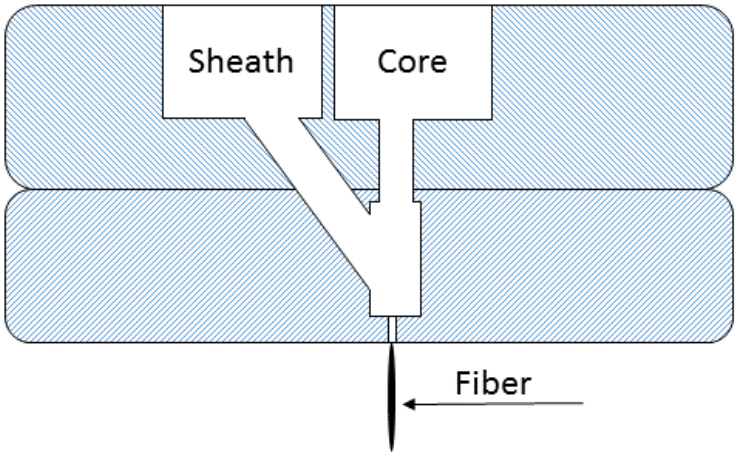

Figure 10. Sketch of the spinneret used to extrude bi-component fiber.

- Polymers

A wide variety of polymers are known to be processable by melt spinning plants. According to [60], these can be for instance PET polyester, PEN polyester, polystyrene, polyurethane and others. However, these polymers are not suited to produce optical fibres. In order to produce good quality optical fibres, the polymers need to resist the high processing temperatures without getting neither oxidized nor decomposed. The resulting hazy or yellowish appearance after oxidation or decomposition would significantly decrease the light transmitance. Secondly, to employ them in textiles the polymeric fibres need to tolerate the increased washing temperature. Furthermore, they should not be hygroscopic. Moreover, they need to feature a higher flexibility to withstand the high forces while being integrated into the textile (e.g. embroidery). Additionally, since in our system two different polymer materials are combined in the dye as a liquid, the processing temperature of these materials should be in the same range. The most important prerequisite for light guiding applications, is the fact that they have to be optically transparent and the refractive index of the core polymer has to be higher than of the polymer used as cladding (condition for light guiding described in Chapter 3.1). Lastly, a

high difference in refractive indices between core and sheath would be advantageous for light coupling (high numerical aperture means easier light coupling).

A commonly used polymer for POFs is polymethyl methacrylate (PMMA), which does not fulfill all of the above mentioned parameters. It can slowly decompose in the presence of water and it is too brittle to use in the textile industry. Cyclo-olefin polymers (COP) do not have these disadvantageous and is there for a very good candidate for the production of optical fibres with melt spinning plant. It is commercially available under the trade name Zeonor®. It shows high transparency in the visible range and has a low water absorption. The good moldability, and suitable high flow properties in the melted state combined with a good temperature and chemical resistance makes it an ideal candidate for the melt processing of optical fibres. Thus, COP was chosen as a core material. For the cladding material, Dyneon THV was used. It has a lower refractive index (1.35 vs 1.5 of Zeonor®), hence it would feature high numerical aperture. Furthermore, similarly to Zeonor®, it repels moisture, has a good resistance to chemicals and, most important, Dyneon THV is processable in melt spinning plants with similar temperatures as Zeonor®. Additionally, the two polymers exhibit good addhesion to each other.

- Process Dependent Light Losses

In order to manufacture the optical fibre with good light transmission parameters, not only the material type is important but also the geometry of the POFs. The system presented in Figure 9 contain three draw-off unit. Rotation speed and temperature of each of these units can be controlled separately. Due to the controllability of the temperature, an annealing process could be performed, and thus a better geometry of the fibres was achieved. The possibility to control the flow of the melted polymers allowed to vary the diameter of the fibres. The diameter and the homogeneity of the fibres were controlled by tuning the draw ratio. By drawing the polymers increases the polymer chains were oriented, which

enhanced the mechanical properties of the produced fibres. However, it can cause crystallinity which would in turn increase light attenuation of the produced POFs. When drawing the optical fibres made of amorphous polymers, one has also to take in consideration that when they undergo high forces micro cracks can occur. These micro cracks cause light scattering, hence increase the light attenuation [61, 62]. These crazes could be observed as parallel cracks in SEM micrograph surface of white fibre (presented in Figure 11).

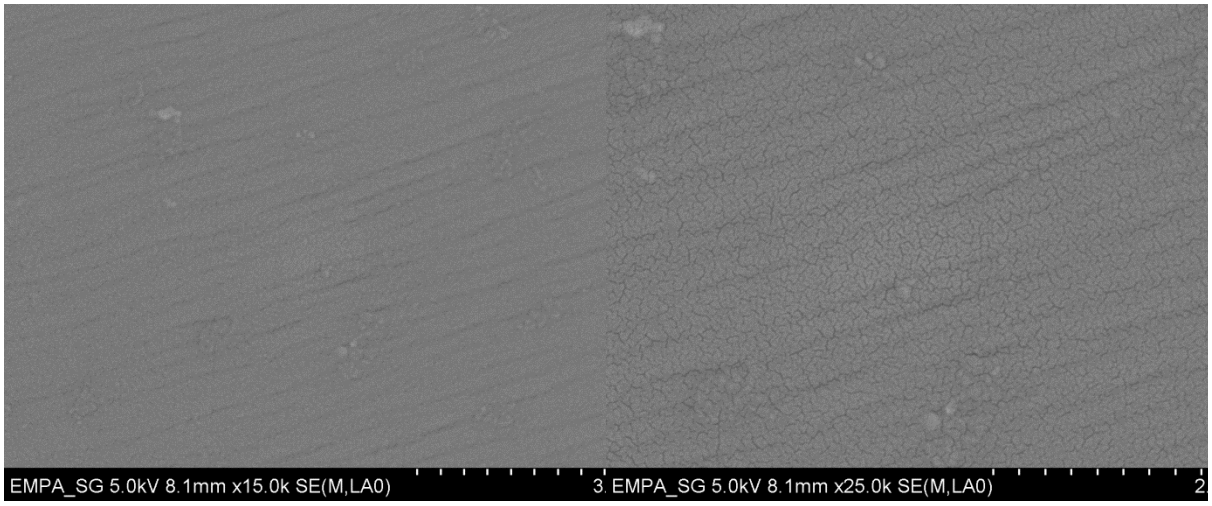

Figure 11. Surface micrograph of fibre that inhibited white parts, presenting crazes on the surface.

The production and structural characterization of the optical fibres produced by melt spinning plant is described in details in next Chapter.

4.2 "Polymer optical fibres for textile applications – bicomponent melt spinning from cyclic olefin polymer and structural characteristics revealed by wide angle X-ray diffraction"

By Felix A. Reifler[a, b, *], Rudolf Hufenus[a], Marek Krehel[c], Eugen Zgraggen[d], René M. Rossi[c], Lukas J. Scherer[c], accepted for publication in Polymer.

Abstract

To obtain thin and flexible polymer optical fibers (POFs) for textile applications, bicomponent melt-spun fibers with a cyclo-olefin polymer (COP) in the core and a tetrafluoroethylene-hexafluoropropylene-vinylidene fluoride terpolymer (THV) in the sheath have been co-extruded on the pilot scale. With higher draw ratio, the orientation within the amorphous COP core increases and the preferred interchain distances gradually change in response to the drawing parameters, as could be revealed by wide angle X-ray diffraction (WAXD). The bicomponent arrangement can promote the formation of a regular core surface because irregularities at the interface between the core and the sheath component can even out thanks to thermal shielding by the sheath component. Light propagation loss (9 dB/m at 652 nm for the most transparent fibers) and tensile properties of the fibers turned out to be adequate to enable their use in industrially produced luminous textiles.

Graphical Abstract

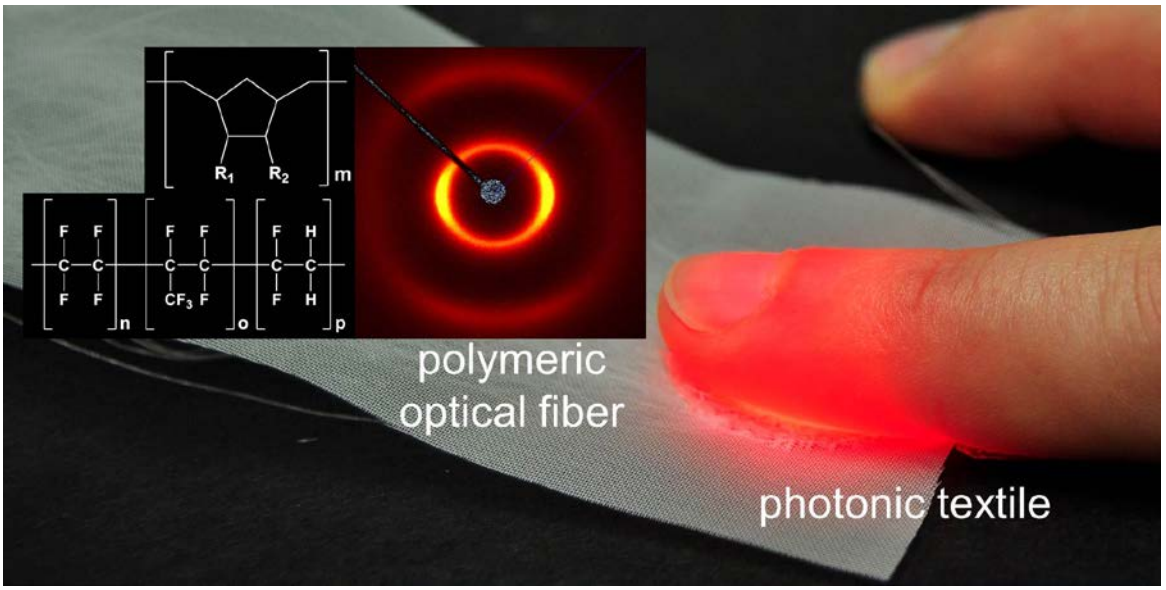

4.2.1 Introduction

Since the digitalization of the data communication in the 1990s, there is an ever growing need on flexible and cheap solutions of optical fibers. Optical fibers made of polymers are not only more flexible, but also cheaper than glass optical fibers. Compared to glass optical fibers, the light attenuation of polymer optical fibers (POFs) is higher, which limits their use to short-range applications. But with the advent of digital technologies, POFs came into focus for short range data transmission in, e.g., cars and home networks [55, 63].

Production and use of textiles is very demanding for the fibers in terms of flexibility and toughness. Flexible POFs made the incorporation of optical fibers into textiles possible [55]. The main use of these POF fabrics are design or illumination applications [64-68]. Other research activities focus on the use of POF fabrics as wearable and flexible sensing devices, for instance for body and health monitoring, or for monitoring the environment [7, 49, 55, 69-79].

The optical fibers used for textile applications are usually realized without an additional protective jacket and are multi-mode fibers with a core-cladding geometry. Its commercial availability, the low material cost and its adequate thermal stability made Poly(methyl

methacrylate) (PMMA) the most frequently used material. for these applications [55, 80], usually in combination with a fluorinated polymer as cladding material [63]. Polymer materials like polycarbonate, polystyrene, and silicone elastomers were also used as light guides in optical fibers [63, 81]. The use of rather uncommon polymers like polyether sulfones, polysulfones or polyether imines is still in the research phase [82].

PMMA, however, has also some drawbacks. Although it is a hydrophobic polymer, PMMA can absorb up to 2% of water [83], which also influences its attenuation characteristics [63]. Its rather high brittleness compared to other polymers used in the fabrication of textiles makes this polymer disadvantageous for the use in fabrics. Furthermore, due to its melt-flow properties, PMMA is not suited for the melt-spinning process, which is the most common procedure to form fibers in the textile industry. Hence, a preform has to be prepared, which is subsequently drawn to the desired diameter. This is necessarily a batch process, using one preform at a time, and the length of fiber produced from each preform is limited [81].

In order to receive continuously produced and affordable POFs for textile applications, it is essential to produce them via a continuous fiber spinning process. The desired core-cladding geometry can then be realized by melt-spinning of bicomponent fibers. Such fibers are manufactured by simultaneously extruding two polymers into one fiber. The different types which can be produced include core-sheath, side-by-side and island-in-the-sea fibers [84, 85]. With bicomponent melt-spinning, advantageous properties of two materials can be combined in one fiber [86]. In addition, the two components can mutually influence their thermal profiles along the spinline during melt spinning due to the shielding effect of the sheath component. This effect can be utilized to influence the structure formation of both components in the desired way [87-89].

During melt-spinning, the extruded filaments are drawn to smaller diameters [85], which increases the orientation of the polymer chains. In semi-crystalline polymers this often leads to an increased crystallinity through orientation-induced crystallization [90]. Although this process distinctly improves tenacity and modulus of the fibers, the increase in crystallinity is not desired for optical fibers since it creates irregularities and density fluctuations in the material which leads to increased light attenuation through scattering [81, 91]. The ideal polymer for the POF production using a melt-spinning plant is drawable in order to gain mechanical strength, but it should maintain its amorphous structure in the drawing process. Drawing an amorphous polymer will align the polymer chains, which leads to a more homogenous structure and thus to lower light attenuation due to reduced scattering [81]. (A substantial part of this study is dedicated to two-dimensional wide angle X-ray diffraction [WAXD] analysis, which is a valuable tool to investigate the orientation and other structural characteristics of amorphous melt-spun filaments [92, 93].)

The POF polymer should withstand the high processing temperatures without being oxidized or decomposed. To render the application of these fibers in textiles feasible, they should possess high flexibility and high tensile strength in order to withstand processing on industrial textile machinery. Commercially available POFs fail when used with industrial machines, as has been shown for the development of light diffusers using embroidery techniques [67]. Consequently, we started a research program to look for alternative polymers for the production of flexible optical fibers that can be produced using a melt-spinning process and that can easily be processed into textile structures [94, 95].

Cyclo-olefin polymers (COP) turned out to be a very promising class of polymers with respect to their inherent material properties and processing conditions. After their discovery in 1983 [96], the development to enhance the optical properties and mechanical strength of COP lead to the commercialization of Zeonor® in 1998 [97]. The combination

of relatively low price, high transparency, low water absorbency and high heat resistance makes this polymer an ideal candidate for the production of POFs. Furthermore, the enhanced transparency in the near-UV region compared to PMMA optimizes its use as a light-guide for sensory applications, and, other than PMMA, it is ideally suited for the extrusion processing [97]. Its very low content of volatile chemicals (8.8 ng/g) [97] should help to avoid the formation of undesired bubbles while melt-spinning.

Hong and White [98] produced a series of filaments from various COPs by melt spinning using a laboratory scale setup consisting of a capillary rheometer with a 1.593 mm die and a motor-driven bobbin to draw-down and wind up the filaments. From Zeonor 1020R, they produced filaments exhibiting ultimate tensile stresses between approx. 50 and 250 MPa and ultimate tensile strains between approx. 55 and 90 %. Winding speed divided by flow speed at die outlet ("draw down ratio") ranged from 193 to 1174. Tensile strength and Young's modulus increased with increasing draw down ratio. Unfortunately, important details concerning the production parameters are not provided, which makes it impossible to calculate the spinning velocity and the diameter of the produced fibers.

To ensure total internal reflection, a polymer with a lower refractive index than the core has to be chosen as the cladding material [70, 80]. In addition, a big difference in the refractive index between core and cladding leads to an increased numerical aperture [63]. This facilitates the launching of light from the light source into the fiber, which is especially beneficial when bundles of fibers have to be coupled with one light source. For this reason, a THV fluoropolymer (tetrafluoroethylene-hexafluoropropylene-vinylidene fluoride terpolymer) with a low refractive index was chosen as the cladding material (i.e. the sheath of the bicomponent fiber). It has a refractive index of 1.35 [99], whereas the refractive index of the COP core polymer is around 1.5 [100]. THV is moisture repellent,

exhibits high flexibility and good chemical resistance and can be processed by extrusion at similar temperatures as the COP core material chosen for this study [99, 101, 102].

In this article, the pilot scale production and the structural characteristics of thin bicomponent polymer optical fibers with a COP in the core and a THV fluoropolymer as sheath material (cladding) will be discussed. To the best of our knowledge, such fibers have not yet been reported.

4.2.2 Experimental Section

- Materials

The cyclo-olefin polymer Zeonor® 1020R (denoted here as "COP") from Zeon Chemicals (Louisville, Kentucky, USA) was used as the core material. According to the manufacturer, it has a density of 1.01 g/cm3 and a glass transition temperature Tg of 102 °C [103]. Its chemical structure is characterized by bulky ring moieties in the main chain (Fig. 12a) [104].

The fluoroplastic polymer Dyneon THVP-2030G X (denoted here as "THV") from Dyneon GmbH & Co. KG (Burgkirchen, Germany) was chosen as the sheath (cladding) polymer. It is a terpolymer of tetrafluoroethylene (TFE), hexafluoropropylene (HFP) and vinylidene fluoride (VDF) [101, 105] (Fig. 12b) having, according to the manufacturer, a density of 1.98 g/cm3 and a melting point Tm of 130 °C [99].

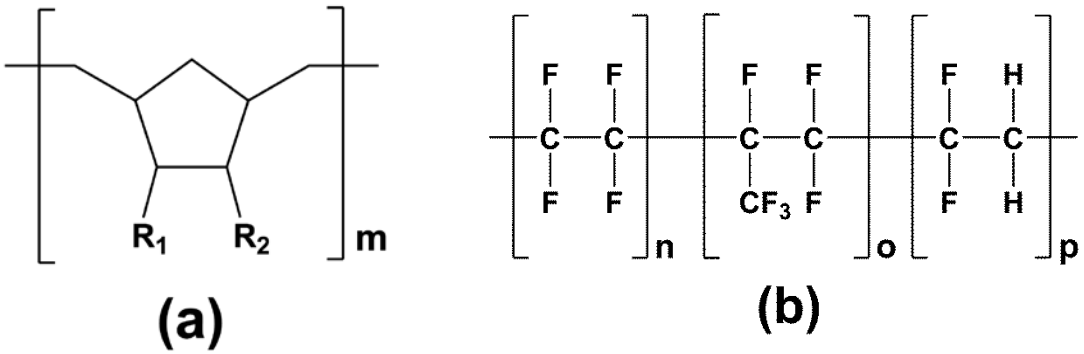

Fig. 12. Chemical structure of the COP (a) and the THV (b) used in this study (redrawn from [104] and [102], respectively).

- Production of the THV fiber

The THV monocomponent fiber was produced in a melt flow index apparatus (MFI) model 7085.15a (ZWICK, Ulm, Germany) with an external drawing engine. Before use, the material was dried in a vacuum oven for 12 h at 100 ºC. The fiber was produced at 250 ºC, with 180 seconds of pre-warming time and a 5 kg load, leading to a fiber with a diameter of (248 ± 8) µm.

- Melt Spinning

Melt-spinning was carried out on a custom-made pilot melt-spinning plant built by Fourné Polymertechnik (Alfter-Impekoven, Germany). This plant, with features corresponding to an industrial plant, enables the production of mono- and bicomponent fibers with various fiber cross-sections and material combinations with a throughput of 0.1-5 kg/h. It comprises two screw extruders and one piston extruder, a spin pack with thermally discrete polymer conduits, and a set of spinnerets allowing for elaborate fiber cross-sections. The pilot melt-spinning plant is further specified in an earlier paper [106]. For melt-spinning of bicomponent fibers, the two polymers were melted using two single screw extruders, and coaxially combined in a spinneret for bicomponent monofilaments with core/sheath-geometry. For the drawn fibers, the temperatures of the polymers leaving the extruder barrel were 250 °C for COP and 275 °C for THV, respectively (Table 1); for the free-fall (FF) COP fiber, the polymer temperature was 270 °C. The spin pack temperature was set at 250 °C for all fibers. The die consisted of a tube with 0.4 mm inner diameter and 0.7 mm outer diameter within a 1.2 mm capillary. Speed and temperature settings of the godets as well as the resulting draw ratio DR (ratio of speed of first godet and winder) are indicated in Table 1.

Table 1: Extrusion parameters of the mono- and bicomponent fibers produced.

Fiber	Polymer		c/s [b]	Core [c]	Godet 1		Godet 2		Godet 3		Winder	Draw ratio
no.	core	sheath	Vol. ratio	wt.-%	Speed [m/min]	Temp [°C]	Speed [m/min]	Temp [°C]	Speed [m/min]	Temp [°C]	Speed [m/min]	
MFI [a]	THV	-	-	100	-	-	-	-	-	-	-	
FF	COP	-	-	100	-	-	-	-	-	-	-	
A1	COP	-	-	100	200	100	290	140	300	80	300	1.5
A2	COP	-	-	100	200	100	390	140	400	80	400	2.0
A3	COP	-	-	100	200	100	490	140	500	80	500	2.5
A4	COP	-	-	100	200	100	590	140	600	80	600	3.0
B1	COP	THV	1.33	40	200	40	290	50	300	30	300	1.5
B2	COP	THV	1.33	40	200	40	390	50	400	30	400	2.0
B3	COP	THV	1.33	40	200	100	490	90	500	30	500	2.5
B4	COP	THV	1.33	40	200	134	490	165	590	75	595	3.0
C1	COP	THV	2.2	52	200	105	390	120	400	50	400	2.0
C2	COP	THV	2.2	52	200	90	490	100	500	50	500	2.5

a produced in the MFI device
b volume ratio core:sheath, calculated from the spin pump settings
c calculated from the volume ratio core:sheath (acc. to spin pump settings)

- General characterization of the fibers

For optical microscopy inspection, the fibers were embedded into epoxy resin. The embedded samples were polished to a thickness of 4 mm and examined using a Keyence VHX-1000 digital microscope (Keyence Microscope Europe, Mechelen, Belgium).

Differential scanning calorimetry (DSC) was performed employing a Mettler DSC 822e with Mettler STARe software package (Mettler-Toledo, Greifensee, Switzerland). The fiber samples were cut into small pieces and carefully put at the bottom of the aluminum pan. Heating rate: 20 °C/min (25-350 °C); N2 atmosphere (30 ml/min).

The linear mass density (titer) of the fibers was measured according to ISO 2060 [107] by weighing a defined length of the fibers sampled under defined strain.

The mean diameter of the monocomponent fibers was calculated from the linear mass density of the fiber and the density of the polymer, assuming a circular shape and not taking into account local variations of the cross section. For the bicomponent fibers, the mean polymer density $\bar{\rho}$, i.e. the quotient of the sum of the partial masses of core and sheath (m_c and m_s) and the total volume V_{tot}, was calculated according to the following equation:

$$\bar{\rho} = \frac{m_c + m_s}{V_{tot}} = \frac{\rho_c * V_c + \rho_s * V_s}{V_c + V_s} = \frac{\rho_c * \frac{V_c}{V_s} + \rho_s}{\frac{V_c}{V_s} + 1} \qquad (8)$$

This leads to mean polymer densities $\bar{\rho}$ of 1.43 g/cm3 and 1.31 g/cm3 for the bicomponent fibers with core:sheath volume ratios $\left(\frac{V_c}{V_s}\right)$ of 1.33 and 2.2 (Table 1), respectively.

The load-strain behavior of the fibers was evaluated using a Tensorapid 3 tensile tester (Uster Technologies, Uster, Switzerland); 500 N load cell; single filament tests with 100 mm test length and a constant rate of extension of 100 mm/min. The stress-strain curve of all fibers, except for fiber A4, shows a large plastic deformation zone after the initial elastic deformation. For this reason it was decided to calculate the tensile strength and the ultimate tensile stress of these fibers from the force and elongation values at the local maximum in the stress-strain curve, just before the first drop of force values preceding the large plastic deformation zone.

The ultimate tensile stress S of the monocomponent fibers was calculated from their linear mass density $LMD = m/L = (V * \rho)/L$, hence $V/L = LMD/\rho$, where m is the mass, L

the length and ρ the density. With $S = F/A = F * (L/V)$ where F is the force and $A = V/L$ is the cross sectional area, follows

$$\boldsymbol{S = F\,\frac{\rho}{LMD}} \qquad (9)$$

The ultimate tensile stress of the bicomponent fibers was calculated in the same way, but using the mean polymer density $\bar{\rho}$ calculated according to Eq. 8.

- Optical measurements

The optical propagation loss of the bicomponent COP/THV fibers was measured using the cut-back method [63]. The optical test system consisted of a medical laser diode with a wavelength of 652 nm and an intensity of 100 mW (Applied Optronics, South Plainfield, NJ, USA). The as-spun fibers were connected to a mode mixer (coupled to the light source) using F-SMA connectors from Thorlabs GmbH (Newton, MA, USA). The transmitted power was measured using an integrating sphere UM-150 (Gigahertz-Optik GmbH, Türkenfeld, Germany) and a photomultiplier tube with a V(λ) filter (PRC Krochmann Berlin, Germany). The output power P (l), in dependence of the fiber length l, was determined by subsequently shortening the fiber, while keeping the input coupling to the fiber constant. The optical loss measurements were repeated six times with different lengths l. The fiber propagation loss α, expressed in decibel per unit of length, was then extracted by using the following formula, where P(0) represents the input laser power:

$$\boldsymbol{\alpha = -\frac{10 * \log_{10}\frac{P(l)}{P(0)}}{l}} \qquad (10)$$

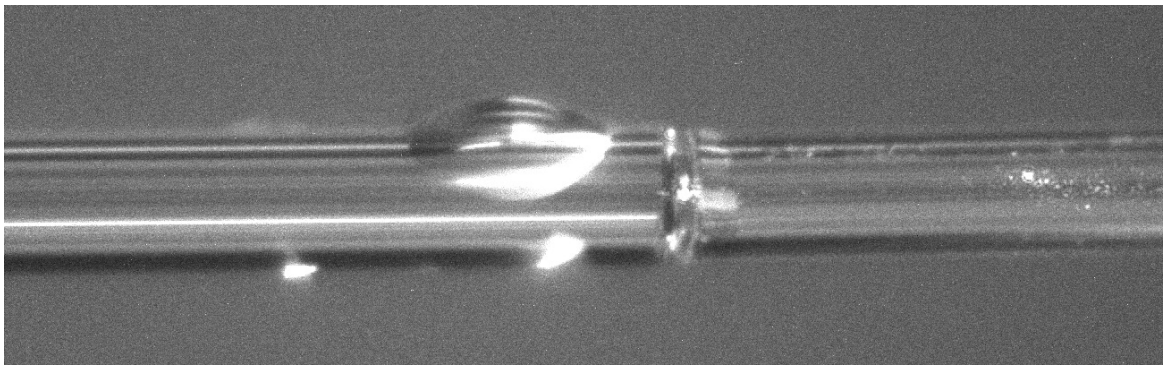

Fig. 13. Single-mode glass fiber (SM820, 5 µm core, 125 µm cladding diameter) on the left side centrally aligned to the monocomponent COP fiber A2 (right side). Reflections are minimized and coupling optimized by applying an index matching liquid in between.

For optimized in-coupling to the monocomponent COP fibers, an alternative optical test system was used: Two different light sources (Hamamatsu PLP10-065 at 655 nm and New Focus TLB-6316 at 850 nm) were coupled into a 850 nm single-mode glass fiber (SM820, 5 µm core, 125 µm cladding diameter). The glass fiber was mounted on an automated 3-axis alignment system; subsequently, it was centrally aligned to the COP fiber to achieve maximum power coupling. The system was equipped with an optical microscope to visually monitor the proper alignment of the fibers (cf. Fig. 13). An index matching liquid between the glass fiber and the COP fiber minimized back reflections and coupling losses. The transmitted power was measured using an OMM-6810B optical power meter equipped with an OMH-6720 measurement head (both from ILX Lightwave, Bozeman, MT, USA).

- Wide Angle X-Ray Diffraction (WAXD)

For wide angle X-ray diffraction (WAXD) analyses, fiber bundles consisting of three to eight single filaments (depending on the fineness of the respective single filaments) were mounted on a custom-made sample holder. WAXD patterns were recorded on an Xcalibur PX four-circle single crystal diffractometer (Oxford Diffraction Ltd, Yarnton, Oxfordshire, UK; κ-geometry; MoKα1 radiation, λ=0.070926 nm, CCD area detection system) and evaluated by means of the CrysAlis Pro Data collection and processing software (Version 171.32.29, Oxford Diffraction Ltd., Yarnton, Oxfordshire, UK) and the XRD2DScan

displaying and analyzing Software (Version 4.1, Alejandro Rodriguez Navarro; Universidad de Granada, Granada, Spain). To deconvolute WAXD data and for peak fitting purposes, the peak separation and analysis software package PeakFit (Version 4.12, Systat Software GmbH, Erkrath, Germany) was used. Peak fitting was performed using the Pearson type VII distribution function [108].

4.2.3 Results and Discussion

- Monocomponent fibers

In order to explore the melt spinning conditions for the COP, at first a series of monocomponent COP fibers has been melt-spun from Zeonor 1020R, intended to be used as the core material in the polymer optical fibers. Once the necessary speed and temperature settings of the godets were found, melt-spinning was straightforward for the fibers with draw ratios (DR) up to 2.5. In Table 1, the melt spinning conditions are presented, whereas Table 2 summarizes the mechanical and optical properties of the fibers produced.

Table 2: Physical properties of the drawn monocomponent (A1-A4) and bicomponent (B1-B4 and C1-C2) fibers produced.

Fiber no.	Draw ratio	Linear mass density [mg/m]	Diameter [a] [µm]	Tensile strength [b] [cN/tex]	Ultimate tensile stress [b] [MPa]	Ultimate tensile strain [b] [%]	Propagation loss [dB/m]
A1	1.5	14.0	133	6.7 ± 0.3	67 ± 3	4.0 ± 0.2	[c]
A2	2.0	12.5	126	6.6 ±0.7	67 ± 7	3.5 ± 0.4	[c]
A3	2.5	9.4	109	12.5 ± 0.4	127 ± 4	4.4 ± 0.1	[c]
A4	3.0	6.5	91	18.2 ± 1.4	184 ± 15	9.4 ± 1.9	[c]
B1	1.5	33.1	172	3.8 ± 0.1	55 ± 2	3.4 ± 0.3	49 ± 12
B2	2.0	25.0	149	6.1 ± 0.2	87 ± 3	4.2 ± 0.3	22 ± 9
B3	2.5	20.1	134	9.0 ± 0.2	129 ± 2	4.6 ± 0.1	9 ± 5
B4	3.0	15.7	118	4.8 ± 0.2	69 ± 3	4.2 ± 0.3	16 ± 2
C1	2.0	28.0	165	8.0 ± 0.3	105 ± 4	4.1 ± 0.1	9 ± 2
C2	2.5	22.4	148	11.2 ± 0.5	147 ± 7	4.4 ± 0.2	15 ± 6

[a] calculated from the linear mass density of the fiber and the density of the polymer (cf. text)
[b] at the local maximum in the stress-strain curve before the first drop of force values (except for fiber A4, cf. text)
[c] not measurable; light intensity at the end of the fiber below the detection limit of the equipment.

Although the fibers A1 to A3 with DR 1.5 to 2.5 had a transparent appearance, the light intensity at their output was below the detection limit of the system regularly used to measure propagation loss. To check whether this was caused by a light guiding problem inherent to the fiber or by an in-coupling issue, an alternative optical test system was used (cf. Fig. 13). The light intensity was still below the detection limit, even with fiber lengths of only 0.1 m. As these fibers are transparent, it has to be assumed that their high loss of light intensity is due to surface irregularities reducing the relative amount of light reflected back to the fiber core at the interface between the polymer and the surrounding air. Instabilities of the polymer flow inside the die and at the die outlet can cause surface melt

fracture which affects the fiber surface and leads to phenomenons like, e.g., sharkskin instability [109].

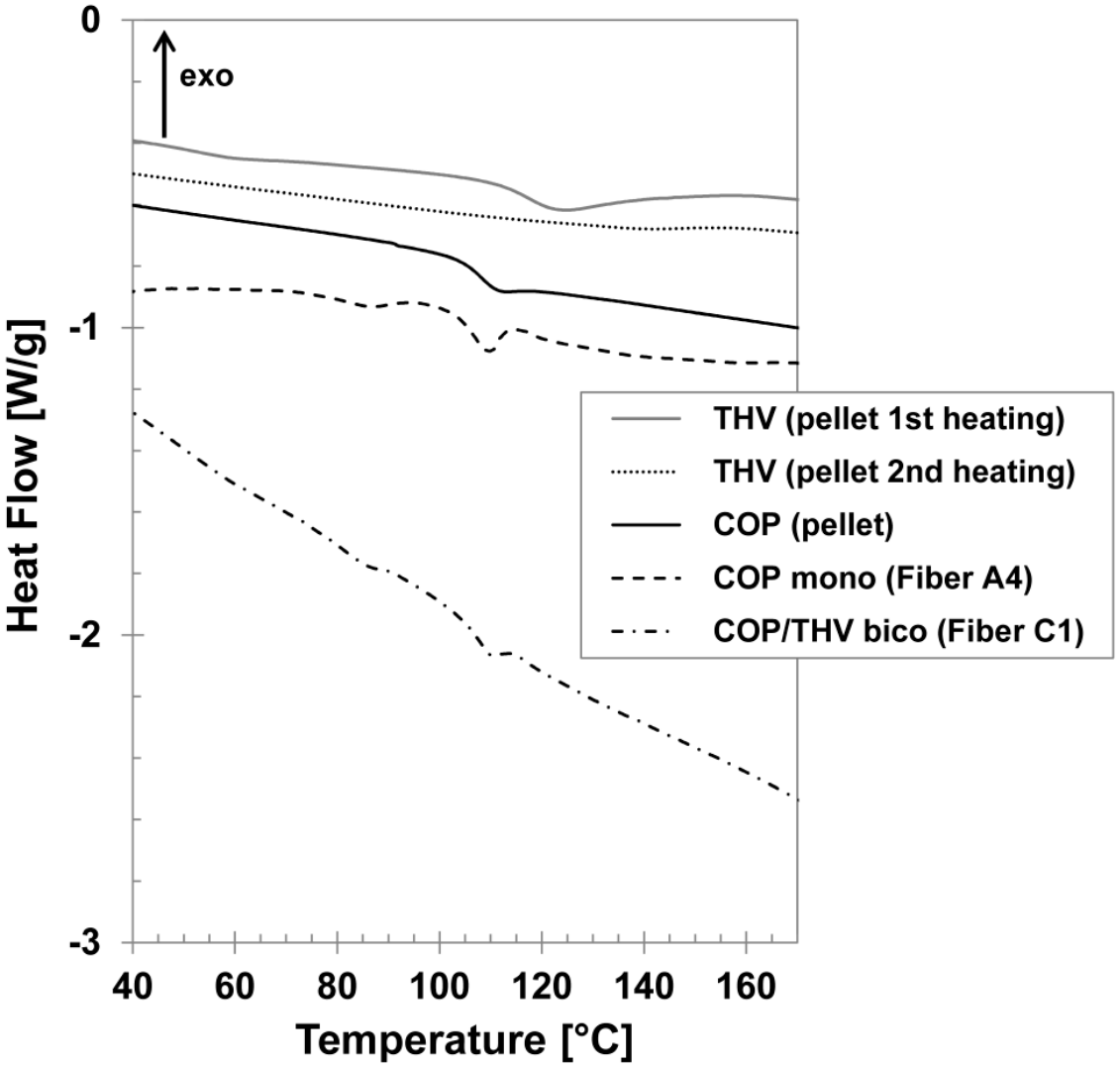

Fig. 14. DSC curves of THV (pellet, sample weight 9.81 mg), COP (pellet, 11.37 mg, 2nd heating), a monocomponent COP fiber (1.32 mg) and a bicomponent COP/THV fiber (2.15 mg).

For the production of fiber A4 with DR 3 it was possible to use the same speed setting of godet 1 and the same temperature settings of all godets as for the production of fibers A1 to A3 with lower DR. The fiber itself, however, exhibited opaque and transparent zones alternately arranged along the fiber in the dimension of some centimeters. This fiber did virtually not transport any light due to the opaque regions, and its propagation loss was also too high to measure even when using the alternative optical test system described above.

According to the DSC curves, the monocomponent fibers are essentially amorphous, exhibiting the COP glass transition temperature in the expected range. As an example, the DSC curve of the fiber A4 (DR 3.0) is presented in Fig. 14. It shows the COP glass transition at Tg=105 °C (manufacturer's specification: 102°C [103]), followed by an enthalpy relaxation peak [110, 111] which indicates the aging the as-spun fiber has undergone after drawing. The nature of the small and broad feature observable from 70 °C to 100 °C could not be fully clarified. The DSC curve of the COP pellets used for the melt-spinning process, however, exhibits a very small shift of the baseline at approx. 91 °C. Hence, the small feature in the DSC curve of fiber A4 could be interpreted as being the signal of a second glass transition coming from an impurity or a byproduct of the synthesis already present in the COP pellets. The lack of a melting point also indicates that the opacity of some parts of fiber A4 does not originate from crystalline regions.

- Wide Angle X-Ray Diffraction (WAXD)

In order to get more information about the structure of the fibers, and to clarify if the opacity variation within fiber A4 is also connected with a change in the structure of the fiber, wide angle X-ray diffraction (WAXD) measurements of the monocomponent COP fibers have been performed. The resulting WAXD patterns (Fig. 15) show a diffuse halo. Such diffuse halos are characteristic of amorphous materials [112]. The maximum position of the first (strong) halo can be interpreted as representing the preferred interchain distance between chain segments in the amorphous material; the second (weak) halo at higher scattering angles 2θ can be assigned to preferred intrachain distances [113, 114].

Scans of the first halo along the scattering angle 2θ with an angular aperture of 10° (cf. Fig. 15b) in meridional direction (i.e. fiber direction) and in equatorial direction are presented in Fig. 16. For the free-fall fiber (FF), which was collected after the spinneret, but before it

struck the first godet, the meridional (mer1) and the equatorial (eq1) peaks show nearly the same maxima at $2\theta \approx 7.4°$.

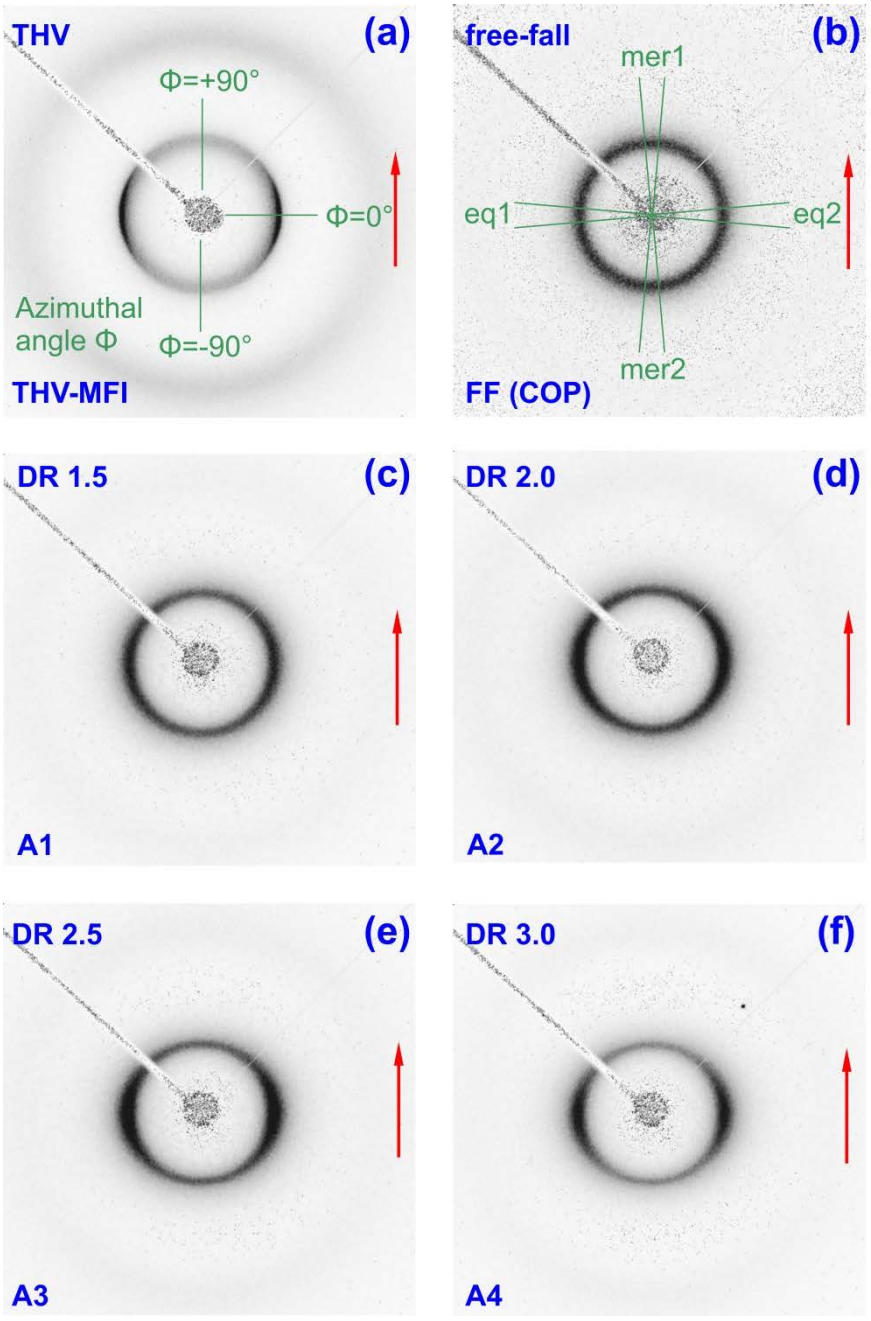

Fig. 15. WAXD pattern of the THV-MFI fiber and the monocomponent COP fibers. The arrow indicates the fiber direction. Indications of azimuthal angle Φ and the azimuthal sectors mer1, eq1, mer2 and eq2 (angular aperture: 10°) hold for all mono- and bicomponent fibers.

The preferred interchain distance d can be calculated via the Bragg equation [115]

$$d = \frac{n\,\lambda}{2\ sin\,\theta} \qquad (11)$$

with n=1, and where λ is the X-ray wavelength and θ is half the scattering angle (2θ) of the maximum position of the halo. For the chain segments in the free-fall fiber FF, a preferred interchain distance of approx. 0.55 nm was found.

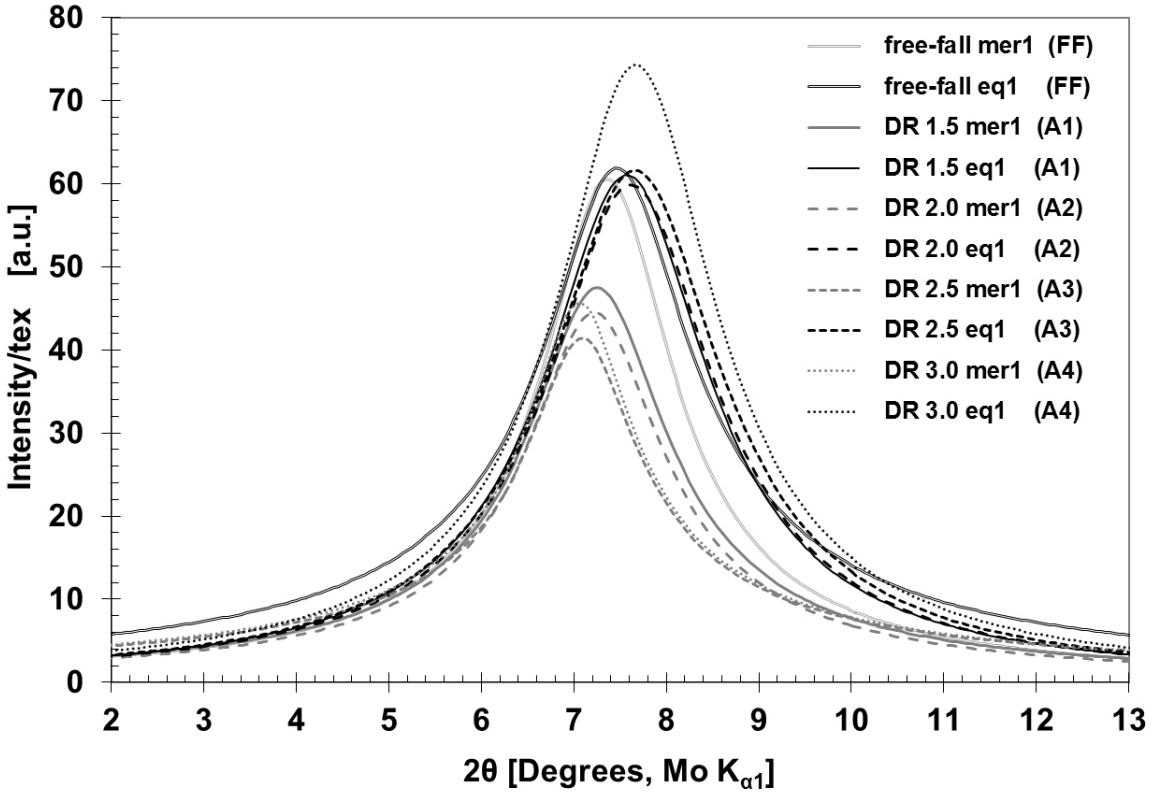

Fig. 16. Fitted peak 1 from the 2θ scan of the first halo for all monocomponent COP fibers (Table 1). Scans were performed with an angular aperture of 10° (cf. Fig. 15b) in meridional direction (i.e. fiber direction) and in equatorial direction.

With higher DR, the equatorial intensity is getting bigger relative to the meridional intensity, and arcs begin to form. This is a clear indication that a degree of orientation is induced in the polymer during drawing [92]. The increasing orientation for higher DR can be visualized by plotting the azimuthal Φ scan for the various monocomponent COP fibers (Fig. 17). The higher ratio between the equatorial intensity at Φ=0° and the meridional

intensities at Φ=+90° and Φ=-90° for fibers with a higher DR can clearly be seen. The azimuthal Φ scan of the free-fall fiber FF shows no sign of orientation. Since this fiber was collected in an early stage of fiber formation, before the first godet, and where its solidifaction process was still ongoing, spinline stress and strain rate were apparently too low to induce a noticeable orientation. This led to simple thinning instead of orientation development [85, 90].

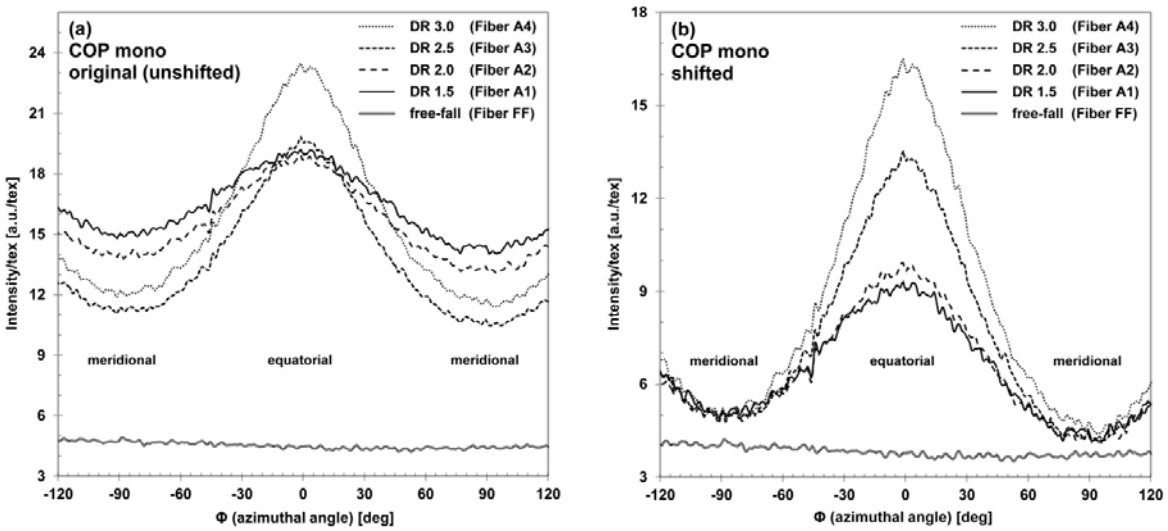

Fig. 17. Azimuthal Φ scans of monocomponent COP fibers, visualizing the increasing orientation for higher draw ratios (DR) by the higher ratio between the equatorial intensity at Φ=0° and the meridional intensities at Φ=+90° and Φ=-90°. Original unshifted (a) and vertically shifted (b) intensity values. Target intensity value for shifting: 5.0 at Φ=-90°; data of the free-fall fiber remained unshifted. The azimuthal scan along the Φ angle was performed using the data in the 2θ sector from 3.0° to 13.0° thus including the complete first halo. Central moving average using the unweighted mean of 3 values; the averaging process was iterated 3 times.

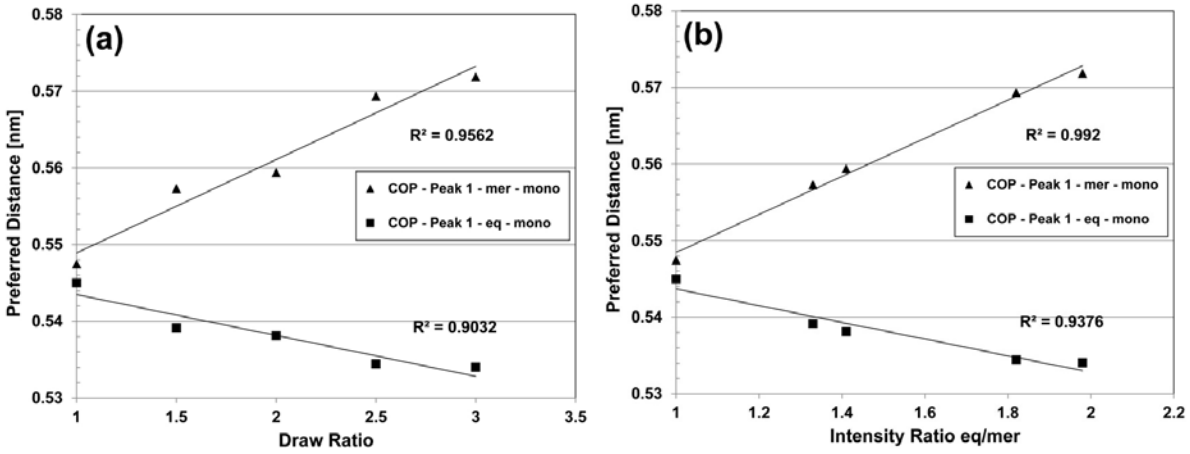

Fig. 18. Preferred distances from fitted peak 1 vs. draw ratio (a) and vs. intensity ratio eq/mer (b) of the monocomponent COP fibers. Mean values of mer1/mer2 and eq1/eq2, respectively. Draw ratio 1 refers to the free-fall fiber (FF).

Along with the higher orientation, the halo deforms and receives an oval shape. Since the equatorial scattering can be attributed to the chain segments oriented parallel to the fiber direction, and the meridional scattering is due to the chain segments oriented perpendicular to the fiber direction [92], there is a difference between these two interchain distances in the drawn filaments. Fig. 18a shows that this difference is between 0.02 and 0.04 nm, with values between 0.53 and 0.57 nm for the preferred distances. The difference is bigger for higher draw ratios and can be fitted to a linear function with reasonable coefficients of determination (Fig. 18a).

This means that in the drawing process, the polymer chains oriented parallel to the fiber direction converge, whereas the distance between the polymer chains oriented perpendicular to the fiber direction increases. Differences in the range found here (some hundredths of nm) between the preferred interchain distances of the chain segments oriented parallel and those oriented perpendicular to the drawing (fiber) direction have been observed also for other oriented polymer films and fibers [92, 93]. In addition, the preferred interchain distances found here for the free-fall fiber FF (no drawing, i.e. DR 1.0) are comparable to the maximum of the X-ray diffractogram of a series of cyclo-olefin

copolymers comprised of ethylene and norbornene units, indicating a repeat distance of 0.52 nm [116].

Fiber A1 with a DR of 1.5 exhibits an ultimate tensile stress of (67 ± 3) MPa, which is only slightly higher than the ultimate tensile stress of the unoriented bulk polymer (53 MPa [104]). As expected, the tensile strength of the fibers is increasing when going from DR 1.5 to 3.0 (Table 2).

The WAXD diagram of fiber A4 with DR 3.0 originates from a fiber bundle which had transparent and opaque parts in the X-ray beam. Additionally, transparent and opaque parts were cut out separately from a piece of fiber A4, and two fiber bundles were fabricated consisting of transparent parts only and opaque parts only, respectively. When examining these two fiber bundles with WAXD, they showed no difference regarding interchain distances and orientation. Since the DSC measurements confirmed the amorphous status of fiber A4 (cf. above) and there are no differences in interchain distances and orientation, the opaque appearance of parts of fiber A4 is rather due to an effect on the microscale: Under high local stress, amorphous polymers are prone to form micromechanical deformations (crazes), adopting a white, opaque appearance caused by light-scattering from the crazes [61, 62]. The first step in crazing is the generation of voids [117]. If such voids already exist in the fibers A1, A2 and A3 with lower DR and a transparent appearance, they are apparently too small to scatter visible light. However, the fact that crazing occurred in the monocomponent COP fibers with DR 3.0 shows that these fibers are beyond the DR range which is accessible with the production equipment used for this study.

- Bicomponent fibers

The monocomponent COP fibers showed high propagation loss mainly due to surface irregularities. In order to receive COP fibers with assured total reflection and a smaller propagation loss, it was decided to produce bicomponent fibers with core-sheath geometry.

From previous experience [89] it was already known that the shielding effect of the sheath component can reduce the cooling rate of the core and reduce its freeze-point stress, which will promote the formation of a regular structure within the core component. This effect is comparable to the installation of a post heater under the spinneret in order to achieve delayed quenching of the melt-spun filament [118-121]. In addition, it was expected that the core surface would be more regular than in the monocomponent fibers because irregularities at the interface between the core and the sheath component can even out thanks to thermal shielding by the sheath component.

A series of bicomponent fibers with COP in the core and THV in the sheath was produced varying the DR and the core-to-sheath volume ratio (Table 1). All these fibers had a transparent appearance, showing no opaque parts. Hence, it can be assumed that no crazing occurred in these fibers. An example of their cross-sectional appearance is presented in Fig. 19.

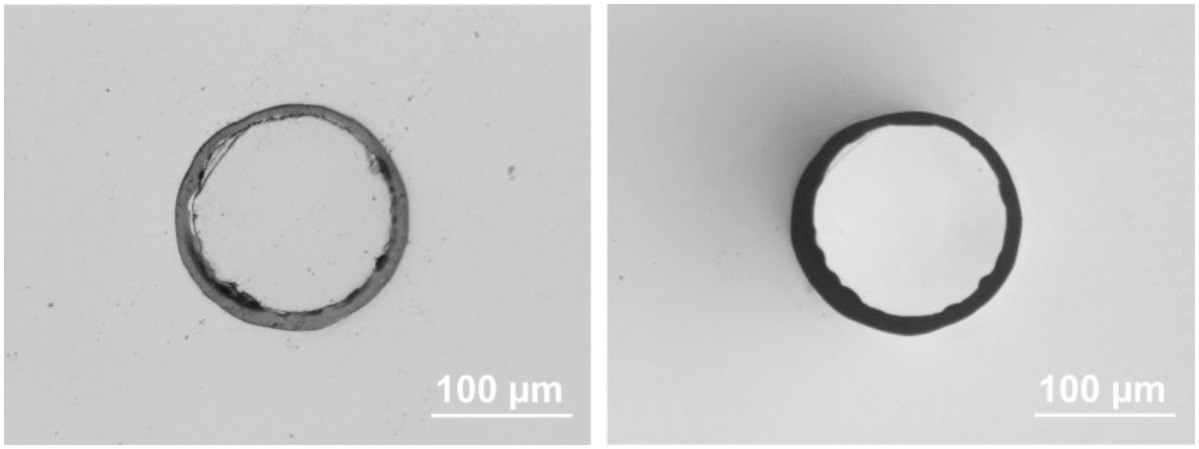

Fig. 19. Optical micrographs of the cross section of the COP/THV bicomponent fiber C1 with a volume ratio core:sheath of 2.2. Left: incident light exposure. Right: transmitted light exposure.

As expected, light propagation in the bicomponent COP/THV fibers is much better than in the monocomponent COP fibers; measuring the propagation loss of the bicomponent fibers did not pose substantial problems. The resulting values are presented in Table 2. Generally,

the fibers with higher draw ratio show a tendency to lower propagation loss values. This can be interpreted as the result of the more homogenous structure in the fiber due to the drawing procedure [81]. Additionally, as shortly described above, the sheath polymer (THV) assures a smooth surface of the COP core by influencing the temperature profile of the core polymer (COP) along the spinline. It also protects the COP core from dust, fingerprints, humidity and water, and by taking the usual role of the cladding, it supports the total inner reflection at the COP-THV interface by its low refractive index.

With propagation loss values of 9 dB/m, the best of the bicomponent fibers produced in this study have the potential to be used for sensorial or luminous applications [7, 55], where short distances around one meter are involved. They contain, however, small bubbles at the interface between core and sheath (Fig. 19). Such bubbles are generated at the die exit, where the polymer flow produces a vacuum between core and sheath. This vacuum is filled up by dissolved gases, moisture and other volatile matter evaporating from the polymers as a result of the pressure drop at the die exit [122, 123].

During fiber production on the pilot plant, inevitable and ubiquitous small variations of the production conditions occur. The opaque and transparent parts alternately arranged along the monocomponent fiber A4 (cf. above) are evidence of this fact. Nevertheless, it was possible to produce fiber A4 with DR 3.0 without applying elevated godet temperatures. Adding a second component and switching over to bicomponent fibers, however, led to increased variations of the production conditions. As a consequence thereof, the production of the bicomponent COP-THV fibers with DR 2.5 and DR 3.0 was only possible with elevated godet temperatures (Table 1). For fiber B4, the temperatures of godets 1 and 2 were set at 134 °C and 165 °C, respectively, which is considerably above the glass temperature of the core polymer. Applying lower godet temperatures led to repeated ruptures of the filament, which made it impossible to collect the fiber on the bobbin.

As expected, the tensile strength of the bicomponent fibers B1 to B3 is increasing when going from DR 1.5 to DR 2.5 (Table 2), but the ultimate tensile stress of fiber B4 is considerably smaller than expected. Obviously, the high godet temperatures had consequences regarding the tensile properties of fiber B4: Its tensile strength is not as high as expected, but the values for the ultimate tensile stress lie between the values for fibers B1 and B2 with DR 1.5 and 2.0, respectively. This means that in the case of fiber B4, the speed settings for godets 2 and 3 (Table 1) did not lead to a proper drawing process. Instead, mainly thinning of the fiber occurred.

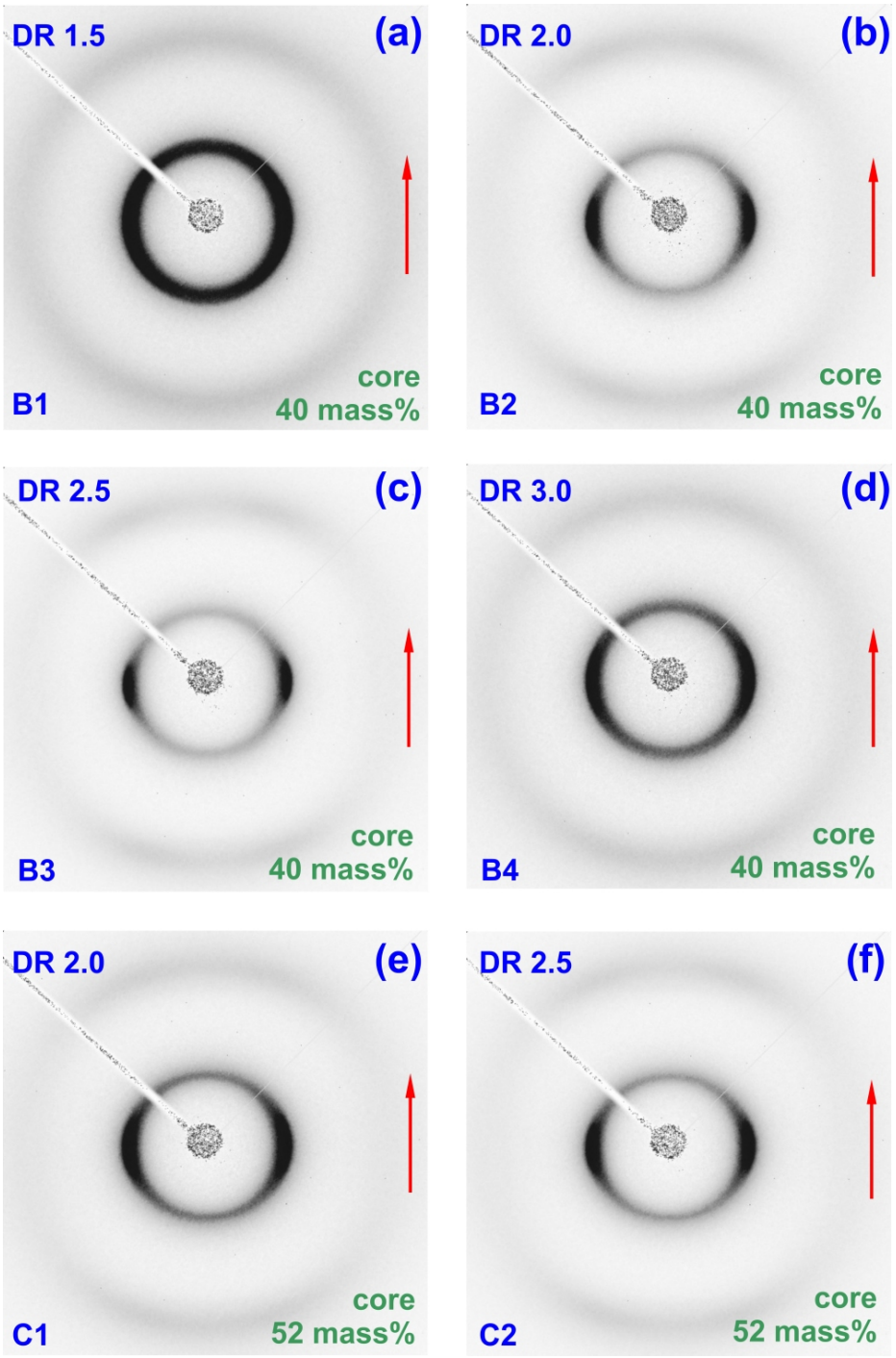

Fig. 20. WAXD pattern of the bicomponent COP/THV fibers. The arrow indicates the fiber direction. Indications of azimuthal angle Φ and the azimuthal sectors mer1, eq1, mer2 and eq2 cf. Fig. 15.

The DSC curves of the bicomponent COP/THV fibers (cf. DSC curve of fiber C1 in Fig. 14) show the same features as the DSC curves from the monocomponent COP fibers. In particular, there appears no melting peak of the THV, although the manufacturer specifies

a melting point of 130 °C for the THV used in this study [99]. The DSC curves of the THV pellets show a broad melting region. The melting peak has a maximum at 124 °C and its area corresponds to a melting enthalpy of only 7 J/g, which is a very small value for an organic compound [124]. After cooling down from 200 °C at a rate of 10 °C/min (crystallization peak [not shown]: Tmax=111 °C, crystallization enthalpy 1.5 J/g), the melting peak of the second heating is even broader and shows basically the same area as the melting peak of the first heating. From this behavior, it can be concluded that the crystallization of the THV is hindered, and the formed crystals are small and defective.

Consequently, the WAXD patterns of the bicomponent COP/THV fibers (Fig. 20) do not exhibit any sharp reflections, but show halos like the WAXD patterns of the monocomponent COP fibers (Fig. 15). The halos in Fig. 20, however, are now a superposition of the diffraction signals of COP and THV.

- Devonvolution and Peak Fitting

In order to make the separate evaluation of the COP core possible, the data coming from the COP have to be separated from the THV data by a deconvolution and peak fitting procedure. This procedure was started using the position of the COP peaks in the 2θ scans of the monocomponent COP fibers in Fig. 16. To also generate a starting point for THV, the WAXD pattern of the THV-MFI fiber (Fig. 15a) was used. Peak fitting of its mer1 and eq1 sectors shows that only a three-peak-fitting procedure can produce satisfactory coefficients of determination (Fig. 21). Hence, peak fitting of the 2θ scans of the bicomponent fibers will result in five peaks for each azimuthal sector. Representative for all evaluations, Fig. 22 shows the results of the peak fitting procedure for the bicomponent COP/THV fiber C1 and the peak attribution to COP. Regarding peak fitting for all six bicomponent COP/THV fibers, the mean values for the resulting coefficients of determination were r2=(0.985±0.005) for the peaks of the meridional sectors and

r2=(0.997±0.002) for the peaks of the equatorial sectors, respectively. The r2 values for the equatorial sectors are generally better because the intensities of the peaks were distinctly higher in these sectors.

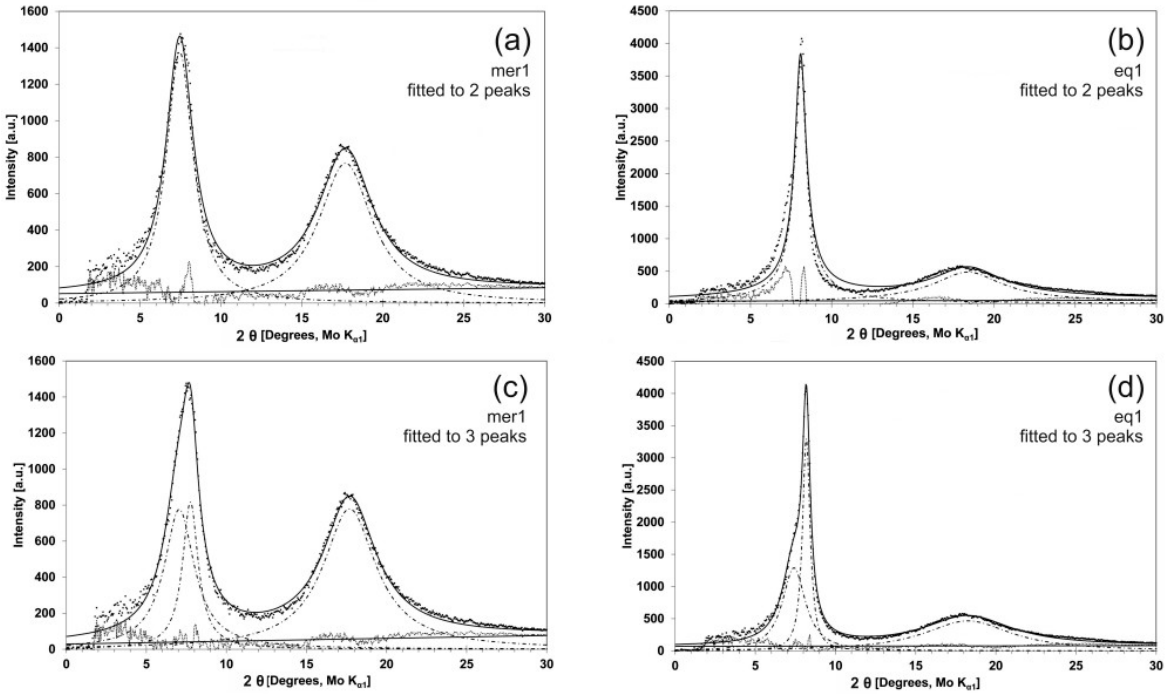

Fig. 21: Peak fitting of the experimental WAXD data (mer1 and eq1 sectors) of the THV-MFI fiber. Coefficients of determination for the two-peak-fitting: r2(mer1)=0.976, r2(eq1)=0.947; for the three-peak-fitting: r2(mer1)=0.981, r2(eq1)=0.991. Dots show the observed data points, dashed lines represent the fitted peaks. The continuous curve is the sum of the resolved peaks, whereas the continuous line at the bottom is the baseline. The dotted line is the difference between the observed intensities and the fitted values. Please note the difference in the intensity scaling (y-axis) for mer and eq data, respectively.

The calculated area of the two COP peaks and the three THV peaks in each bicomponent fiber was used to check the reliability of the peak attribution marked in Fig. 22: The fibers B2 and B3 contain 40 wt-% of COP, fibers C1 and C2 contain 52 wt-% of COP. Hence, the calculated COP mass ratio C1:B2 and C2:B3 will be 52/40=1.3. As a first approximation, the area of the diffraction peaks attributed to COP can be considered to be proportional to the mass of the diffracting polymer COP. Hence, the COP peak area ratio for the fibers mentioned above should also be 1.3. Using the data for the fitted COP peaks and taking

into account the linear mass density of the fiber bundles used for the WAXD experiments, experimental intensity ratios of 1.21 and 1.18 were calculated for C1:B2 and C2:B3, respectively. Performing the same procedure for the THV peak area ratios (calculated value: 48/60=0.8), experimental values of 1.15 and 0.93 could be calculated, respectively. These values are in accordance with the calculated values, and, as expected, the COP value is higher than the THV value for both pairs of fibers (C1, B2 and C2, B3).

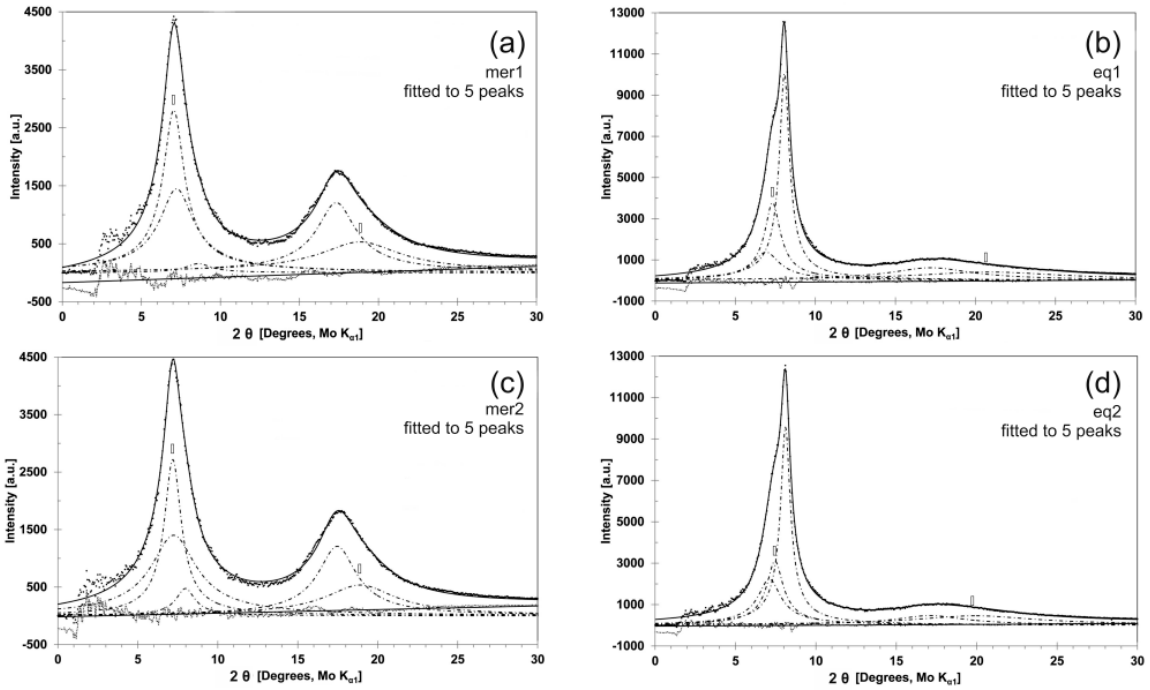

Fig. 22. Peak fitting of the experimental WAXD data (mer and eq sectors) of the bicomponent COP/THV fiber C1. The small and narrow vertical rectangles locate the position of the peak maxima for the two fitted COP peaks in each sector. Coefficients of determination: r2(mer1)=0.986, r2(eq1)=0.995, r2(mer2)=0.987; r2(eq2)=0.998. Attribution of line drawing styles: cf. caption for Fig. 21. Please note the difference in the intensity scaling (y-axis) for mer and eq data, respectively.

In analogy to the procedure for the monocomponent COP fibers (cf. above and Fig. 18), the fitted data for the first (strong) COP peak in the region of 7.5° 2θ in the bicomponent COP/THV fibers were now used to calculate the preferred interchain distances in meridional and equatorial direction. In the plot of these distances versus the DR (Fig. 23a), the same general trend as in the monocomponent fibers can be seen (cf. Fig. 18). The distance values range between 0.53 and 0.58 nm, and the difference between the preferred

interchain distances parallel and perpendicular to the fiber direction ranges between 0.01 and 0.04 nm, which is in good accordance with the values for the monocomponent fibers. The data points for DR 3.0 (fiber B4), however, do not fit into this trend. As mentioned above, fiber B4 had to be produced using higher godet temperatures than for the other bicomponent fibers (cf. Table 2), which led to inferior tensile properties than expected. From the WAXD data for the interchain distances it can also be seen now that the elevated godet temperatures led to a different orientation behavior of the polymers during the drawing process.

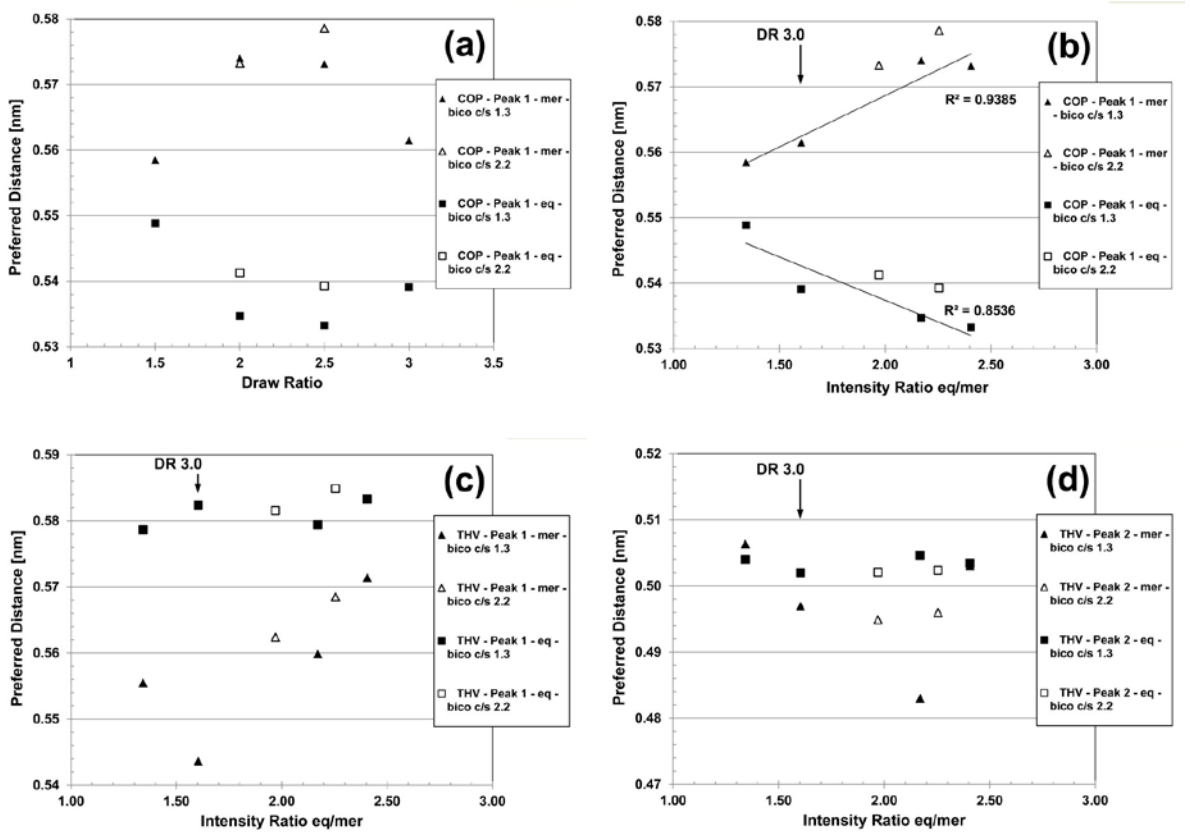

Fig. 23. Preferred distances from fitted peaks of the COP/THV bicomponent fibers: (a) from COP peak 1, vs. draw ratio; (b) idem, but vs. intensity ratio eq/mer; (c) from THV peak 1, vs. intensity ratio eq/mer; (d) from THV peak 2, vs. intensity ratio eq/mer. Mean values of mer1/mer2 and eq1/eq2, respectively. Regression lines in (b) are calculated for data of the bicomponent fibers with a mass ratio core/sheath of 1.3.

To be able to better explain the calculated interchain distances in fiber B4, the idea was not to put the DR in the x-axis, but an "orientation factor", expressed by the area (or intensity)

ratio between the equatorial sectors at Φ=0° and the meridional sectors at Φ=+90° or Φ=-90°. Because the halos of COP and THV strongly overlap in the region of the first COP halo, a "COP only" Φ scan cannot be generated. That is why it is only possible to use the data of an "overall Φ scan", taking into account the data in the 2θ sector from 3.0° to 13.0°, thus including the first halo of COP and the first two peaks of THV. The plot of the shifted "overall Φ scans" (Fig. 24b) shows that the full width at half maximum (FWHM) values of the curves are comparable; hence it is admissible to use the maximum equatorial intensity at Φ=0° and the minimum meridional intensity at Φ=-90°, taken from the unshifted values (Fig. 24a), to calculate the ratio eq/mer. The plot shows that the intensity ratio eq/mer for fiber B4 (DR 3.0) is low and placed between the values for DR 1.5 and DR 2.0, which is the consequence of the higher godet temperatures mentioned above.

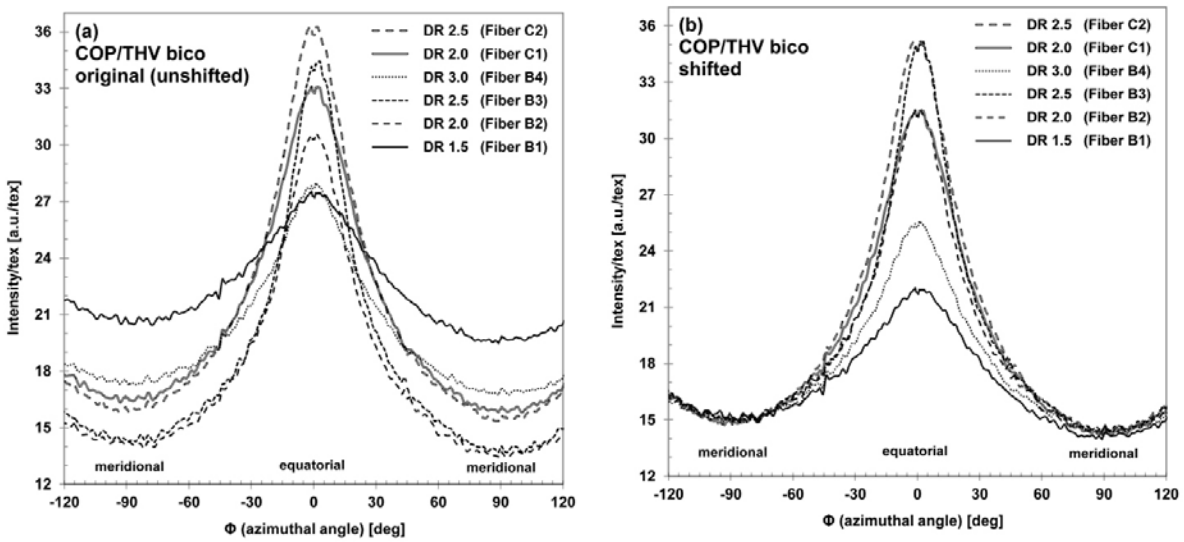

Fig. 24: Azimuthal Φ scans of bicomponent COP-THV fibers, showing original unshifted (a) and vertically shifted (b) intensity values. Target intensity value for shifting: 15.0 at Φ=-90°. The shifting process leads to a better graphical visibility of the intensity ratio eq/mer. The ratio eq/mer was calculated using the unshifted intensity values at Φ=0° and Φ =-90°, respectively. The azimuthal scan along the Φ angle was performed using the data in the 2θ sector from 3.0° to13.0° thus including the first halo of COP and the first two peaks of THV. Central moving average using the unweighted mean of 3 values; the averaging process was iterated 3 times.

The plot of the preferred interchain distances in meridional and equatorial direction for the first COP peak in the bicomponent fibers was now redrawn using the intensity ratio eq/mer instead of the DR as x-axis. The data of fiber B4 (DR 3.0) now perfectly fit into the general trend (Fig. 23b). When calculating eq/mer for the monocomponent fibers in the same way as for the bicomponent fibers, and plotting the preferred distances as a function of eq/mer instead of DR, the coefficients of determination for the linear regression are even higher (Fig. 18b).

The maximum of the fitted COP peak 1 of the bicomponent COP/THV fibers shows different values for different DR, and this leads to different preferred interchain distances for each fiber (cf. Fig. 23a and Fig. 23b), as discussed above. For THV, however, most of the fitted maxima of its first peak (at approx. 7° 2θ) and its second peak (at approx. 8° 2θ) are independent of the draw ratio (cf. in Fig. 23c and Fig. 23d). From this it can be concluded that they "locked in" at particular values, which can be interpreted as being a transition from a truly amorphous to a rather crystalline state.

As a matter of fact, the datasheet of THV states a melting point Tm of 130 °C [99], and the unextruded THV exhibits an endothermic melting peak at this temperature region in the DSC experiment (Fig. 14). Hence, THV can be regarded as a semicrystalline polymer. In the DSC curve of the bicomponent COP/THV fibers, however, no endothermic signal can be detected above approx. 115 °C (cf. above and Fig. 14). The two features below 115 °C are the same as for the monocomponent COP fibers and thus come from the COP core polymer. As mentioned before, the crystallization of THV is hindered and will therefore only form small and imperfect crystals. As the melting point of the THV crystals in the COP/THV bicomponent fibers cannot be detected by DSC, these crystals seem to be even smaller than the crystals formed in the THV pellets.

4.2.4 Conclusion

In this study, we produced thin and flexible polymer optical fibers (POFs) with a cyclo-olefin polymer in the core and a fluoropolymer in the sheath by bicomponent melt-spinning on the pilot scale. It was shown that monocomponent COP fibers are not suited for optical use due to a very high light propagation loss. In bicomponent melt spinning, however, the shielding effect of the sheath polymer can promote the formation of a regular interface between the core component and the sheath and favor a regular structure within the COP component in the core. The core fiber and the cladding (i.e. the sheath) are formed simultaneously in one step. The core polymer is protected from damaging external influences, and the sheath polymer provides a low and constant refractive index, supporting the total inner reflection at the core-sheath interface.

The structural characteristics of the fibers were examined by wide angle X-ray diffraction (WAXD). With WAXD, the structure development of the amorphous COP component could be followed, in particular the gradual change of the preferred interchain distances in fiber direction and perpendicular to it, in response to the drawing procedure. In the THV sheath component, however, some of these distances remained unchanged, indicating a transition from amorphous to crystalline state.

Production of COP containing fibers with high DR (2.5 and more) is a critical process and this study showed that suitable fibers with DR 3.0 are not accessible with the production equipment used: When attempting to produce monocomponent COP fibers with DR 3.0, fibers with alternatively arranged transparent and opaque zones formed, exhibiting crazing in the latter. For the production of bicomponent fibers with DR 3.0, godet temperatures beyond the glass temperature of the core polymer had to be used, and the evaluation of the WAXD data showed that this caused mainly thinning of the fiber instead of proper drawing. Orientation and tensile properties of the bicomponent COP/THV fiber with a nominal DR of 3.0 actually correspond to a DR between 1.5 and 2.0.

For visible red light, the propagation loss of the bicomponent fibers was small enough to open the possibility to incorporate them into textiles for, e.g., sensorial applications. A next step to further reduce the light propagation loss would be to minimize the accumulation of bubbles at the interface between core and sheath by intensifying the procedures to clean and dry the polymers prior to the extrusion process.

The flexibility and the mechanical resistance of the bicomponent melt-spun POFs described in this article make them good candidates to be successfully stitched on an industrial embroidery machine into carrier fabrics to build luminous textiles. Thanks to their in- and outcoupling properties, these POFs made it possible to manufacture a fully textile based reflectance pulse-oximeter sensor for non-invasive monitoring of heart rate and oxygen saturation values of human subjects [125].

Acknowledgements

This work was financially supported by NanoTera (TecInTex). The authors thank Benno Wüst and Laura Gottardo for the fiber sample preparations, Pierlugi Barbadoro for the measurements of the mechanical fiber properties, as well as Thomas Weber and Walter Steurer of the Laboratory of Crystallography (Department of Materials, ETH Zürich, Switzerland) for providing access to their X-ray diffraction equipment and generous support.

4.3 Application of Flexible Polymeric Optical Fibres for Medical Sensing in Textiles

Bicomponent melt-spun POFs as described in the section above proved to be flexible and resistant enough to be successfully stitched using an industrial embroidery machine into carrier fabrics to build luminous textiles. In Chapter 5 we demonstrate that thanks to the flexibility of fibres described in Chapter 4.2 and their in and out coupling properties we could manufacture a fully textile based reflectance PPG sensor. Moreover the analysis of

the PPG together with modified Beer-Lambert law allowed calculation of the pulse and oxygen saturation.

5. "Development of a Luminous Textile for Reflective Pulse Oximetry measurements"

By Marek Krehel, M. Wolf, René M. Rossi, Gian-Luca Bona and Lukas J. Scherer, Biomedical Optics Express, Vol. 5 Issue 8, pp.2537-2547 (2014)

Abstract: In this paper, a textile-based sensing principle for long term photopletysmography (PPG) monitoring is presented. Optical fibres were embroidered into textiles such that out-coupling and in-coupling of light was possible. The "light-in light-out" properties of the textile enabled the spectroscopic characterisation of human tissue. For the optimization of the textile sensor, three different carrier fabrics and different fibre modifications were compared. The sample with best light coupling efficiency was successfully used to measure heart rate and SpO2 values of a subject. The latter was determined by using a modified Beer-Lambert law and measuring the light attenuation at two different wavelengths (632 nm and 894 nm). Moreover, the system was adapted to work in reflection mode which makes the sensor more versatile. The measurements were additionally compared with commercially available system and showed good correlation.

5.1 Introduction

Due to the aging society, medical textiles are attracting more attention every day. In the next decades, wearable sensors are expected to conduct continued and autonomous monitoring of life-sustaining parameters [43, 126, 127]. Different approaches of long-term body monitoring solutions using textile fabrics have been intensively studied in recent years [58, 128]. The electronics involved in the proposed solutions often influence the haptic of medical textiles negatively. To overcome that problem, flexible and smart fibres allow the separation of the rigid electronics from the measured region and thus from the body. Electrocardiography (ECG) is a well-documented example where very flexible electro-conductive yarns replaced rigid electrodes and therefore allowed long-term ECG

monitoring [129]. Different research groups were attracted by the integration of polymer optical fibres into fabrics for different purposes [130][9]. In the medtech sector, luminous textiles have been reported to find applications as illuminating source in phototherapies or photodynamic therapies [55] or for sensing purposes [7]. Different ways to laterally out-couple light have been reported [7, 55] The light out-coupling can be achieved by damaging the fibre surface [7], or by bending the fibres [127]. Moreover, the use of light-emitting diodes (LEDs) as light source provides low power consumption and long lifetime. The separation of the electronics from the body and the low power consumption makes luminous textiles ideal candidates for biomedical monitoring systems [131]. Other advantages of textile-integrated flexible optical fibres for wearable systems are the light-weight structure, insensitivity to electromagnetic fields, water and corrosion resistance, comfort, ease of movements, and reduced movement artefacts [5, 6, 55, 132]. Due to these benefits, optical fibre based sensors are used in numerous applications to detect chemical or physical changes [5, 7, 133-135]. Insensitivity to electrical fields is of great importance, especially in hospitals where a lot of electromagnetic fields are present [136]. The combination of enhanced comfort while wearing the textiles and the resistance to above-mentioned parameters make photonic textiles practical for long-term monitoring systems of human vital parameters. Long term monitoring systems with enhanced haptic is very significant in monitoring paraplegic patients since any type of rigid sensors is a danger of causing decubitus ulcers [137]. The other planned application of the proposed textile-based SpO2 system is the monitoring of neonates to prevent psychological discomfort of parents caused by the big amount of medical apparatus [138]. To implement optical fibres into textiles, the fibres should be highly flexible, which is neither the case for glass-based nor for commercial available polymer optical fibres (POFs) made of polymethylmethacrylate (PMMA). For textile applications, there is a demand for polymer optical fibres made of more flexible polymers [55]. We have recently demonstrated that cyclo-olefin polymers are

ideally suited for the production of flexible optical fibres [139]. As has been demonstrated in this study, these fibres withstand even strong mechanical stresses occurring during the industrial embroidering process. The mentioned SpO2 is a parameter that measures arterial oxygen saturation indirectly and non-invasively by means of measuring light absorption in human blood [140]. Monitoring of oxygen saturation is crucial since the delivery of oxygen to human organs is essential to prevent hypoxemia and maintaining humans in wellbeing [141]. The other application where a wearable SpO2 system in reflective mode is desired is for people performing high-altitude activities e.g. mountaineering or climbing. During this activities hypothermia, trauma or severe stress levels can occur. Since the blood perfusion of the extremities can be strongly decreased in this conditions, SpO2 measurements in transmission mode is no longer possible in the body extremities e.g. in the fingers [142-144]. The above mentioned solutions work either as rigid electronics that works in both modes (transmission and reflection) or as a flexible textile but only in transmission mode. So far no-one has reported SpO2 sensing textile that would work in reflection mode. In reflection mode, the working principle is the statistical fact that the further away the light is collected from the illumination point, the deeper the light has penetrated into the tissue, which allows the volumetric determination of the blood perfusion (photopletysmography) [145, 146].

In this study, we report on a proof of concept where optical fibres embroidered into textiles measured heart rate and oxygen saturation in the reflection mode. In contrast to transmission mode, the reflection mode is more versatile. It does not limit the measurements to places like fingertips, ear lobes or toes and enables the development of a wide variety of wearable sensing systems like T-shirts, hats, breast-belts, or armbands [147]. The results we achieved were cross compared with a commercial available and calibrated device. Moreover, we show that the integration of optical fibres in form of

concentric rings enable the collection of light with constant distance from the light source as schematically presented in Fig. 25. In reflection mode, the working principle is the statistical fact that the further away the light is collected from the illumination point, the deeper the light has penetrated into the tissue, which allows the volumetric determination of the blood perfusion (photopletysmography) [27, 28].

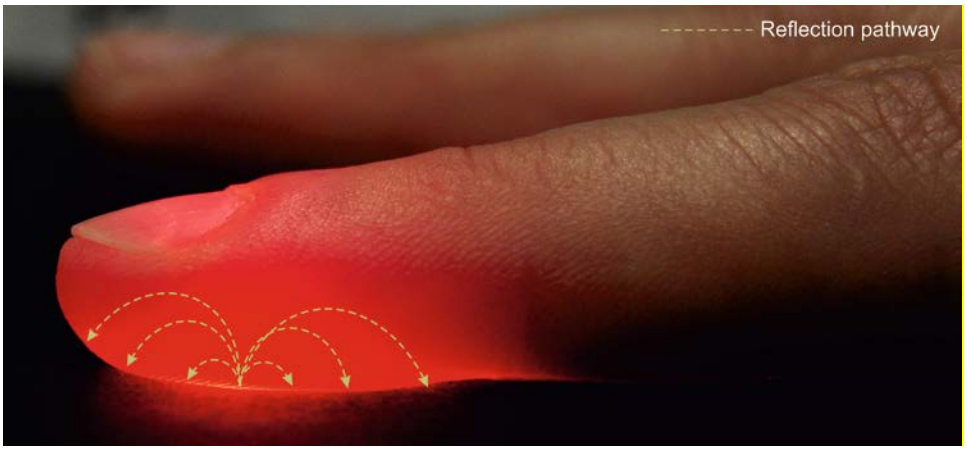

Fig. 25. Analysis of different depths of tissue. The further from the illumination point the deeper parts of tissue are penetrated (dotted line)

5.2 Materials and Methods

5.2.1 Fibre type

The optical fibres used in this study were produced using a melt-spinning process. The core of the optical fibres was made of cycloolefin polymer, (Zeonor 1020R, Zeon, Düsseldorf, Germany) and as cladding material a fluorinated polymer (THVP 2030GX, Dyneon, Burgkirchen, Germany) was used. Refractive indices of the core and cladding are 1.53 and 1.35 respectively which gives numerical aperture (NA) of 0.72. The total diameter of the fibres was 152 µm with cladding thickness of 12 µm. Light attenuation of the optical fibre was 9 dB/cm at 652 nm, measured with the cut back method. Further details for the production of the optical fibres are found in [128].

5.2.2 Sample preparation

In Fig. 26, a sketch presenting the scheme of the stitching pattern with the optical fibres is illustrated. Between the optical fibres stitched in the middle (acting as light source) and the three embroidered rings (acting as a light collector), a three dimensional ring was embroidered with black polyester yarn provided by Schweninger Textil GmbH & CoKG (Lustenau, Austria)

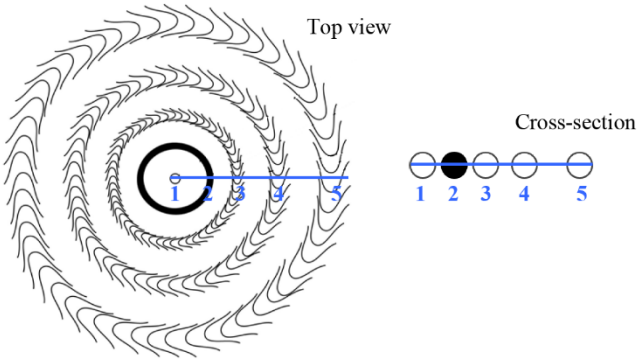

Fig. 26. Sketch presenting embroidered optical fibres. Where (1) optical fibres stitched to couple the light out; (2) three dimensional embroidered black ring to prevent light short circuit. (3),(4) and (5) represent rings of optical fibres stitched to couple the light in. Each "V"-shaped line in the rings represents a portion of a single optical fiber.

All the samples were produced at Forster Rohner AG (St. Gallen, Switzerland). The optical yarn was embroidered on the fabric using an embroidery machine ERA TM 0625 (Saurer AG, Switzerland). The carrier fabric was mounted on the vertical frame (1.60 m in width) whose movements corresponded to a digitalized embroidery pattern. In front of the fabric a perpendicularly positioned set of needles (type 4 RS/SPI nr "3770120137" manufactured by Bachmann AG Swiss) was threaded with the monofilament optical fibre. To obtain embroidery of a high quality the thread was pulled through the positive thread feed system, so called ActiFeed, that applied a tension of 85 g. The shuttle guide was positioned behind and parallel to the fabric, and at the height of the needles. The shuttle was threaded with polyester yarn (type, 80/2 Polyester (PES), white). Fig. 27 shows two patterns of laying the optical yarn on the fabric surface ("M" and "V" type). Each line represents a portion of the

laid optical yarn whereas red dots correspond to the points where the needle went through the fabric and interlaced optical yarn with the polyester yarn carried by shuttle. The zigzag stitch was used to create both patterns (Fig. 27) and optical yarn was laid on the face of the fabric whereas polyester yarn stayed at the opposite side of the fabric.

All the samples were produced at Forster Rohner AG (St. Gallen, Switzerland) on a stitching machine ERA TM 0625 (Saurer AG, Switzerland). Needles type 4 RS/SPI nr "3770120137" manufactured by Bachmann AG Swiss needles were used. The following shuttle parameters were conducted: Type: Saurer; Tension: 85 gr; Bobine: 80/2 Polyester (PES), white.

As carrier fabrics on which the embroidery was produced, three different types were tested: one thin woven, and one thin and one thick (70 g/m2 and 140 g/m2) nonwoven fabric; all the carrier fabrics were made of polyester. The woven fabrics were provided by Engelbert E. Stieger (Rorschacherberg, Switzerland) and the nonwoven fabrics by Fritz Landolt AG (Näfels, Switzerland). The woven textile sample was used as a carrier fabric for two different stitching patterns ('M' and 'V') as presented in Fig. 27. To obtain such embroidery, the optical fibres had to be fixed with a certain amount of fixation points with the carrier textile (marked in red in Figure 3). As can be seen in Fig. 27, the shape 'M' had 9 fixation points comparing to 5 fixation points in the 'V' shape pattern. The entire sample with 'V' pattern consisted of 82 optical fibres and the sample with the 'M' pattern was made of 54 optical fibres.

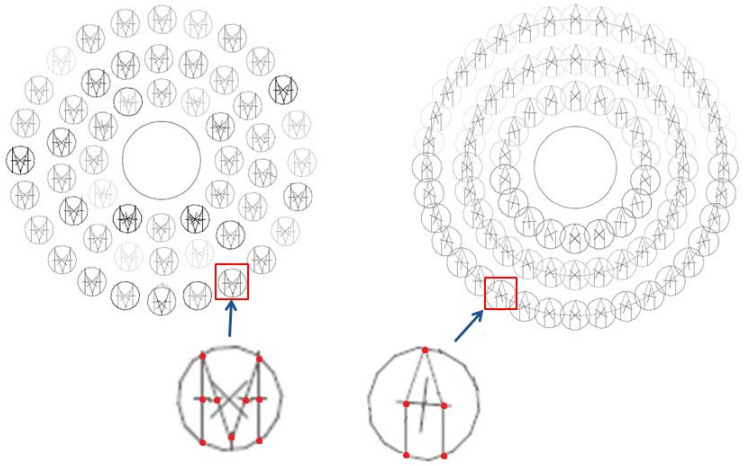

Fig. 27. Two types of embroidery patterns. On the left hand side, the 'M' type pattern is presented and on the right hand side, the 'V' type pattern. Red dots represent fixation points with the carrier textile. Pattern 'M' consisted of 54 optical fibres (12, 18, 24 in each ring from the middle to the outer one, respectively) whereas total number of fibres in the ' V' pattern was 82 (18, 28, 36 in each ring counting from the middle to the outer one)

The samples with the 'V' pattern were produced four times and underwent the following surface modifications: (1) cladding removal by rubbing the sample with a cloth immersed with solvent (acetone), (2) surface roughening by scratching with diamond lapping paper (3 µm grit) and (3) addition of polydimethylsiloxane (PDMS) layer on top of the samples. The PDMS was a Silicone Elastomer Kit (Sylgard® 184) provided by Dow Corning. It consisted of PDMS in a liquid form and a curing agent. Once mixed, it was placed in a desiccator and dried in vacuo. Afterwards the PDMS mixture was smeared over the sample forming a 1 mm thick layer. A summary of the produced samples with their abbreviated entries are presented in Table 3.

Table 3. Listing of all manufactured samples and their abbreviations

Fibre type	Carrier fabric	Abbreviation
738* ['V' pattern]	Woven fabric	V_WV
738 ['M' pattern]		M_WV
738 ['V' pattern]	Thick nonwoven	V_TCK
	Thin nonwoven	V_THN
738 [removed cladding]		RC_WV
738 [surface roughened]	Woven fabric	SR_WV

*Fibre code name, core Zeonor, cladding THV. More details in [139].

5.2.3 Measurement of the light coupling efficiency

In Fig. 28, the measurement setup of the in-coupled light efficiency is shown. A human tissue model was made of PDMS with the addition of Indian ink for light scattering purposes as described in [148]. The setup consisted of a PCB board with an LED (570 nm) placed in the centre of the board, a metal ring for supporting the PDMS-based human tissue model covering the metal ring and the LED (as presented in Figure 4a). Figure 4b shows the way the textiles were placed on the optical tissue model when tested. The bundled fibres from each ring were combined and glued with a fibre optic epoxy glue (F112) into an SMA 905 connectors both provided by Thorlabs GmbH (Dachau/Munich, Germany). In order to achieve flat fibre facets for good light coupling efficiency, the fibre bundles were polished with diamond lapping films (in this order: 6 µm, 3 µm and 1 µm grit) after the glue was dried (24 h at room temperature). The collected light was analysed using a photomultiplier (PMT) provided by PRC Krochmann GmbH (Berlin, Germany) combined with an integrating sphere. Measurements of light coupling efficiency were conducted five times.

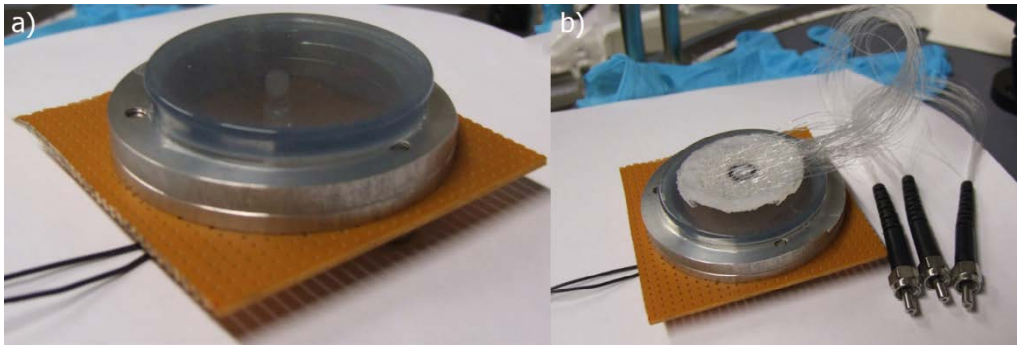

Fig. 28. Setup for measurements of the light in-coupling efficiency. On (a) the setup of the PDMS-based human tissue model is shown. The PDMS consisted of India ink and the polymer film was placed on the supporting metal rings and the LED was located centrally. (b) shows the placement of the textile when tested

5.2.4 Heart rate and oxygen saturation measurements (SpO2)

The pulse wave signals were analysed with a near infrared tissue spectrometer Oxiplex provided by ISS (Champaign, USA), the same apparatus providing the light sources. This

tissue spectrometer consists of laser diodes (with emitting peaks at 692 nm and 834 nm and power 5 mW each) that acts as light sources and photomultiplier tubes (PMT) for light detecting purposes. The light sources are time multiplex for measurements. The tests were performed with the fabric V_WV (Table 1), which was located on the middle finger of the right hand, as presented in Figure 5. First, fibres from all the rings were combined and placed into the light detecting part of the Oxiplex. In a second measurement, the signal from the fibre bundles from each ring was characterized separately.

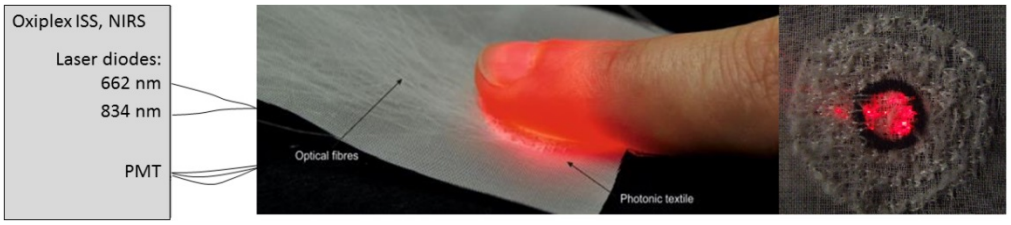

Fig. 29. Measurement conditions of the heart rate and the oxygen saturation recording using the presented photonic textile. Light is coupled from the middle of the textile into the tissue of the finger and is then scattered back to the textile. On the right hand side top view of the photonic textile, without the finger, is presented: light is delivered by the central fiber, while the black ring prevents "short circuit" (see also Fig. 26).

The oxygen saturation was calculated using the modified Beer-Lambert law. According to this law, following equations were solved to obtain changes in oxygenated (O2Hb) and deoxygenated (HHb) haemoglobin [7]:

$$\Delta HHb \times d \times DPF = (-0.239\Delta A_{692nm} + 0.099\Delta A_{834nm})$$

$$\Delta O_2Hb \times d \times DPF = (0.185\Delta A_{692nm} - 0.508\Delta A_{834nm})$$

where ΔA692nm and ΔA834nm are the amplitudes of the light attenuations caused by the pulsation, d is the distance between illuminating and detecting point and DPF the differential patch length factor, which occurs in tissue due to multiple scattering. Factors d and DPF were assumed to be the same for both wavelengths. Since the arterial oxygen

saturation is determined by the ratio ΔO2Hb/(ΔO2Hb+ΔHHb), d and DPF cancel." Thus the fallowing equation was used for the SpO2 Calculations [7]:

$$SpO_2\,[\%] = \Delta O_2Hb/(\Delta O_2Hb + \Delta HHb)$$

All data were recorded from one human subject in a resting position. Furthermore, for cross comparison, the measurements were compared with a measurement performed with a commercial system Nellcor N-395 provided by the University Hospital Zürich.

All the recorded data were imported into MATLAB R2012b for further signal processing. Bandpass filtering between 0.5-2.5 Hz was applied in order to minimize movement artefacts and other noises. After the filters were applied, recorded data were used to calculate the SpO_2 values according to the description in paragraph 2.4. To extract the frequency of the heart rate, a Fourier transformation was performed. Heart rates and SpO2 results were smoothed with moving average algorithms.

5.3 Results and Discussion

5.3.1 Wearable long-term monitoring system

In order to maintain a good wearing comfort, which is needed for the long term monitoring, these medical textiles should be highly flexible. This allows the adaption of the textile patch to any complex body surface. The amount of fixation points of the embroidery influences the drapability of the fabric. A higher amount of this fixation points facilitate the production process, but on the other hand enhance the rigidity of the fabric. The ‘M’ shape embroidery pattern consisted of 9 fixation points while the ‘V’ shape pattern had only 5 fixation points (Fig. 27). The total amount of fixation points per sensor was therefore 486 for the ‘M’ type sample and 410 for the ‘V’ type sample.

In Fig. 30, the flexibility of the textile is demonstrated. In order to determine whether the embroidered fibres out-coupled the light efficiently, and if the rings were well separated,

the bundled optical fibres from each light-collecting ring were connected to a light source of a different colour. As can be seen from the image, the rings were well separated and light was out-coupled from the bends of the embroidered fibres. Furthermore, the three dimensional black ring prevented a light sort circuit from the out-coupled light of the outer rings to the optical fibres embroidered in the centre of the ring system. Such a short circuit would dramatically decrease the light pulsation amplitude, a parameter which has to be maintained as high as possible for measurements in pulse oximetry devices.

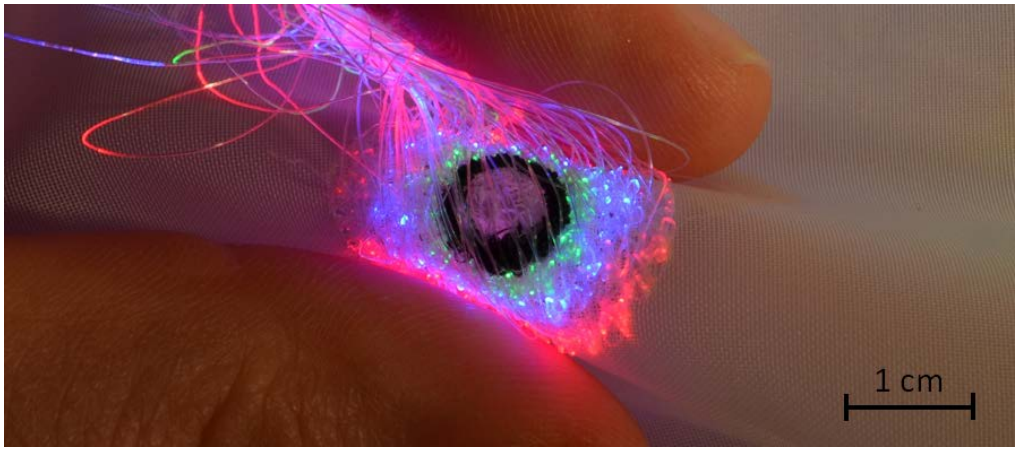

Fig. 30. A luminous textile used in this study is bent to show the flexibility of the fabric. The fibre bundles of each ring were connected to LEDs with different colours to illustrate the successful separation of the fibre bundles and the light out-coupling efficiency.

5.3.2 Efficiency of light in-coupling

To obtain a maximal signal to noise ratio, we determined, which sample has the highest light in-coupling efficiency. The measurements were conducted using the setup illustrated in Fig. 28. Firstly, the influence of the stitching pattern (‘M’ and ‘V’) was evaluated. The light in-coupling efficiency for the optical fibres embroidered in a ‘V’ shape was 35 % higher than when embroidered in an ‘M’ pattern. The reason lies in the enhanced number of ‘V’s being stitched in the patch compared with the ‘M’s: with the ‘V’ pattern 82 fibres could be stitched into the carrier fabric whereas for the ‘M’ patterned sample only 54 fibres

fitted in the same textile area. This effect over-compensated the launching efficiency of the increased in-coupling points of the ‘M’ pattern.

In the next step, the effects of carrier fabrics were assessed. Due to the higher rigidity of the fabrics with the ‘M’ pattern and the decreased efficiency, the fabric tests were performed with the optical fibres embroidered in a ‘V’ shape. As can be seen from Fig. 31, the matrix fabric, which led to the highest efficiency was the woven fabric. Nonwoven fabrics have a much higher yarn density than the woven fabric. As a consequence, the fabric material absorbed more of the out-coupled light.

Lastly, the surface modification of the optical fibres in order to enhance the coupling efficiency was assessed. As it can be noticed from Fig. 31, none of the studied surface modifications increased the efficiency. The first idea was to remove the cladding from the fibres in the area where the textile would be in touch with the tissue. A higher efficiency was expected due to direct optical contact of the fibre’s core with the tissue. However, fabric RC_WV had a light coupling efficiency, which was 63 % lower than the untreated patch V_WV. The cladding of the optical fibres was removed by applying a mechanical force in the presence of organic solvent (acetone). The cladding material THV is well soluble in acetone whereas the Zeonor core material is not [solubility information was provided by manufacturers of the polymers]. It was empirically proven that this solvent did not dissolve the polymer of the core. However, this treatment negatively influenced the light transmission parameters.

Roughening the surface (SR_WV), which mainly consisted in producing big numbers of micro cracks and ditches that would act as light coupling areas, decreased the efficiency by nearly 75% compared to the most efficient non-treated fabric V_WV.

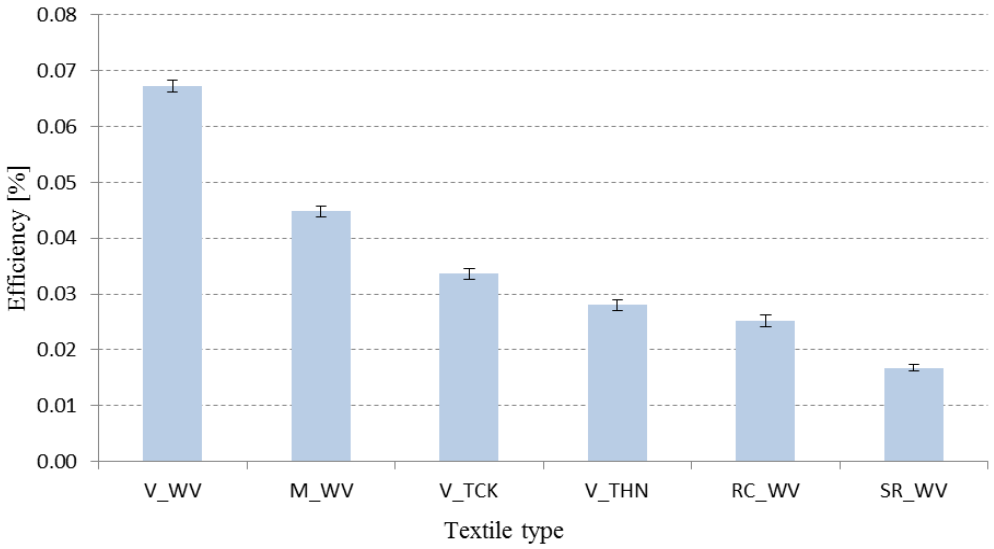

Fig. 31. Efficiency of light coupling into photonic textile with its standard deviation (n=5)

5.3.3 Measurements of pulse waves and of the oxygen saturation

In Fig. 32 time traces of light absorbed in the tissue together with calculated heart rate and blood oxygenation are shown. Parts (a), (b), and (c) represents data acquired from each individual ring (first, second and third ring respectively, counting from the centre of the ring system as illustrated in Figure 26). The measured data were compared with the data obtained from a commercial Nellcor sensing system. The oxygen saturation levels for all measurements were in the range of 92-98 %, which are expected values for healthy human beings [149]. The biggest deviation between the commercial Nellcor sensing system and the proposed sensor were detected in the SpO2 measurement (a). In the first 15 seconds of this measurement a miscorrelation of results of up to 5 % (92% for textile based system and 97% for commercial device) was observed. This miscorrelation were also observed for the recorded pulse. This effect can be explained by a low signal to noise ratio, which is due to the small amount of optical fibres (18) collecting light in the first ring. After about 15 seconds of this measurement the data correlated better and eventually showed a very good correlation (less than 1 % deviation). However, the obtained heart rate values from the two instruments correlated much better. Fewer artefacts were observed in measurement (b), from the middle ring (ring 4 in Figure 26) where 28 optical fibres were collecting light.

During the first 10 seconds, signal from proposed textile system underestimated the SpO2 value by 2% during which a lot of noise was present. Pulse data correlated well however, between 15 and 20 seconds, an increased deviation of 7 heart beats per minute was observed. As for the measurements of the first two rings, for ring 4 (measurement c) an enhanced amount of noise was present at the beginning of the measurement, which prevented the determination of the SpO2 value during the first 5 seconds. For measurements (c) and (d) the variation of the SpO2 signal was below 1%. For these measurements more optical fibres were used (36 optical fibres for (c) scenario and 82 for (d) where all three rings were combined for launching the light), which underlines the fact that the more optical fibres are used the better accuracy can be obtained.Reasonable agreement was obtained for the values collected from rings b), c) and d).

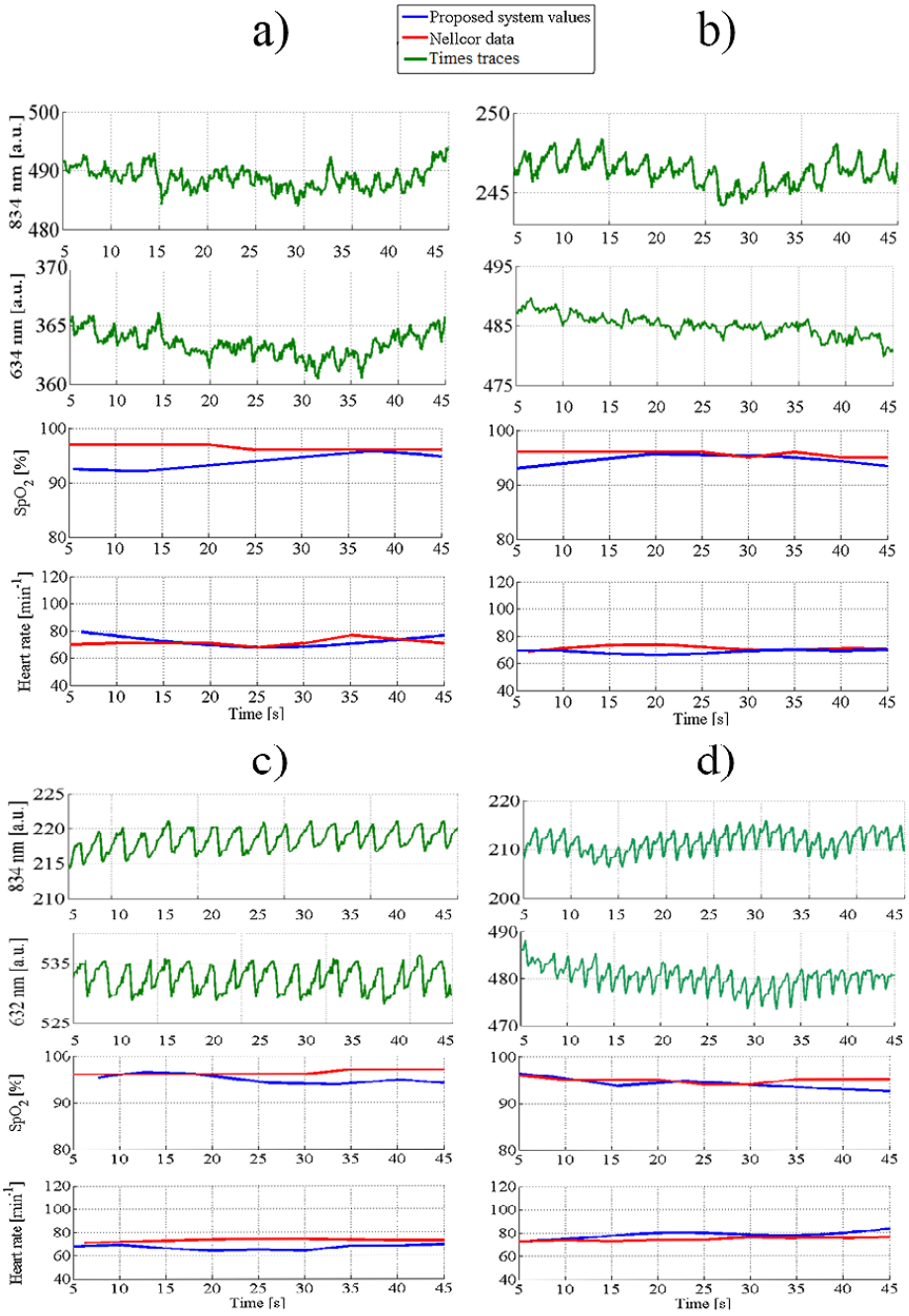

Fig. 32. Graphs presenting time traces of light absorption in the tissue together with calculated heart rates and blood oxygenation are presented. Parts (a), (b) and (c) represent measurements form rings 2-4 (Figure 26) respectively; and in (d) the fibres of all three rings were combined.

5.3.4 Conclusions

In this paper, a fully textile-based pulse-oximeter was presented. This photonic textile work in reflection mode, which makes them very versatile for wearable long-term monitoring and allow the measurements in different parts of the body like forehead, chest, arms, etc.

Furthermore, the presented fabric has the haptic of conventional fabrics and thus enhances the acceptance of the wearer, which is necessary for long-term monitoring purposes. The data were additionally crossed compared with commercial device and showed good correlation once enough fibres were used to collect the outcoupled light.

The same principle can be used for near-infrared spectroscopy to monitor the perfusion in the tissue. This is of great importance to monitor the perfusion to detect decubitus as early as possible, and where flexible textile-based sensor solutions are required. Further work implies the miniaturization of the electronic components to obtain a fully wearable sensing system.

5.3.5 Acknowledgements

This work was financially supported by NanoTera (TecInTex). Gratefully acknowledged is the support of Michel Schmid, Joanna Frackiewicz Kaczmarek and the valuable scientific discussions with Damien Ferrario and Josep Solà.

5.3.6 Supplementary information - Stitching protocol

St. Gallen 17.01.2013

Pattern used: tt0183_7_1 (Forsterrohner code name)

Stitching should start at different point than sample in order to have good quality of 3 dimensional black ring

Once the black ring is finished bobbin with black yarn should be taken out, otherwise black yarn will be integrated into the sample

Fabric used: “FRTT1022 PES……..”

Needle used 4 RS/SPI nr “3770120137”

Shuttle parameters:

Typ: Saurer

Tension: 85 gr.

Bobine: 80/2 Pes. Weiss

Embroiderytest with Fibre 738 Fabric Vlies 140 gr.

24.01.2013 Maschine works well

24.01.2013 Die Spulen mit wenig Fadenmenge weisen Fibrillenverletzungen auf

31.01.2013 Stickversuche mit neuer Faser ?(schwarzer Plastikkörper) Faser kann nicht gestickt werden. ➔ Fasern auf der Rolle gekreuzt abgerissen etc.

Stickversuch FRTT201, ➔ bricht, Faser ist zu starr.

Produktion 2x Faser 738 laüft gut

Stickboden: FRTT1007, Vlies 70 gr.

In the next chapters different type of polymeric optical fibres was described. These optical fibres depicted high flexibility and were also intended to be used in textiles to form wearable sensing system, however for different application then the ones presented in in former chapter. Due to the new requirements their parameters had to be optimized. Production, optimization, implementation in textiles and real application is described in the following chapters.

6. "Characterization of Flexible Copolymer Optical Fibres for Force Sensing Applications"

By Marek Krehel, René M. Rossi, Gian-Luca Bona and Lukas J. Scherer Sensors 2013, 13(9), 11956-11968.

Abstract: In this paper, different polymer optical fibres for applications in force sensing systems in textile fabrics are reported. The proposed method is based on the deflection of the light in fibre waveguides. Applying a force on the fibre changes the geometry and affects the wave guiding properties and hence induces light loss in the optical fibre. Fibres out of three different elastic and transparent copolymer materials were successfully produced and tested. Moreover, the influence of the diameter on the sensing properties was studied. The detectable force ranges from 0.05 N to 40 N (applied on 3 cm of fibre length), which can be regulated with the material and the diameter of the fibre. The detected signal loss varied from 0.6% to 78.3%. The fibres have attenuation parameters between 0.16–0.25 dB/cm at 652 nm. We show that the cross-sensitivies to temperature, strain and bends are low. Moreover, the high yield strength (0.0039–0.0054 GPa) and flexibility make these fibres very attractive candidates for integration into textiles to form wearable sensors, medical textiles or even computing systems.

Keywords: force sensor; optical fibres; sensitive force sensor; flexible light guide

6.1 Introduction

Optical fibres-based sensors have numerous advantages compared to electrical or chemical devices, e.g. insensitivity to electromagnetic fields, water and corrosion resistance, compact size and light weight [5, 6]. Due to these benefits, optical fibre based sensors are used in numerous applications to detect changes in chemical and/or physical parameters [5, 7, 133-135]. Various methods to detect pressure using optical fibres are known. Wang et al. proposed a pressure sensor that employs the effect of photoelasticity [150]. Urban et al. designed a pressure sensor that relies on FBG lateral deformation [151]. Within the

Seventh Framework Programme “Ofseth”, optical fibres using optical time-domain reflectometry for distributed respiration measurement and optical fibres with long period gratings in microstructured POF were incorporated into elastic fabrics to measure the breathing rate and the breathing volume by measuring the changes in applied pressure[76, 152, 153]. The most common method to determine the pressure using optical fibres is by using fibre Bragg gratings [151, 154-156]. To implement optical fibre based pressure sensors into textile fabrics, the fibres should be highly flexible, which is not the case for glass-based fibres most often used for fibre Bragg grating based sensors. Moreover, sensors based on fibre Bragg gratings have to be single mode and are dependent on temperature, strain and pressure simultaneously and require compensation of some of the parameters in order to sense one of them [157, 158].

In this study, elastically deformable light pipes, so called multimode optical fibres which react to applied pressure by deflecting light in the fibre structure, are reported. Due to their high flexibility and their appropriate tensile strength (from 0.0033 to 0.0056 GPa), they are suitable for incorporation into textiles [55, 159]. Long-term body monitoring solutions using textile fabrics have been intensively studied in recent years [132, 160]. Plastic optical fibres have several advantages compared to textile electronics when wearing them close to the body, e.g., comfort, ease of movements, and reduced movement artefacts [159]. Since the electronics often involved in the proposed solutions often negatively influences the haptic of these textiles, flexible and smart fibres allow for the separation of the rigid electronics from the measured region and thus from the body. Possible body parameters which could be measured with the proposed solution are, e.g., muscles activity, motion detections or breath monitoring [161]. For technical applications, these pressure sensors can be used for counting occupied seats in airplanes, cars or for monitoring immobile patients in hospitals to prevent decubitus.

6.2 Experimental Section

6.2.1 Materials and Methods

All the polymers used were purchased from WackerChemie AG (München, Germany). The polymers were all from the Geniomer group and are copolymers containing a soft silicon part and a hard polyurethane part. Geniomer 100-HDS and Geniomer 100 consist of about 70% silicon and 30% polyurethane, while Geniomer 175 consists of only 10% polyurethane and 90% silicon and has a lower processing temperature than the two Geniomer 100 polymers. Geniomer 100-HDS is Geniomer 100 with the addition of highly dispersed silicate particles.

- Fibres Extrusion with Melt Flow Index

The transparent light pipes were produced by a melt flow index apparatus (MFI), model 7085.15a, provided by ZWICK (Ulm, Germany) with an external drawing engine. In Table 4 the extrusion parameters at which the fibres were extruded are shown. All tested materials were firstly dried in a vacuum oven for 8 h at 80 °C. 7 g were used for each test. Fibres made of Geniomer 100 were extruded with three different diameters. Since this material showed the best melt flow characteristics of all three polymers, the diameter of the light pipes could be easily varied with this polymer. Three different fibre diameters made of this material were studied: 0.45 mm, 0.75 mm, and 0.85 mm. Consequently, these optical fibres can support thousands of optical modes although the fibre does not feature an outer cladding to protect the surface from scratches or other defects.

Table 4. Summary of parameters used for the fibre extrusions

Material type	Fibre Diameter [mm]	Temperature [ºC]	Pre-worming time [s]	Load [kg]	Engine Speed [arbitrary units]
Geniomer 100	0.45	163	240	1.2	5–6
Geniomer 100	0.75	160	240	2.16	10
Geniomer 100	0.85	165	240	3.8	2–3
Geniomer 175	0.5	160	240	2.16	10
Geniomer 100-HDS	0.5	160	240	2.16	10

- Light Loss

The optical loss measurements were performed with the cut-back method [128]. The medical laser used therefore had a wavelength of 652 nm with an intensity of 100 mW and was provided by AOL Medical Instruments. The 1 m long fibres were connected to the mode mixer (coupled to the light source) using F-SMA connectors from Thorlabs GmbH (Newton, USA). The following equation was used to compute the light attenuation [58]. The optical loss measurements were repeated five times.

$$\boldsymbol{A = 10 \cdot log_{10}\left(\frac{I}{I_0}\right)} \quad (12)$$

Where: I - Input light intensity, I0- Output light intensity

The optical loss measurements were repeated five times. Intrinsic losses over a whole visible spectrum range from 300 nm to 750 nm of Geniomer 100 were performed using a Lambda 900 UV-VIS spectrophotometer provided by Perkin Elmer. The spectrometer measures continuously and independently (by means of beam splitting) the intensity of the reference beam and uses the value to compute reflection or transmission coefficients. To determine the intrinsic loss of the copolymers (Figure 34), a polymer cube with the dimension 50 × 10 × 5 mm3 was formed, shown in Figure 33.

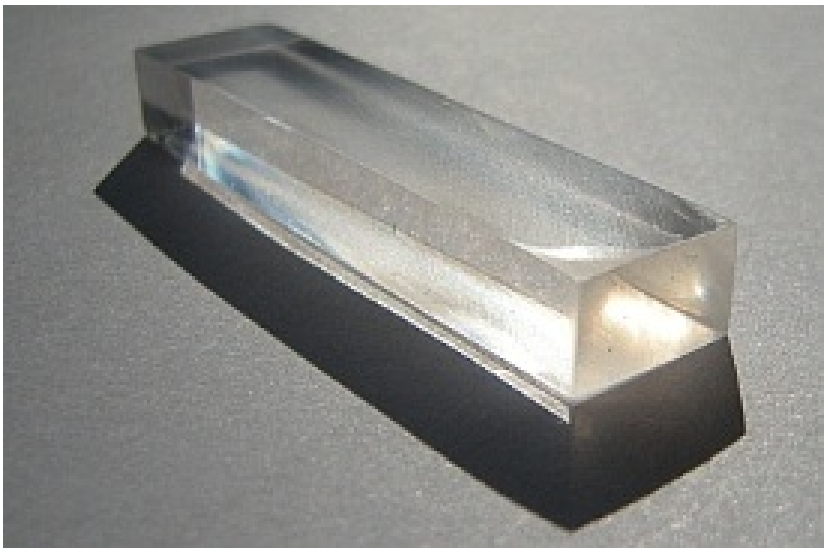

Figure 33. Polymer cube used for measurements of intrinsic light absorption of materials.

First the Fresnel reflection coefficient of the material was measured. This was done by measuring the light transmission through the thinnest part of the sample (5 mm), where the light absorption could be neglected. Afterwards, the light transmission through the 50 mm part was measured. The spectrophotometer was set to give the light transmission values from 300 nm to 750 nm in steps of 1 nm. For the force measurement setup, the extruded fibres were connected via a mode mixer to a Halogen-Deuterium Lamp model L10290 provided by Hamamatsu Photonics K.K. (Hamamatsu City, Japan), with SMA 905 connectors. In order to achieve flat fibre facets for good light coupling efficiency, fibres were cut with unused scalpel blades. Due to the elastic behaviour of the fibre material, polishing was not performed [17]. The ends of the fibres were connected by custom developed connectors to the measurement head RW3701-2 (Gigahertz Optik, Türkenfeld, Germany) and the outcoming light was measured using an Optometer P9710 detector (Gigahertz Optik). The force was applied with a Zwick INSTRON tensile testing machine model 4502 over the length of 3 cm. To study the influence of the temperature on the sensing system, the optical fibres were heated by a hot plate (Heidolph D-91126 type: MR Hei-Standard, Schwabach, Germany) and monitored by a temperature controller (Heidolph

type: EHT Hei-Con). As a light source, an LED IFE97 and as a detector a photodiode IFD91 were used, both provided by Industrial Fibre Optics (Tempe, USA).

6.3 Results and Discussion

6.3.1 Optical Properties of the Extruded Optical Fibres

The force sensor is based on the losses in light transmission along the light guides when the fibres are compressed. Thus it was essential to check whether the extruded fibres have reasonable light transmission parameters, i.e. low optical losses. Since the final goal is to incorporate the fibres to medical textiles with a max. length of 1 m, the maximum light attenuation should not exceed 0.2–0.3 dB/cm at 652 nm. Light losses at this level allow the detection of the transmitted light of a 1 m long light guide.

- Light Attenuation

In Table 5, a summary of light attenuation measurements at 652 nm is listed. No significant differences between the different materials and different diameters were observed. The optical signal loss varied between 0.16 and 0.25 dB/cm. That means that all fibres produced with the MFI apparatus were suitable for light transmissions over short distances of up to 1 m.

Table 5. Summary of light attenuation measurements of the fibres produced in this study.

Type of a Fibre	Light Attenuation [dB/cm]	σ [1][dB/cm]
Geniomer 100-HDS d = 0.5 mm	0.25	0.09
Geniomer 175 d = 0.5 mm	0.19	0.07
Geniomer 100 d = 0.75	0.22	0.06
Geniomer 100 d = 0.85 mm	0.20	0.09
Geniomer 100 d = 0.45 mm	0.24	0.12

[1] Standard deviation.

- Intrinsic Light Absorption Spectrum Measured at 652 nm

Figure 34 shows the intrinsic absorption spectrum of the light guide made of Geniomer 100-HDS as explained in paragraph 5.2.2, Since the overall attenuation of the light pipes was much higher (Table 5), the main light loss was due to extrinsic losses caused by the extrusion process (irregular fibre surface, bubbles or other inhomogeneities in the material). The absorption spectrum of Geniomer 100-HDS showed a local absorption band at around 635 nm, which corresponds to the 6th overtone of the C–H vibrations [24]. In the range of 660–700 nm, the absorption became lower than 0.01 dB/cm. Below 450 nm and above 700 nm the material starts to absorb strongly.

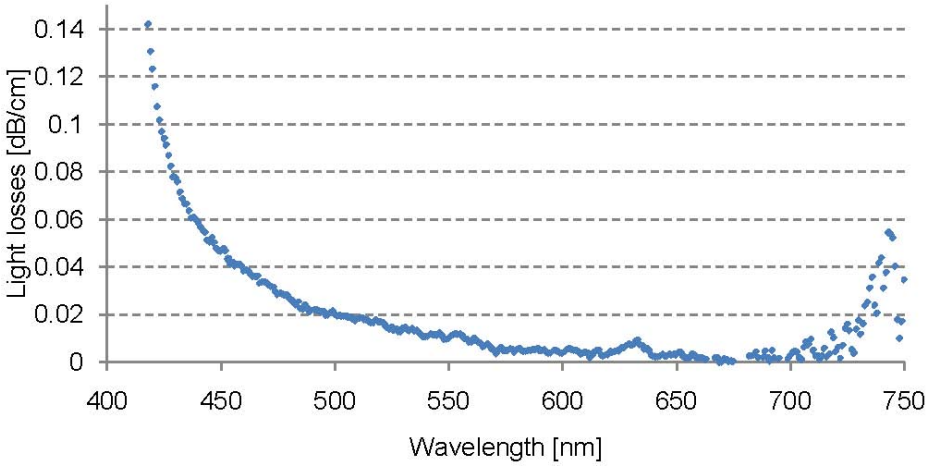

Figure 34. Intrinsic losses of the Geniomer 100-HDS polymer copolymer (measured from a polymer cube).

6.3.2 Force Sensing

The force sensing setup is presented below in Figure 35. The signal was measured from the middle of the three fibres. The outer fibres were used to support the weight.

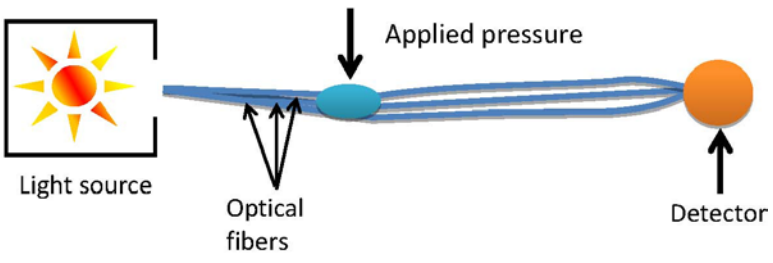

Figure 35. Force sensing setup.

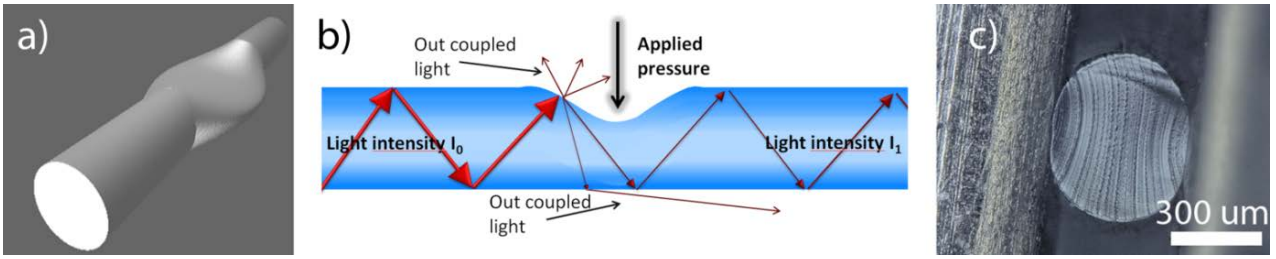

Figure 36. (a,b) Show schematically the influence of applied pressure on the elastic optical fibre. In (c) The cross-deformation of the fibre is demonstrated with a micrograph.

In Figure 36, a scheme representing the pressure sensing principle is shown. The applied force resulted in an elliptical deformation of the fibre cross section. From the side projection a kind of cavity was observed, as schematically illustrated in Figure 3. This deflection increased the out-coupling of the light in the region under pressure due to the geometrical deformation of the fibre. Since the degree of deflection was directly related to the applied force, the force could be quantitatively determined.

From the strain-stress curve (Figure 37) it can be concluded that the fibre made of Geniomer 175 had a smaller elastic modulus than the fibres made of the other two Geniomer materials and thus should have the highest response for applied pressure. The Young moduli of Geniomer 100 and Geniomer 100-HDS are similar and big differences in the light transmission could not be observed while applying pressure. However, the strain-stress curve was measured along the fibres and not perpendicularly (as the force was applied) which can cause a discrepancy between young moduli and the drop in light transmission

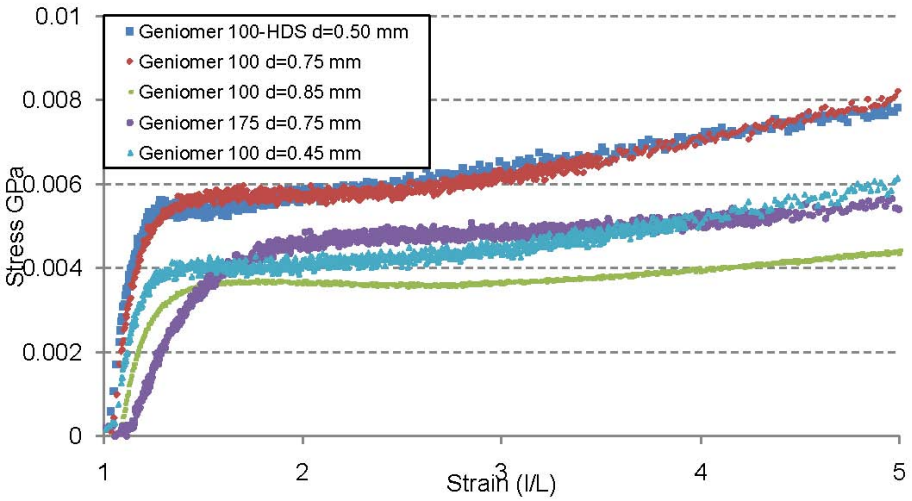

Figure 37. Stress strain curve of the different fibres produced in this study. The fibres made of Geniomer 175 show the lowest young's modulus.

Table 6. Yield strength of the extruded fibres.

Copolymer Type	Yield Strength [GPa]	σ [GPa]
Geniomer 100-HDS d = 0.5 mm	0.0054	0.0002
Geniomer 175 d = 0.5 mm	0.0045	0.0001
Geniomer 100 d = 0.45 mm	0.0039	0.0001

The force sensing experiments were conducted with the three different types of fibre materials. In order to check the repeatability, the measurements for each force were repeated three times. Each time the force was applied, it was completely released afterwards to check if the geometry of the fibre relaxed completely to its initial state. Firstly, the force of 1 N was applied three times to check whether the fibre was sensitive to the force at this level. The forces were then increased with increments of 10 N until the normalized signal output after releasing was below 90% of the original signal. If the signal did not recover 100%, the fibre was deformed not only elastically but also plastically. If the original shape was not recovered it was a sign that plastic deformation occurred [162]. The stress which is needed to start the plastic deformation is defined as the yield strength which was different for the three materials (Figure 37).

Table 7. Summary of force influence on light transmission.

	Polymer type	Diameter [mm]	Force [N]	Normalized signal	σ	Normalized signal after releasing force	σ
1	Geniomer 175	0.5	0.05	99.4%	0.1%	100.0%	0.0%
			0.1	98.8%	0.1%	100.0%	0.0%
			0.2	97.8%	0.0%	100.0%	0.0%
			0.5	94.3%	0.2%	100.0%	0.0%
			1	79.2%	0.5%	100.0%	0.0%
			10	42.0%	0.4%	100.0%	0.0%
			20	25.0%	0.7%	91.5%	1.7%
2	Geniomer 100	0.45	1	90.9%	1.0%	100.0%	0.0%
			10	61.6%	1.4%	91.0%	2.5%
3	Geniomer 100-HDS	0.5	1	90.0%	0.3%	100.0%	0.0%
			10	55.1%	0.6%	100.0%	0.0%
			20	40.6%	0.5%	100.0%	0.0%
			30	30.4%	0.0%	95.8%	1.1%
			40	21.7%	0.0%	90.6%	0.9%
4	Geniomer 100	0.75	1	94.3%	0.2%	100.0%	0.0%
			10	71.3%	0.6%	100.0%	0.0%
			20	53.0%	0.5%	90.7%	0.3%
5	Geniomer 100	0.85	1	91.7%	1.4%	100.0%	0.0%
			10	71.4%	0.7%	100.0%	0.0%
			20	54.5%	0.5%	100.0%	0.0%
			30	43.1%	0.8%	95.6%	1.0%
			40	31.9%	1.1%	91.7%	0.9%

Depending on the copolymer material used for extrusion, the applied forces caused different light transmission responses (Table 7). This was expected due to the different yield strengths shown in Figure 37. Geniomer 100-HDS showed full reversibility up to 20 N and was therefore the material which was best suited for large forces. At the level of 30 N the signal went back to 95.8% ± 1.1%. Although the fibre did not relax completely at 30 N and 40 N, the measured signal after applying pressure was completely reproducible (σ = 0.0%) at these forces. Geniomer 100 and Geniomer 175 showed plastic deformation already at 10 N. Geniomer 100 did only reach 91% ± 2.5% of the initial signal after releasing from 10 N and was therefore the material with the lowest applicable forces for

the sensing system. The sensitivity of the applied force on the fibre deflection is related to the young's modulus of the material. As expected from the strain-stress curve, the fibre made of Geniomer 175 had the highest response to applied force, as shown in Table 7. The drop in the signal of 20.8% ± 0.5% for 1 N was twice as much than the fibres produced from Geniomer 100 and Geniomer 100-HDS as presented in Table 7 (Sections 2 and 4). Due to the highest sensitivity of the fibres extruded of Geniomer 175, these fibres were chosen to measure the smallest detectable force. Forces ranging from 0.05 N to 0.5 N were applied three times (over 3 cm fibre length). From Section 1 in Table 7 it can be concluded that all the measured forces were successfully detected and the measurements were fully reproducible ($\sigma = 0.0\%$). The smallest detectable force was as low as 0.05 N.

Since the light losses caused by the applied forces are associated to the fibre deflection, not only the polymer material but also the diameter of the fibre influenced the measurement range. This was demonstrated with the polymer Geniomer 100. By decreasing the fibre diameter, the fibres became more sensitive to the applied force. The fibre with the diameter of 0.85 mm was not sensitive enough at low forces (1 N) to get accurate and repeatable values as shown in Table 7. However, the thicker fibre showed a larger measurement window; forces of up to 40 N could be measured reversibly, while the thinnest fibre (0.45 mm) could only be used for forces of up to 10 N.

- Fibre Deflection Against Signal Drop

In Figure 38 the relative fibre deflections in the force direction vs. the signal drop of all fibres (different polymers and different diameters) are presented. Only the measurements with strictly elastic deformations were included in the figure. The measurements of the fibre deflection were performed simultaneously with the force measurements using the tensile testing machine. Figure 38 clearly shows that the signal drop is correlated to the fibre deflection, independently of the polymer material and the fibre diameter. This shows

that only the deflection in force direction influences the amount of the out-coupled light and that the elastic properties of the material has only a minor influence on the signal change. However, the sensitivity of the deflection towards the applied force is material dependent as shown above.

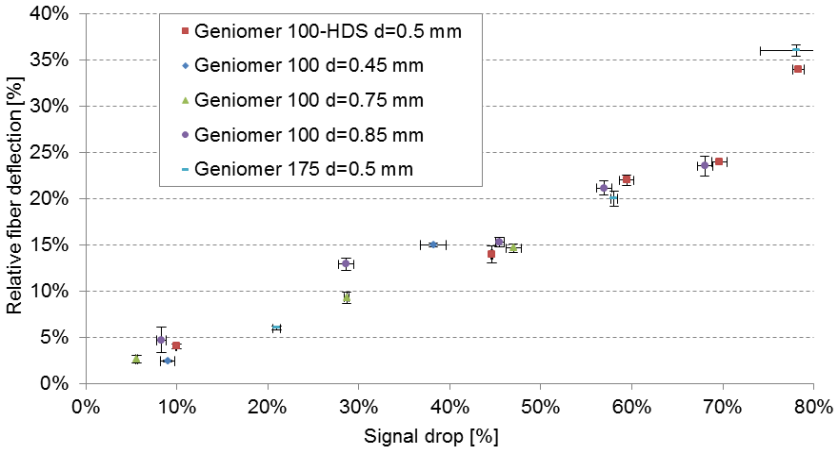

Figure 38. Fibre deflection vs. signal drop of fibres made of different materials and different diameters measured at 652 nm. Only the measurements with elastic deflections are shown.

- Cross Sensitivity

Since this sensing technique relies on intensity measurements, it is essential to assess the influence of other parameters that can influence the light intensity. Below, we describe the influence of axial strain and bend losses on the fibre. The motion artifacts are not taken into account since they can be filtered out with signal processing.

- Axial Strain Influence on the Sensor Signal

In order to determinate whether the sensor is cross sensitive to axial strain, the fibre made of Geniomer 100 (d = 0.75 mm) was stitched into a woven textile (code name FRTT1022; provided by Forster Rohner, St. Gallen, Switzerland) as presented in Figure 39.

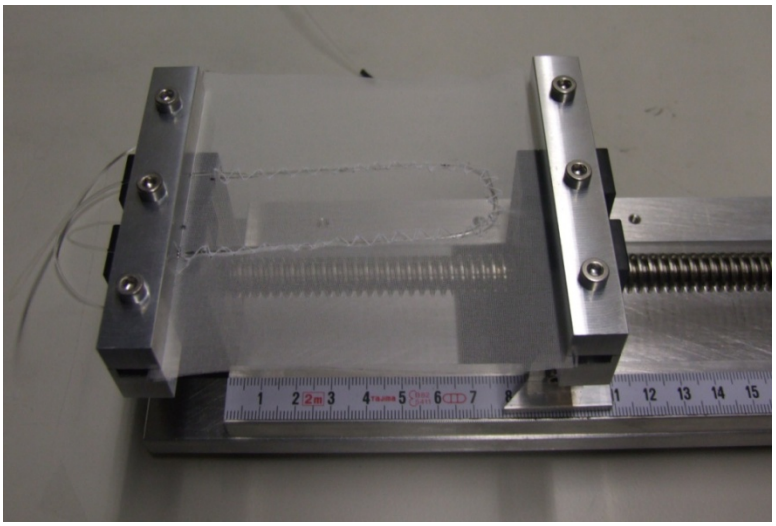

Figure 39. Measurement setup for axial strain influence.

According to the technical data sheet of this textile, the elastic deformation is 4%. The light intensity signal was measured simultaneously while the fabric was stretched with increments of 1.33%. In Table 8 the relative textile elongation vs. normalized signal is presented. It can be noticed that a loss in light transmission was detected when the fibre was stretched. At the maximum elongation of the fabric that was used, the signal dropped by 97% of the initial signal. This signal drop of 3% was lower than the signal drop of the smallest applied force in this study which was 1 N (signal drop of 5.7%). This leads us to the conclusion that axial strain would only influence the accuracy of the measurements at very low pressure. However, the influence of axial strain at low pressure can be bypassed by using a textile with a lower flexibility.

Table 8. Strain influence on the light transmission trough the sensor.

Relative Textile Elongation	Normalized Signal
0.00%	100.0%
1.33%	99.6%
2.67%	99.0%
4.00%	97.0%

- Bend Losses

To determine the influence of bend losses, the textile presented in Figure 39 was placed on three cylinders with radii 3, 5 and 6.5 cm respectively. Those numbers were chosen as the representative of human body parts: forearm, arm and thigh. In Table 9, the light loss vs. bend radius is presented. The signal when bended with radii 5 and 6.5 cm decreased less than 1%, which is most likely caused by applied pressure and contact with the cylinder. When the fabric was stronger bended with a radius of 3 cm, the light loss increased by up to ~3.5%. The reason of the light loss was a combination of loss caused by increased imprinting of the matrix textile to the elastic optical fibre and of optical bend loss. This could be minimized by placing a cladding on the core of this waveguide, which in turn would protect the core from textile imprints. However, even at this level, the light loss was relatively small (detectable forces start at around 5.7% light loss).

Table 9. Influence of fibre bendings on the relative light loss.

Bending Radius [cm]	Light Loss by Bending	σ	Light Loss when 1 N Force Applied	σ	Light Loss when 20 N Force Applied	σ
3	3.43%	0.24%	5%	0.4%	43.1%	0.2%
5	0.91%	0.26%	7.9%	0.4%	44.6%	0.3%
6.5	0.89%	0.93%	8.8%	0.4%	45.1%	0.6%

Table 9 shows the signal changes when a pressure was applied after the fibre was bent with a defined radius. As can be seen, the light loss was lower when the bending was narrower. The differences between the different radii became more significant when less force was applied.

- Temperature Dependency

All the three Geniomer materials used have a Tg of around −130 °C and therefore have no phase change at higher temperature due to the amorphic nature of these polymers. In order to check the temperature dependence of the sensing properties, the experiments were performed under different temperatures. A force of 3 N was always applied to the Geniomer 100-HDS fibre with a diameter of 0.5 mm to show the reversibility at a certain temperature. Since this sensing system is supposed to be integrated into medical textiles in close contact with human beings, the measurements of the light losses with applied forces were performed at temperatures ranging from 25 to 45 °C with intervals of 10 °C (Figure 40). As can be seen in Figure 40, the temperature had no major influence on the light loss of the fibre while a force was applied.

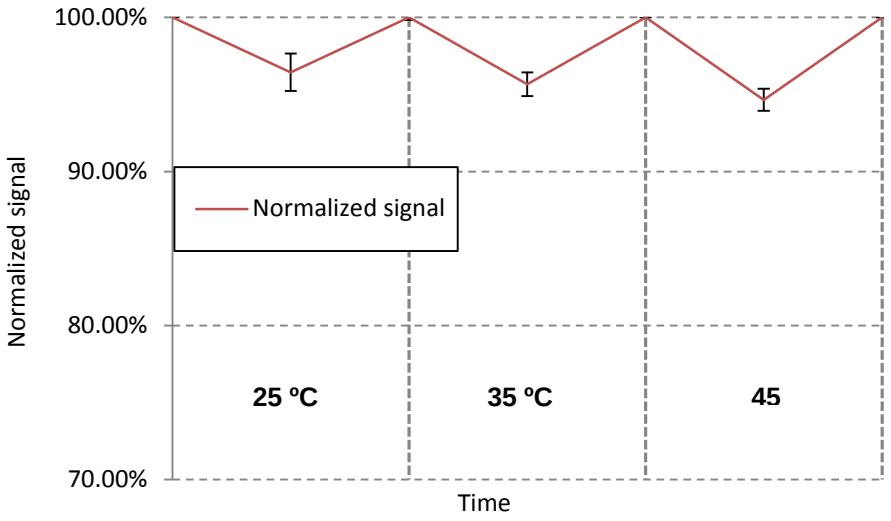

Figure 40. Signal dependency on the temperature. First, the attenuation was measured at a given temperature without applying any force. Then a force of 3 N was applied. The experiments were performed between 25 and 45 °C with 10 °C intervals and at a wavelength of 652 nm.

- Inaccuracy

Applied strain, bends and temperature change can influence the data. However, the accumulated errors should not exceed 10% of the signal change under the tested conditions. To determine for instance the breathing rate or to monitor the seat occupation, 10% of signal change would be acceptable. When detecting very low forces, as it would be the case for heart rate monitoring, the cross sensitivity becomes more important. Influences on the signal change have to be controlled by using other sensors (e.g. temperature sensor) or by controlling the environment of the fibre (e.g. avoiding of strain on the textile by using a non-elastic textile matrix). Since the optical power of LEDs is temperature-dependent, a control measurement may be necessary. The power fluctuation of the LED can be monitored by installing another LED of the same type for reference measurements into the measurement setup.

6.4 Conclusions

We demonstrate a simple way to manufacture force sensors based on light pipes in the form of multimode optical fibres made of copolymers. The working principle of the sensor is the use of the deflection of the fibre structure when a force is applied. By using materials with different young's modulus, the sensitivity of the material can be tuned according to the desired application in the range of 0.05–40 N over a fibre length of 3 cm. The fibres produced from Geniomer 175 are best suited for low forces, while the Geniomer 100-HDS fibres are ideal sensors for larger forces. Moreover, due to the flexibility and the high mechanical strength of the material, the proposed sensor can be easily integrated into textiles to form textile-based force sensors with possible applications as seat occupation monitoring in automotive or aeroplanes or as force sensors for medical applications (prevention for decubitus or breathing monitoring). Since the flexible fibres and not the electronics have to be placed on the measuring place, this sensing principle has no negative

influence on the flexibility and the haptic of the textile. Only one wavelength is used for the measurement, which simplifies the electronic system consisting of an LED and a photo detector like e.g. a photodiode. With a thin polymer cladding with a lower refractive index than the copolymer waveguide core, the robustness of the sensor could be improved further. Scratches and imperfections at the fibre surface would then not deteriorate or mask the sensing signal.

6.5 From flexible polymeric optical fibre based force sensor to respiratory rate monitoring.

In Chapter 6 we showed that the block co-polymers of PDMS and polyurethane can act as force sensors. Moreover, their sensitivity can be tuned by varying the thickness of the fibre and ratio of PDMS to polyurethane. Furthermore, we demonstrated that this sensor can be integrated into textiles and is not cross sensitive to high radius bends, which occur in human body. We also investigated the influence of temperature, and no significant changes were observed. Additionally cross sensitivity to axial strain was examined and no major signal changes were observed. Thanks to these advantages we could form a medical textile that was able to monitor respiratory rate. In the following chapter we describe real life application of how force sensing fibres investigated in Chapter 6 can be used to monitor respiratory rate. The most suitable fibre is chosen and different approaches signal-collection are presented. Lastly, the data from the most suitable sensing system is compared to a commercial system.

7. “Optical Fibre Based Sensor for Respiratory Monitoring”

by Marek Krehel, Michel Schmid, René M. Rossi, Luciano F. Boesel, Gian-Luca Bona and Lukas J. Scherer. Sensors 2014, 14(7), 13088-13101; doi:10.3390/s140713088

Abstract: In this paper, a textile-based respiratory sensing system is presented. Highly flexible polymeric optical fibres (POFs) that react to applied pressure were integrated into a carrier fabric to form a wearable sensing system. After the evaluation of different optical fibres, different setups were compared. To demonstrate the feasibility of such a wearable sensor, the setup featuring the best performance was placed on the human torso, and thus it was possible to measure the respiratory rate. Furthermore, we show that such a wearable system enables to keep track of the way of breathing (diaphragmatic, upper costal and mixed) when the sensor is placed at different positions of the torso. A comparison of the results with the output of some commercial respiratory measurements devices confirmed the utility of such a monitoring device.

Keywords: breathing monitoring; fibre optic sensing; respiratory rate; medical textiles; photonic textiles; technical textiles

7.1 Introduction

The respiratory rate is the frequency of breaths taken within a certain amount of time. This rate can vary depending on the need for oxygen. For instance, if the resting body starts to work, the respiratory rate increases. The respiratory rate is correlated to the gas composition in the blood, e.g., faster breathing can occur when the oxygen level is low and the carbon dioxide or the carbon oxide level is high. This means that an increased breathing rate can be caused by an increased carbon oxide concentration deriving from an infection [163]. Abnormal breathing rates can also be caused by other specific medical conditions that require medical attention, e.g., fever, dehydration, lung cancer, use of narcotics,

alcohol abuse, etc. [2]. Three types of breathing can be differentiated. (1) Diaphragmatic breathing: the main expansion is in the abdominal and lateral costal parts; (2) Upper costal breathing: chest expands the most; and (3) a mix of diaphragmatic and upper costal breathing. The first one is considered as optimal breathing since lungs can expand the most and thus the highest gas exchange can take place [4, 164]. Since the three ways of breathing lead to the expansion of different parts of the human torso, they can be distinguished by measuring the pressure change at different places of the torso.

To be able to better analyse and interpret the breathing rate, a solution for long-term monitoring is required. Attempts of monitoring systems lacked the desired comfort for patients and were thus not suited for long-term use [165].

A fibre optic fabric-based sensor system is ideally suited for long-term monitoring due to its enhanced comfort and versatility [55]. The other advantages of optical fibres-based sensors compared to electrical or chemical devices are their insensitivity to electromagnetic fields, water and corrosion resistance, and their compact size combined with low small weight [5, 6]. The insensitivity to electromagnetic fields is of great importance in the hospital environment where a lot of such fields are present [136]. This opens the door to the use of fibre optic fabrics during magnetic resonance imaging (MRI) and computed tomography (CT) examinations [5, 7, 133-135]. Recently researchers successfully developed MRI compatible sensors, for instance by means of a Plexiglas springboard which converts patients' movements to strain, and the latter is then measured by a fibre Bragg grating system [166-168]. Different approaches to measure the respiratory rate with optical fibres have been studied. Zieba et al. recorded changes in the distance between the light waveguide end and a sensor's head, which were caused by the chest movements [8]. Within the Seventh Framework Programme "Ofseth", optical fibres-based optical time-domain reflectometry for distributed respiration measurement and optical fibres with long

period gratings in microstructured POF were evaluated. They were incorporated into elastic fabrics to measure the breathing rate and the breathing volume [76, 152, 153]. Similar principles have been reported and a summary presented in [76]. Augousti et al. proposed a respiratory analysis by means of macro bending loss effects [169, 170]. Although most of the published work dealing with textile-based breathing monitoring systems show satisfactory sensing capabilities, their use in a medical environment is still limited by the poor usability of the sensors for the medical staff and the patient [76]. Furthermore, the high costs and the incompatibility with current industrial textile processes have hindered market entrance. The brittleness and the weak mechanical strength of optical glass fibres is an additional challenge when it comes to the textile integration of these fibres using an industrial process. Yoo et al. also showed respiratory rate measurements systems, but their systems, even if capable of being integrated into textiles, would be of very low haptic response. They used commercial optical fibers with additional springs and mirrors [171]. For wearable systems, simple and miniaturized electronics with small power consumption are necessary.

So far no one has reported a textile-based solution that would measure the respiratory rate by means of signal intensity changes and that would enable to distinguish between the three types of breathing. The elastomeric waveguides, which we have reported elsewhere [172], overcome the abovementioned comfort and industrialization problems. These waveguides react to applied pressure with a change in light intensity. In this study, we demonstrate the feasibility of using these elastic and flexible waveguides to measure the respiratory rate and to evaluate the type of breathing.

7.2 Experimental Section

7.2.1 Materials and Methods

Four custom made optical fibres, varying in flexibility, were used to perform the measurements (Geniomer (Gm) 100 HDS d = 0.5 mm, Gm 100 d = 0.75 mm, Gm 100 HDS d = 0.8 mm and Gm 175 d = 0.5 mm). The optical fibres had attenuation parameters between 0.16 dB/cm–0.25 dB/cm at 652 nm. Moreover, their high yield strength (3.9–5.4 MPa) and flexibility allowed to manually integrate them into textiles. Comprehensive information about production and the characteristics of these fibres can be found in [172]. In order to integrate the fibres into a textile as illustrated in Figure 41, they were laced in a woven polyester textile, provided by Engelbert E. Stieger (Rorschacherberg, Switzerland).

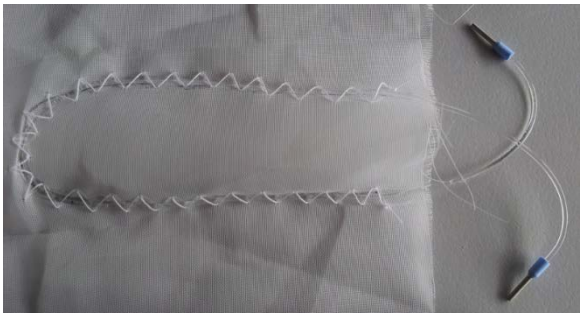

Figure 41. Picture illustrating the integration of the fibre into the textile to form the sensing setup, herein called “half oval”.

The sensing textiles were sewed on the inside of a custom developed chest strap which consisted of polyester textile, rubber straps and a buckle. Afterwards the strap was placed on a test subject (28 year old, male, 182 cm, 72 kg) as shown in Figure 42.

The scheme from Figure 42. Sensing system placed on a human subject study. Blue and black connectors are housings for the LED and the photodiode, respectively. The power supply is provided by the grey wires.

shows the driving and measuring electronics. As a light source, a red LED (660 nm) housed in connector (IFE99B) provided by I-Fiberoptics (Tempe, AZ, USA and a photodiode, enclosed in a connector (IFD91) with housing dimensions of 24 mm × 7 mm,

provided by the same company to detect the remaining light reaching the other end of the optical fibre. The device package features a micro lens for efficient light coupling. A 150 kΩ resistor was used to provide the gain in the signal and was changed depending on the signal strength. The MSR Data logger had a sampling frequency of 50 Hz. Total weight of light sources and electronics was below 100 g.

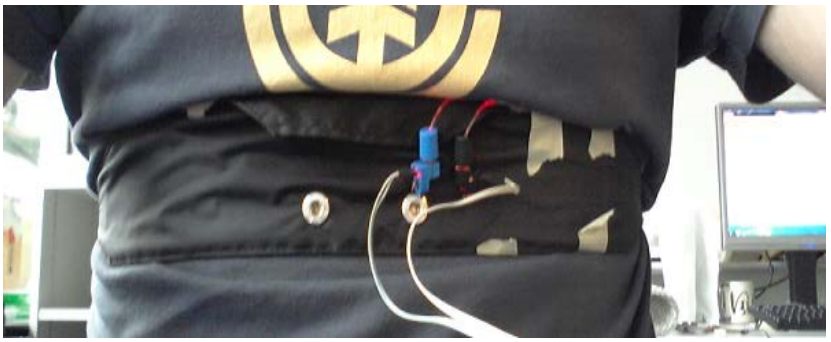

Figure 42. Sensing system placed on a human subject study. Blue and black connectors are housings for the LED and the photodiode, respectively. The power supply is provided by the grey wires.

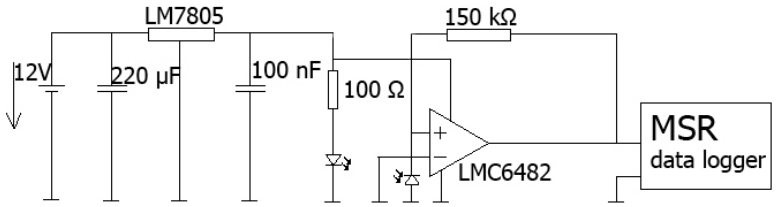

Figure 43. Sketch illustrating the electronics used to power the LED, and to amplify and to log the signal from the photodiode.

All the acquired data were evaluated in MATLAB R2012b.

7.2.2 Comparision of the Fibre Types

The performance of all four types of fibres was conducted in two scenarios, first with a slow breathing frequency (~6 breaths per minute), and secondly with a fast breathing frequency (~42 breaths per minute). The logged data was band pass filtered for respiratory rates between 5 and 60 respiratory cycles per minute. The measurements were all conducted with half oval form geometry of the fibre (Figure 41).

7.2.3 Comparison of Different Fibre Setups

Different setups from fibre Gm 175 d = 0.5 mm were tested. Firstly, the half oval form, as presented in Figure 41, with three different fibre lengths (240 mm, 180 mm, and 60 mm) were prepared. Afterwards, the half oval shape was additionally arranged with an additional meander consisting of 6 bends in the middle of the half oval, as presented in Figure 44. Two variations of this setup were prepared. In the first setup (shown in Figure 44a) the fibre was integrated without cross points; in the second setup (Figure 44b) the sensing fibre had six cross points (at the bends of each meander with the half oval).

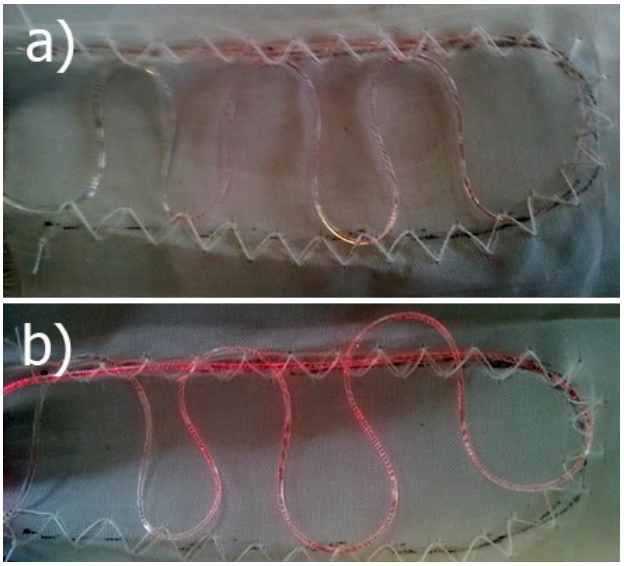

Figure 44. Picture presenting modification of half oval form. In (a) fibre was folded without cross points; whereas in (b) fibre crossing took place.

The last setup was a straight fibre wrapped around the chest with a chest strap (described in Section 2.1.). The measuring setup was the same as described in that section. Due to the weaker signals in these tests, the gain resistor was increased to Rgain = 1 MΩ. The measurement procedure was the same as described in section 2.1.1. In Table 10 all the tested fibre setups with their abbreviation are listed.

Table 10. Description of fibre types with their abbreviation.

Fibre Setup Type	Abbreviation	R_{gain} [k Ω]
Half oval, length 60 mm	HO_L = 60mm	150
Half oval, length 180 mm	HO_L = 180mm	
Half oval, length 240 mm	HO_L = 240mm	
Half oval with additional bends	HOAB	
Half oval with additional bends and crossing fibres	HOCF	
Fibre around the chest	FAC	1000

7.2.4 Comparison of the Sensing Positions

After having determined the type of optical fibre and the setup, the best position of the sensing textile on the human body was assessed. Following breathing scenarios were conducted to compare the sensing positions. Firstly, diaphragmatic and upper costal breathing (~6 breaths per minute) was performed, in which the human subject was asked to inhale a maximum possible amount of air. Secondly, the subject was asked to conduct upper costal breathing (~15 breaths per minute) under normal resting conditions. Thirdly diaphragmatic breathing (~12 breaths per minute) was performed.

This procedure was executed at different positions of the sensor on the torso. Three positions were on the front body: on a heart region (1); above the navel (2); above the left hipbone (3); as well as two on the back: below the left shoulder blade (4) and in the center of the back (5).

7.2.5 Cross Comparison with Commercial Device

Measurements from different positions on human torso were additionally verified with a reference measurement. Correlation measurements were conducted by the cardiopulmonary exercise testing instrument (SN808861, CareFusion, San Diego, CA,

US). While conducting cross comparison measurements, the following respiratory rates were monitored: 2 min of normal breathing (~15 breaths per minute), then 1 min fast breathing (~50 breaths per minute), followed by 1 min normal breathing. We also analysed the agreement between the two devices with Bland-Altman plots [173]. For that, we took several data points during the 4 min experiment. As the individual data points were not acquired at the same time intervals, interpolation of some of the data was required to create the plot.

7.3 Results and Discussion

7.3.1 Comparison of the Sensitivity of Different Optical Fibres

In order to determine the best suited fibre, all the samples were evaluated under slow and fast breathing conditions. Additionally, this allowed checking if the sampling frequency of the sensing system was fast enough. Normal respiratory rates for a healthy adult varies between 10 and 20 respirations per minute [174]. However, it can easily rise while e.g., performing sport activities [175]. Therefore, the sensing system was tested in the respiration rate that goes well beyond this number (respiratory rate frequencies of around 6 and of 50 breaths per minute were evaluated as well).

The quality of measurements is determined by the signal to noise ratio, which in turn means the stronger the signal the better the quality of the data output will be. In Figure 45 the measurements of two breathing conditions with all four types of fibres are presented. It was observed that changes in signal intensity in waveguides Gm 100 d = 0.75 mm and Gm 100 HDS d = 0.5 mm were very low for the slow breathing scenario (0.024 ± 0.06 V for Gm 100 d = 0.75 mm and 0.015 ± 0.03 V for Gm 100 HDS d = 0.5 mm). Both fibres Gm 100 HDS d = 0.8 mm and Gm 175 d = 0.5 mm exhibited higher signals (with amplitudes in the range of 0.06 ± 0.01 V for Gm 100 HDS d = 0.8 mm and 0.048 ± 0.03 V under slow breathing). In the fast breathing scenario, the signal from fibre Gm 100 HDS d = 0.5 mm

had no detectable peaks. Signal changes from fibres Gm 100 d = 0.75 mm and Gm 175 d = 0.5 mm were comparable and varied between 0.02 and 0.03 V. Highest signal amplitudes (while fast breathing) were obtained from fibre Gm 100 HDS d = 0.8 mm. However, it was noticed that the measurement signals from fibre Gm 100 HDS d = 0.8 mm featured more interfering frequencies under slow and fast breathing. Therefore, fibre Gm 175 d = 0.5 mm was chosen for further experiments due to the high signal strength and the lowest interfering frequencies.

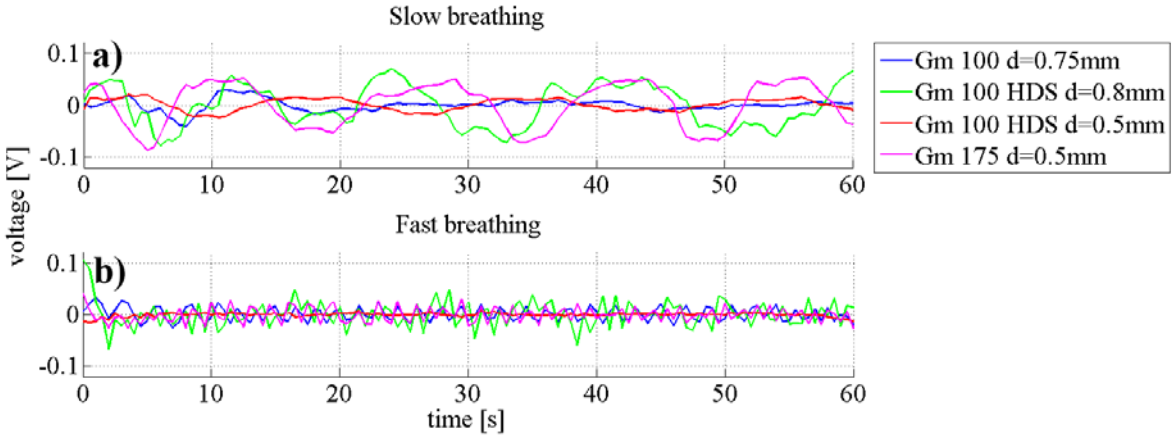

Figure 45. Graphs representing the slow breathing (a) and fast breathing (b) scenario. All four fibres types were measured for the two scenarios.

7.3.2 Comparison of Different Sensor Setups

The same tests described in Section 3.1.1. were conducted to determine the best geometry of the textile-integrated optical fibre. In order to only use one electronic device with the LED and the photodiode close to each other, the two fibre ends were always close to each other. Firstly, the samples with the half oval geometry were examined (fibre lengths of 240 mm, 180 mm and 60 mm, respectively). Different lengths were measured in order to find out what is the best length of the sensing waveguide that could be used. Secondly, the setup with additional bends was studied (HOAB).

It was expected that the additional bends would have a beneficial input on the sensitivity, because more fibre surface was in touch with the skin surface. Afterwards the setup HOCF

was studied. The setup HOCF differed from HOAB in that each of the additional bends from the meander crossed the main loop twice, which means the fibre had in total six cross points. Due to the additional pressure applied on these cross points, the sensor was expected to be more sensitive. Lastly, the setup with the waveguide wrapped around the chest was studied (FAC). This was the longest sensing waveguide in contact to the skin and since it surrounded the torso, breathing volume should be determinable with this sensing geometry.

In Figure 46a, the plots from different sensor setups when the subject was breathing slowly are presented. The signal strength for the FAC setup was the highest due to the amplification with a stronger resistor since the signal with the resistor used for the other fibre geometries was at the detection limit (1 MΩ vs. 1 kΩ, which makes a 6.7 times higher gain). This amplification also increased the artefacts, which were present as additional peaks that did not correspond to the respiratory rate. One prominent artefact (indicated by red arrow) signal appeared always a 5 s after the main breathing signal. It was a result of a back pressure applied against the back of the chair, and it was not present in the other scenarios since the sensing fibres were placed in front of the torso and thus no pressure was applied when the body was pressed against the chair. The signal from the sample HOCF had the lowest amplitude (0.015 V). This can be explained by the additional bends and crossing fibres, which highly attenuated the signal, whereas all other sensor setups showed very similar amplitude changes.

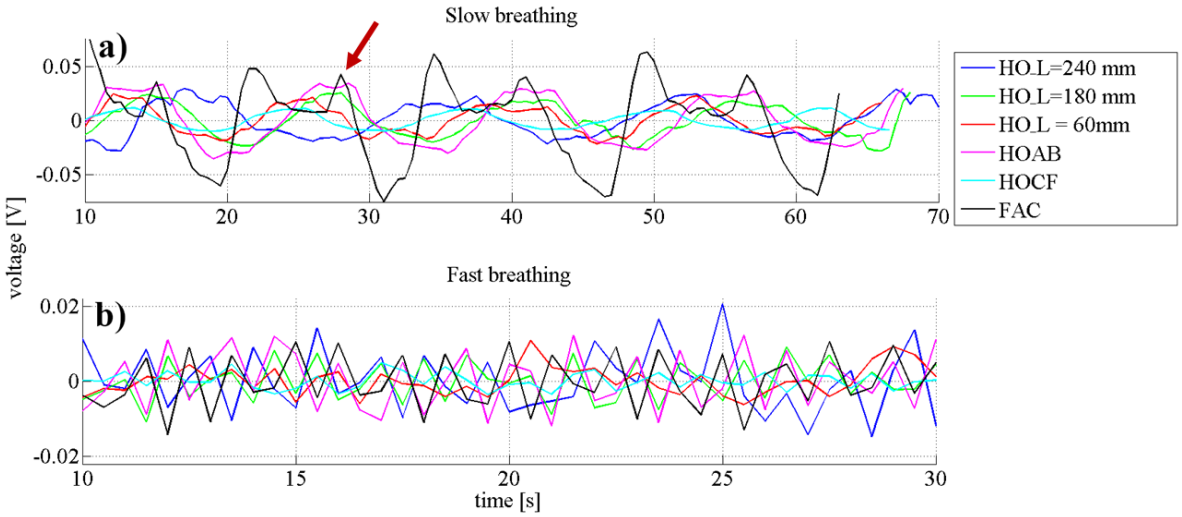

Figure 46. Graphs representing the data required to evaluate which sensor form is the best suited for respiratory rate measurements. On top slow breathing and on the bottom fast breathing.

In Figure 46b the graphs of the fast breathing scenario are presented. The plotting from the HOL_ = 60 mm was nearly flat and no peaks that would correspond to the respiratory rate were detected. All the other samples had similar amplitude changes in the range of 0.010 ± 0.03 V. Since the sensing textile HO_L = 180 mm had the lowest amount of interfering signals in slow breathing and had a comparable amplitude difference as the other samples while fast breathing, this geometry was chosen for further examinations.

7.3.3 Positioning of Sensors to Distinguish Different Types of Breathing

In order to find out what is the best place on human body to measure respiratory rate the measurements of three types of breathing types (diaphragmatic, upper costal and mixed breathing) were evaluated at five different positions on the human body (Figure 47).

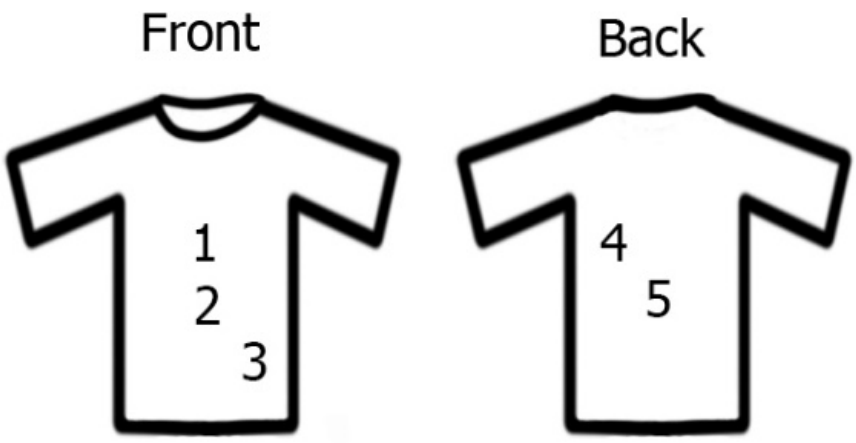

Figure 47. Positions of setup placed on subject study. On the front side: (1) on a heart region; (2) above the navel; (3) above the left hipbone; and on the back side: (4) below left shoulder blade; (5) in the middle of the back.

Figure 48 compares the measurements from the above-mentioned breathing types. Figure 8a presents the measurements while the subject was performing diaphragmatic breathing, the best signal change was obtained when the sensor setup was placed above the navel (position 2) (0.027 ± 0.003 V). Signal artefacts were not observed. As discussed in the introduction, the girth around the abdominal expands most during this type of breathing. This explains the highest detected pressure change while breathing when the sensor was placed on position 2. Peaks related to breathing frequency could also be detected when the sensor was placed on the middle of the back (position 5) with signal amplitudes of around 0.022 ± 0.04 V, interfering frequencies were not noticed in this scenario neither. Signal from setup placed at position 4 could be used for measuring the respiratory rate, however with very small amplitudes (0.013 ± 0.03V). No peaks corresponding to respiratory rate were found when the sensor was placed either above the heart (position 1) or above the hipbone (position 3).

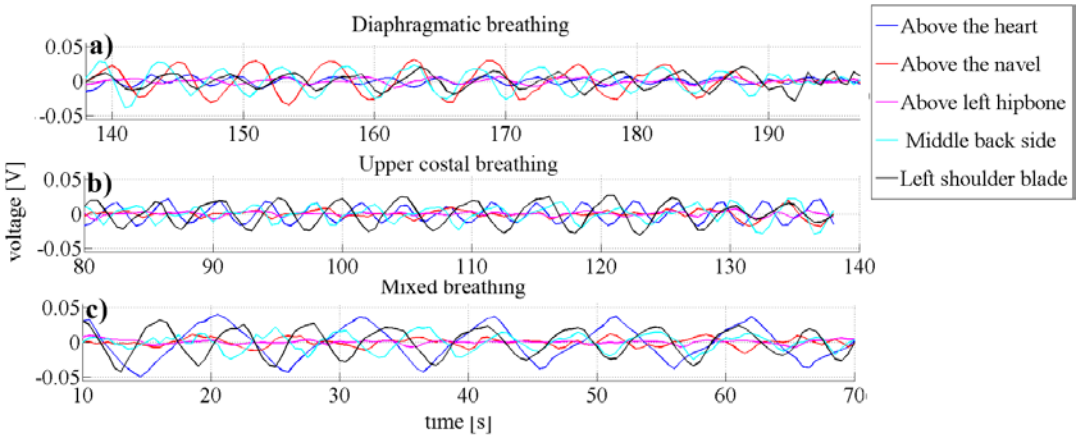

Figure 48. Graphs representing data from different types of breathing and data required to find out what is the best place on human body to measure respiratory rate.

Except setups placed on the position 1 the sensors reacted similar while upper costal breathing was performed (Figure 8b) as they did while diaphragmatic breathing, only with smaller amplitudes. The signal amplitude for sensors placed above the heart (position 1) was 0.017 ± 0.003 V and 0.021 ± 0.004 V for the sensor when placed below the left shoulder blade (position 4). The signal changes when the sensor was placed below the center of the torso (positions 2 and 3) were below 0.01 V and no respiratory related peaks could be detected. The low signal was expected, because the body changes the geometry during chest breathing mainly on the upper half of the torso (positions 1, 4 and 5).

It was ascertained that different types of breathing measured at the same place influence the amplitude of the signal. During mixed breathing presented in Figure 8c, the highest signal amplitude (0.036 ± 0.002 V) was obtained from the sensor placed above the heart (position 1). Furthermore, no interfering frequencies were observed. When the sensor was placed at position 4, slightly lower and artefact-free signals (0.025 ± 0.004 V) were measured. Weak signal changes were also observed from the sensor placed in the middle of the back-side (position 5), however the amplitude changes were not constant over time, which hinders long-term breathing monitoring. No peaks belonging to the breathing were

observed from sensors placed above the navel (position 2) and above the left hipbone (position 3).

To summarize, the positioning of the sensor has an influence on the signal amplitude and can therefore be used to distinguish the different types of breathing. For instance, when placing one sensing setup above the navel (position 2) and a second one above the heart (position 1) diaphragmatic breathing (position 2) can be distinguished from costal breathing (position 1). When both of these sensors react to respiratory changes, a mixed type of breathing is performed.

7.3.4 Cross Comparison with Commercial Device

The respiratory rate under regular circumstances (no infections, no sport activities) varies between 10 and 20 breaths per minute [174]. However, special events can elevate the breathing frequency close to 60 times per minute [175], and thus the results from our system were compared with a commercial, non-portable system in the range from 10 to 60 breaths per minute.

Figure 49 shows the collected data. The data sets arising from the commercial oxycon device correlated well with the one of the developed sensor. Looking at the “Above the heart” and “Middle back side” graphs, a delay in correlation can be noticed. This slight difference can be explained by the lower time resolution used to calculate the frequency using the short-time Fourier transform (STFT) to extract the respiratory rate from the measured data. A higher frequency resolution was chosen which led to the lower time resolution [176]. For long-term applications, the used time resolution is adequate since lowering of the power consumption is always a subject of wearable systems.

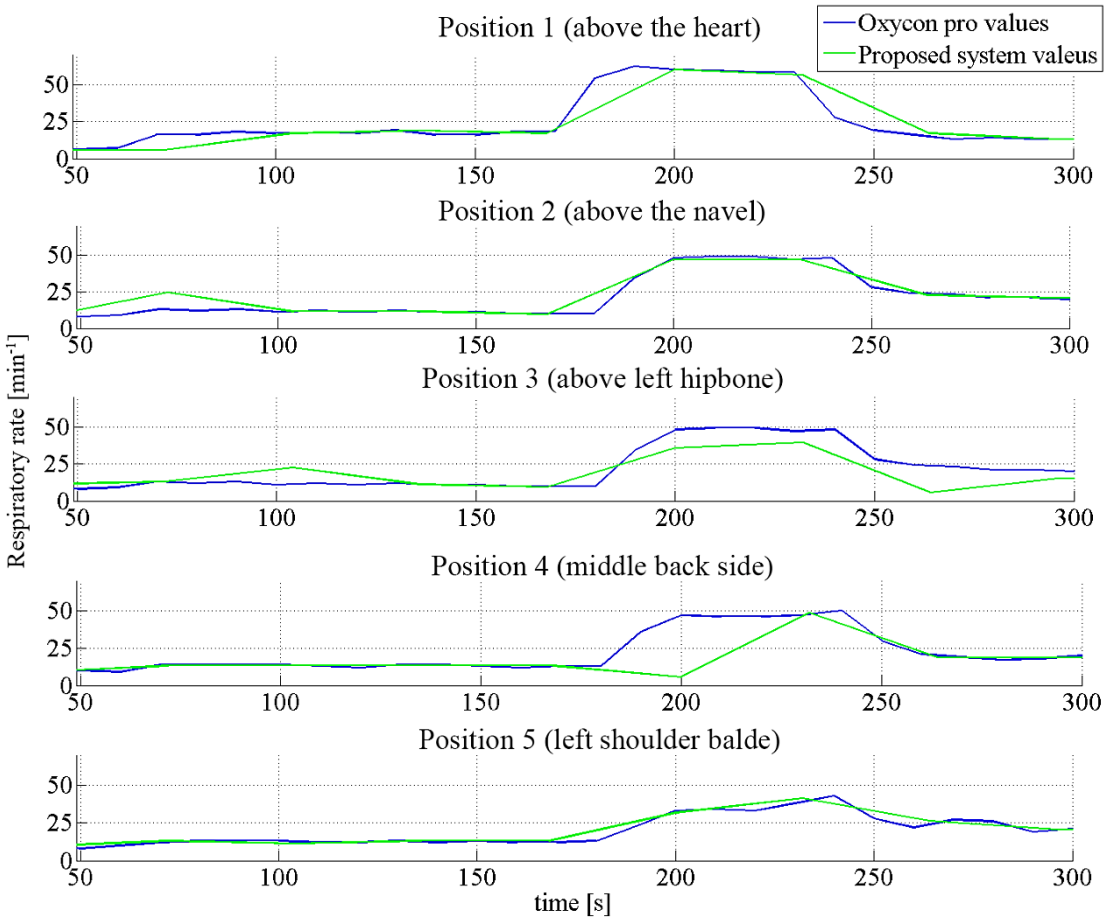

Figure 49. Cross comparison of respiratory data sets from our sensing system and from commercial device.

The low signal to noise ratio resulted in a slight underestimation of the frequency in the measurement setup placed above the left hipbone (50 vs. 40 breaths per minute) because not all breaths were recorded. It also underlines the results discussed in Section 3.1.3 where only for diaphragmatic breathing enough signal was obtained when the sensor was placed above the left hipbone.

Besides the discussed disagreement, the data correlate well in both slow and fast (respiratory rate frequency from 10 to 50 breaths per minute) scenarios. This is shown in Figure 50 for 2 of the 5 studied positions. We observe that the difference in both signals (from the oxycon device and the optical fibre sensor) is roughly constant over the whole duration of the experiment (4 min). Moreover, the differences in respiratory rate for these

two positions are mostly concentrated in the range of ±3 min−1 (with the exception of a few outliers).

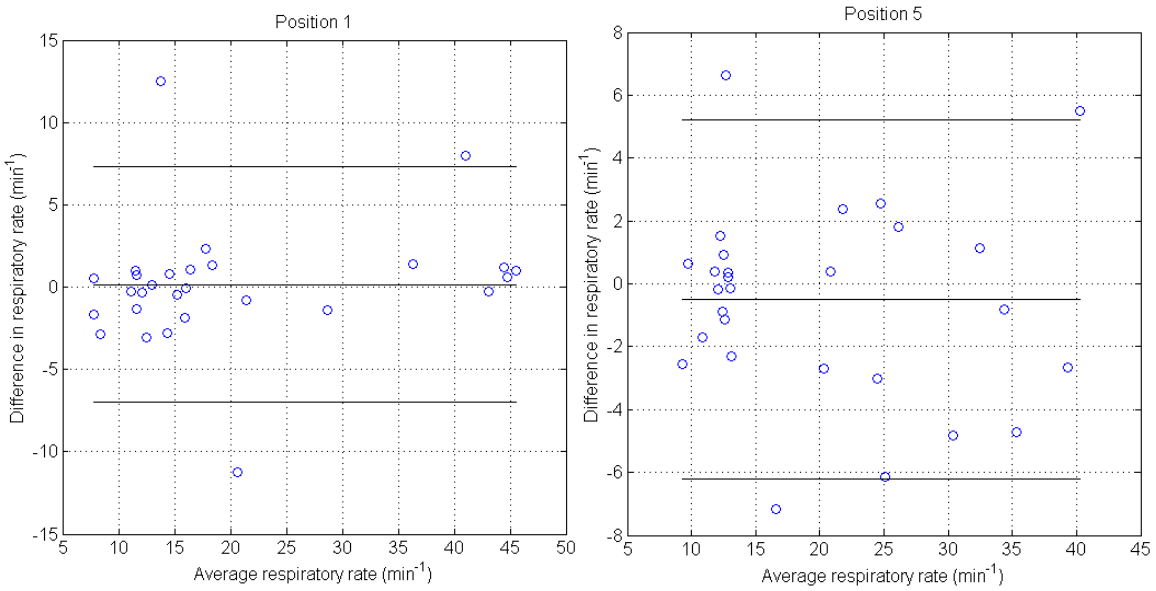

Figure 50. Bland-Altman plots comparing the results from respiratory rate of the oxycon device and our optical fibre sensor. Data taken from Figure 9. The three horizontal lines represent the mean ± 1.96 SD (standard deviation).

7.4 Conclusions

We demonstrate the feasibility of a fully textile, fibre optics based respiratory rate sensor. Comprehensive studies determined the best suited waveguide and integration geometry to create a breathing rate sensing device. Placing the fibre-based sensor on different areas of the human body showed that depending on the way of breathing, the signal amplitude was different at different positions. This opens new possibilities, such as by integrating two or more sensors in e.g., a T-shirt would allow obtaining information not only about the breathing rate, but also about the way of breathing. The obtained measurement data were additionally verified by comparing them with the output of a commercially available device, which showed good correlation. The flexibility of the sensing textile ensures a good haptic response, which for a wearable long-term monitoring system is crucial. The fact that the electronics do not have to be placed directly on the measurement place allows the adjustment of the rigid electronics on places with a lower disruption for the wearer.

Motion artefacts were not significant, thus simple filtering was satisfactory. If the sensor needed to be used under conditions with extraordinary movements, a compact size accelerometer would be used for signal to noise improvement. Furthermore, only one wavelength is necessary for the intensity-based sensor, which simplifies the electronics and allows the miniaturization to an accepted level.

Acknowledgment

This work was financially supported by NanoTera (TecInTex and Obesense). The support of Benno Wüst, Alexander Haag, Youna Maussion, and Jörg Gschwend is gratefully acknowledged.

8. Conclusion

The work of this dissertation has been focused on manufacturing new type polymeric optical fibres and integrating them in the textiles to develop so called medical sensing textiles. The main goal was to produce sensing medical textiles that would be accepted by patients in a long term monitoring situation due to their enhanced haptic and pleasant comfort. The outcome has two major findings.

Firstly, new type of POFs manufactured with cyclo-olefin polymer in the core and the fluoropolymer in the cladding by bi component melt spinning plant have very promising performance for applications in future in textile sensing. This happens due to their enhanced flexibility in bending while maintaining its strength and possibly low price. We have successfully embroidered these POFs in textiles and formed luminous textiles. These produced luminous textiles acted as light guides from a sources and light detectors. Consequently, the light could be delivered and collected to and from human tissue. Therefore, a PPG demonstration with a clear signal was obtained. From the obtained PPG, by means of the modified Beer-Lambert law, pulse oxygen saturation and heart rate were assessed. In addition, the data acquired from our textile based system were compared with commercial standards and showed reliable correlation. Engineers and researchers must ensure that the embroidered samples have the highest the possible light coupling efficiency, and thus signal-to-noise ratio is as high as possible.

Secondly, we showed that the manufactured, highly elastic, waveguides can be used to manufacture pressure sensitive textiles. These waveguides are not only simple in manufacturing but their sensitivity can be easily tuned as well. Moreover, since we propose an intensity based sensing system, simple electronics can be used (e.g. LED emitter and PIN photodiode). Therefore, this sensing system has the potential to be cheap, portable and easy in use. Furthermore, we proved that this textile sensor is capable of respiratory rate

monitoring function for humans. Additionally, by means of using multiple sensing patches, it was possible to differentiate between different types of breathing.

All textile based medical sensors made with our POFs had haptic as good as regular textiles, and thus show a high potential to be accepted by patients for long term monitoring, due to the superior comfort. Additionally, these fully textile based optical sensing systems, exhibit good correlation to industrial standards.

9. Outlook

Future research is planned regarding perfusion working towards a depth resolution of the tissue using optical sensing techniques. Namely, blood flow in the layers of the upper tissue and oxygen saturation values are intended to be measured.

Industrial development is planned to introduce the embroideries into textiles such as T-shirts, hats or socks, hence measuring the oxygen saturation of the torso, the brain or the legs, respectively, resulting in important progress of wearable monitoring devices for medical applications. Furthermore, introduction of a depth resolution of the oxygen saturation in tissue has been proposed and is currently being studied. Long term monitoring solutions require, besides high comfort, stability of the light coupling. Hence, consistency of the light coupling LED, photodiode and POFs should be studied and established. Moreover, when in contact with human skin the cleaning issue plays a role. If the same sensing system should be used by multiple patients a cleaning procedure needs to be established. Signal processing should be improved to obtain higher signal to noise ratio, and thus more reliable results. Additionally integration of an accelerometer into the system could provide data that could be used removing or minimizing motion artefacts. Once the signal to noise ratio is established as satisfactory, long term monitoring should be performed in order to prevent any type of unexpected complications with such measurements.

Concerning the force measurements a cladding material with proper refractive index should be implemented. Once the material is established a method to apply it, homogenously, on the core should be evaluated. It would be of a great advantage in order to prevent the core from mechanical damages such as scratches, cracks or dust.

Both above mentioned systems are planned to be employed in the ParaTex project funded by NanoTera program. Within the framework of this project, innovative sensing systems

are intended to monitor pressure, oxygenation and perfusion in 10 healthy patients and 10 paraplegic patients. The differences between healthy and paraplegic subjects are expected to bring new information regarding the origin of pressure ulcers. The study on human subjects has already been accepted by the ethical committee.

Regarding the respiratory rate, the integration of multiple sensing fibers connected to one devaice would be advantageous (lower weight, energy consumption and higher comfort). The signal could be easily separated by means of time multiplexing.

Concerning the material, further research on production the polymeric optical fibres is required. In order to produce good quality POFs from continuous extrusion systems a very good knowledge of polymers is required: new types of polymers could be developed for this application. The effect of parameters such as ambient humidity and temperature in the extrusion area should also be evaluated.

In any of the proposed sensing systems the weight of the electronics have to be minimized to maintain high wearing comfort. Since the heaviest part of the electronics is normally the battery, light pulsing could be used to minimize battery usage. Additionally, real life tests during MRI or CT examinations should be studied.

Once the above proposed improvements are achieved the sensors could and should be combined in the one textile patch. This in turn ought to be produced with the industrial standards and scale. As a result of industrialization the price of the device would significantly decrease and consequently the availability of the sensor would be significantly higher.

10. Acknowledgements

First of all I would like to thank my supervisor Dr. Lukas Scherer for his invaluable help while writing this thesis and the everyday supervision in Empa St. Gallen.

I would like to appreciate Dr. René Rossi for giving me the opportunity to work in the laboratory of Protection and Physiology.

Great acknowledgement goes to my university supervisors: Prof. Dr. Gian-Luca Bona and Prof. Dr. Martin Wolf for their suggestions and directions.

I would like to show my appreciation to Maike Quandt for the translation of abstract and for help when writing the introduction.

Many thanks go to Dr. Matthew Morrissey for English corrections and proofreading the thesis.

I would also like to show my gratitude to everybody who helped me with the measurements: Leonie El Issawi-Frischknecht, Dr. Patrick Rupper, Pierluigi Barbadoro, Jörg Gschwend, Eugen Zgraggen, and all the others with I unintentionally forgot to mention.

Many thanks go to people that made my life outside of Empa very pleasant: Nicolas, Alex, Matthias, Agathe, Andrej, Matthew and Gagik.

Last but not least I am very thankful to Martin Amberg for his great organisation of football games.

11. References

1. Light, in Encyclopædia Britannica Online. 2014.

2. Parkes, R., Rate of respiration: the forgotten vital sign. Emerg Nurse, 2011. 19(2): p. 12-7; quiz 18.

3. Volker, P., Ray Optics, Fermat's Principle, and Applications to General Relativity. 2000, Berlin, Germany: Springer.

4. Costa, D., et al., Participation of the sternocleidomastoid muscle on deep inspiration in man. An electromyographic study. Electromyogr Clin Neurophysiol, 1994. 34(5): p. 315-20.

5. Giallorenzi, T.G., et al., Optical Fiber Sensor Technology. Ieee Journal of Quantum Electronics, 1982. 18(4): p. 626-665.

6. Liehr, S., et al., Polymer Optical Fiber Sensors for Distributed Strain Measurement and Application in Structural Health Monitoring. Ieee Sensors Journal, 2009. 9(11): p. 1330-1338.

7. Rothmaier, M., et al., Photonic textiles for pulse oximetry. Optics Express, 2008. 16(17): p. 12973-12986.

8. Zieba, J., M. Frydrysiak, and K. Gniotek. Textronics system for breathing measurement. in 5th Central European Conference on Fibre-Grade Polymers, Chemical Fibres and Special Textiles. 2007. Warsaw, POLAND: Inst Chemical Fibres.

9. Bergstrand, S., et al., Existence of Tissue Blood Flow in Response to External Pressure in the Sacral Region of Elderly Individuals - Using an Optical Probe Prototype. Microcirculation, 2010. 17(4): p. 311-319.

10. Hagblad, J., et al., Assessment of the Optical Interference in a PPG-LDF System Used for Estimation of Tissue Blood Flow, in 15th Nordic-Baltic Conference on Biomedical Engineering and Medical Physics, K. Dremstrup, S. Rees, and O. Jensen, Editors. 2011, Springer: New York. p. 17-20.

11. Harlin, A., H. Myllymäki, and K. Grahn, Polymeric optical fibres and future prospects in textile integration. Autex Res. J., 2002. 2(3): p. 132-143.

12. Yeo, T.L., et al., Characterisation of a polymer-coated fibre Bragg grating sensor for relative humidity sensing. Sens. Actuators, B, 2005. 110(1): p. 148-156.

13. Yeo, T.L., T. Sun, and K.T.V. Grattan, Fibre-optic sensor technologies for humidity and moisture measurement. Sens. Actuators, A, 2008. 144(2): p. 280-295.

14. Folke, M., et al., Critical review of non-invasive respiratory monitoring in medical care. Medical and Biological Engineering and Computing, 2003. 41(4): p. 377-383.

15. Conde Pastor, M., et al., The influence of respiration on biofeedback techniques. Applied Psychophysiology Biofeedback, 2008. 33(1): p. 49-54.

16. Doi, K., et al., Lung injury following acute kidney injury: Kidney-lung crosstalk. Clin. Exp. Nephrol., 2011. 15(4): p. 464-470.

17. Hagblad, J., et al., Technical issues related to the long-term monitoring of blood flow at different depths using LDF and PPG. Physiological Measurement, 2012. 33(6): p. 985-996.

18. Nishyama, M., M. Miyamoto, and K. Watanabe, Respiration and body movement analysis during sleep in bed using hetero-core fiber optic pressure sensors without constraint to human activity. J. Biomed. Opt., 2011. 16(1).

19. Witt, J., et al. Smart medical textiles with embedded optical fibre sensors for continuous monitoring of respiratory movements during MRI. in Fourth European Workshop on Optical Fibre Sensors. 2010. Porto, Portugal.

20. Narbonneau, F., et al. OFSETH: optical technologies embedded in smart medical textile for continuous monitoring of respiratory motions under magnetic resonance imaging. in Biophotonics: Photonic Solutions for Better Health Care II. 2010. Brussels, Belgium.

21. Rull, G., Arterial Blood Gases - Indications and Interpretation. patient.co.uk, 2010.

22. K, M., Untersuchungen über die Sauerstoffsättigung des menschlichen Arterienblutes. 1935.

23. Wukitsch, M.W., Pulse oximetry: historical review and Ohmeda functional analysis. Int J Clin Monit Comput, 1987. 4(3): p. 161-6.

24. Severinghaus, J.W. and Y. Honda, History of blood gas analysis. VII. Pulse oximetry. J Clin Monit, 1987. 3(2): p. 135-8.

25. Svanberg, E.K., et al., Physiological influence of basic perturbations assessed by non-invasive optical techniques in humans. Appl. Physiol., Nutr., Metab., 2011. 36(6): p. 946-957.

26. Santos, S.A., B. Venema, and S. Leonhardt, Accelerometer-assisted PPG measurement during physical exercise using the LAVIMO sensor system. Acta Polytech., 2012. 52(5): p. 80-85.

27. Dumas, C., J.A. Wahr, and K.K. Tremper, Clinical evaluation of a prototype motion artifact resistant pulse oximeter in the recovery room. Anesth Analg, 1996. 83(2): p. 269-72.

28. Barker, S.J. and N.K. Shah, The effects of motion on the performance of pulse oximeters in volunteers (revised publication). Anesthesiology, 1997. 86(1): p. 101-8.

29. Barker, S.J., K.K. Tremper, and J. Hyatt, Effects of methemoglobinemia on pulse oximetry and mixed venous oximetry. Anesthesiology, 1989. 70(1): p. 112-7.

30. Barker, S.J. and K.K. Tremper, The effect of carbon monoxide inhalation on pulse oximetry and transcutaneous PO2. Anesthesiology, 1987. 66(5): p. 677-9.

31. Allen, J., Photoplethysmography and its application in clinical physiological measurement. Physiological Measurement, 2007. 28(3): p. R1-R39.

32. Guyton, A.C.J.E., Textbook Of Medical Physiology. 11th ed, ed. P.E. Inc. 2006.

33. Schiefer, J. Long Term Vital Parameter Monitoring (LAVIMO). 2013.

34. Schäfer, A. and J. Vagedes, How accurate is pulse rate variability as an estimate of heart rate variability?: A review on studies comparing photoplethysmographic technology with an electrocardiogram. International Journal of Cardiology, 2013. 166(1): p. 15-29.

35. Kokkinos, D., et al., Fiber optic based heart-rate and pulse pressure shape monitor, in Optical Fibers and Sensors for Medical Diagnostics and Treatment Applications XII. 2012: San Francisco, CA, USA.

36. Erlanger J, H.D., An experimental study of blood pressure and of pulse-pressure in man. Johns Hopkins Hosp Rep, 1904. 12: p. 145.

37. Verdecchia, P., et al., Variability between current definitions of 'normal' ambulatory blood pressure: Implications in the assessment of white coat hypertension. Hypertension, 1992. 20(4): p. 555-562.

38. Gupta, S.K. and S.H. Bodakhe, An elevated pulse pressure: A major risk factor for cardiovascular diseases. Asian Journal of Pharmaceutical and Clinical Research, 2013. 6(SUPPL.5): p. 5-11.

39. V., F.G.G., PPG-based methods for non invasive and continuous blood pressure measurement: an overview and development issues in body sensor networks I.S.D. Dept. of Electron., Univ. of Calabria, Rende, Italy, Editor. 2010: Ottawa, ON p. 10-13.

40. Teng, X.F. and Y.T. Zhang, Continuous and noninvasive estimation of arterial blood pressure using a photoplethysmographic approach. Proceedings of the 25th Annual International Conference of the Ieee Engineering in Medicine and Biology Society, Vols 1-4, 2003. 25: p. 3153-3156.

41. McCombie, D.B., A.T. Reisner, and H.H. Asada, Adaptive blood pressure estimation from wearable PPG sensors using peripheral artery pulse wave velocity measurements and multi-channel blind identification of local arterial dynamics. 2006 28th Annual International Conference of the IEEE Engineering in Medicine and Biology Society, Vols 1-15, 2006: p. 2824-2827.

42. P. Fung, G.D., C. Ries, C. Mott, M. Ansermino,. P. Fung, G. Dumont, C. Ries, C. Mott, M. Ansermino,. in San Francisco, CA. 2004. San Francisco, CA: IEEE.

43. Zheng, J.W., et al., A wearable mobihealth care system supporting real-time diagnosis and alarm. Medical & Biological Engineering & Computing, 2007. 45(9): p. 877-885.

44. Mak, A.F.T., M. Zhang, and E.W.C. Tam, Biomechanics of Pressure Ulcer in Body Tissues Interacting with External Forces during Locomotion, in Annual Review of Biomedical Engineering, Vol 12, M.L. Yarmush, J.S. Duncan, and M.L. Gray, Editors. 2010, Annual Reviews: Palo Alto, CA, USA. p. 29-53.

45. Kottner, J., A. Gefen, and N. Lahmann, Weight and pressure ulcer occurrence: A secondary data analysis. International Journal of Nursing Studies, 2011. 48(11): p. 1339-1348.

46. Anders, J., et al., Decubitus Ulcers: Pathophysiology and Primary Prevention. Deutsches Arzteblatt International, 2010. 107(21): p. 371-U33.

47. Aissaoui, R., et al., Analysis of pressure distribution at the body-seat interface in able-bodied and paraplegic subjects using a deformable active contour algorithm. Medical Engineering & Physics, 2001. 23(6): p. 359-367.

48. Hagblad, J., et al., A technique based on laser Doppler flowmetry and photoplethysmography for simultaneously monitoring blood flow at different tissue depths. Medical & Biological Engineering & Computing, 2010. 48(5): p. 415-422.

49. Rothmaier, M., M.P. Luong, and F. Clemens, Textile pressure sensor made of flexible plastic optical fibers. Sensors, 2008. 8(7): p. 4318-4329.

50. Yan, C., E. Ferraris, and D. Reynaerts, A pressure sensing sheet based on optical fibre technology. Procedia Eng., 2011. 25(0): p. 495-498.

51. Lim, T.K., et al. Measurement of contact forces between human and vibrating floors using fiber Bragg grating foot sensors. in Smart Structures and Devices. 2001. Melbourne, VIC; Australia.

52. Pleros, N., G.T. Kanellos, and G. Papaioannou, Optical fiber sensors in orthopedic biomechanics and rehabilitation, in 9th International Conference on Information Technology and Applications in Biomedicine, ITAB 2009. 2009: Larnaca; Cyprus.

53. Coyle, S., et al., Textile-based wearable sensors for assisting sports performance, in 6th International Workshop on Wearable and Implantable Body Sensor Networks, BSN 2009. 2009: Berkeley, CA, USA. p. 307-311.

54. Krupincová, G. and M. Meloun, Yarn hairiness versus quality of yarn. J. Text. Inst., 2013. 104(12): p. 1312-1319.

55. Selm, B., et al., Polymeric Optical Fiber Fabrics for Illumination and Sensorial Applications in Textiles. Journal of Intelligent Material Systems and Structures, 2010. 21(11): p. 1061-1071.

56. Wang, J.C., B.H. Huang, and B. Yang, Effect of weave structure on the side-emitting properties of polymer optical fiber jacquard fabrics. Text. Res. J., 2013. 83(11): p. 1170-1180.

57. Shen, J., et al., Light-emitting fabrics integrated with structured polymer optical fibers treated with an infrared CO2 laser. Text. Res. J., 2013. 83(7): p. 730-739.

58. Kuzyk, M.G., Polymer Fiber Optics. 2007. p. 97-98.

59. Kaino, T., K. Jinguji, and S. Nara, Low-Loss Poly(Methyl Methacrylate-D5) Core Optical Fibers. Applied Physics Letters, 1982. 41(9): p. 802-804.

60. Menachem Lewin, J.P., Marcel Dekker, High technology Fibers, part A, Handbook of Fiber Science and Technology. 1985. III.

61. Bower, D.I., An Introduction to Polymer Physics. 2002, Cambridge etc.: Cambridge University Press.

62. Michler, G.H., Kunststoff-Mikromechanik. Morphologie, Deformations- und Bruchmechanismen. 1992, München Wien: Carl Hanser Verlag.

63. Ziemann, O., et al., POF Handbook - Optical Short Range Transmission Systems. 2008, Berlin and Heidelberg: Springer Verlag.

64. Daniel, M., Light emitting fabric. United States Patent US 4234907 (A), 1980-11-18.

65. Koncar, V., Optical Fiber Fabric Displays. Optics & Photonics News, 2005. 16(4): p. 40-44.

66. Wilson, J.D., et al., Design of a light stimulator for fetal and neonatal magnetoencephalography. Physiological Measurement, 2009. 30(1): p. N1-N10.

67. Selm, B., et al., Novel flexible light diffuser and irradiation properties for photodynamic therapy. Journal of Biomedical Optics, 2007. 12(3): p. 034024.

68. Cochrane, C., et al., Flexible displays for smart clothing: Part I-Overview. Indian Journal of Fibre & Textile Research, 2011. 36(4): p. 422-428.

69. Bartlett, R.J., et al., Plastic optical fibre sensors and devices. Transactions of the Institute of Measurement and Control, 2000. 22(5): p. 431-457.

70. Zubia, J. and J. Arrue, Plastic optical fibers: An introduction to their technological processes and applications. Optical Fiber Technology, 2001. 7(2): p. 101-140.

71. Dhawan, A., T.K. Ghosh, and A. Seyam, Fiber-Based Electrical and Optical Devices and Systems. Textile Progress, 2005. 36(2): p. 1-84.

72. Boczkowska, A. and M. Leonowicz, Intelligent materials for intelligent textiles. Fibres & Textiles in Eastern Europe, 2006. 14(5): p. 13-17.

73. Tang, S.L.P. and G.K. Stylios, An overview of smart technologies for clothing design and engineering. International Journal of Clothing Science and Technology, 2006. 18(1-2): p. 108-128.

74. Diamond, D., et al., Wireless sensor networks and chemo-/biosensing. Chemical Reviews, 2008. 108(2): p. 652-679.

75. Zieba, J., M. Frydrysiak, and K. Gniotek, Textronics system for breathing measurement. Fibres & Textiles in Eastern Europe, 2007. 15(5-6): p. 105-108.

76. Grillet, A., et al., Optical fiber sensors embedded into medical textiles for healthcare monitoring. IEEE Sensors Journal, 2008. 8(7-8): p. 1215-1222.

77. Krebber, K., et al. Smart technical textiles with integrated POF sensors. in Proc. of SPIE Vol. 6933, Conference on Smart Sensor, Phenomena, Technology, Networks, and Systems. 2008. San Diego, CA.

78. Bilro, L., et al., Optical Sensors Based on Plastic Fibers. Sensors, 2012. 12(9): p. 12184-12207.

79. Krehel, M., et al., An optical fibre-based sensor for respiratory monitoring. Sensors, 2014. 14(7): p. 13088-13101.

80. Koike, Y. and K. Koike, Progress in Low-Loss and High-Bandwidth Plastic Optical Fibers. Journal of Polymer Science Part B-Polymer Physics, 2011. 49(1): p. 2-17.

81. Argyros, A., Structure, properties and characteristics of optical fibres, in Handbook of Textile Fibre Structure, Volume 2 - Natural, Regenerated, Inorganic and Specialist Fibres, S.J. Eichhorn, et al., Editors. 2009, Woodhead Publishing: Oxford. p. 458-484.

82. Abouraddy, A.F., et al., Towards multimaterial multifunctional fibres that see, hear, sense and communicate. Nature Materials, 2007. 6(5): p. 336-347.

83. N'Diaye, M., et al., Water Absorption of Poly(methyl methacrylate) Measured by Vertical Interference Microscopy. Langmuir, 2012. 28(31): p. 11609-11614.

84. Houis, S., F. Schreiber, and T. Gries, Fibre-Table according to P.-A. Koch: Bicomponent Fibres. Textile Technology, ed. T. Gries. 2008, Aachen: Shaker. 78.

85. Spruiell, J.E., Structure Formation During Melt Spinning, in Structure Formation in Polymeric Fibers, D.R. Salem, Editor. 2001, Carl Hanser Verlag: Munich. p. 5-93.

86. Hufenus, R., et al., Design and Characterization of a Bicomponent Melt-Spun Fiber Optimized for Artificial Turf Applications. Macromolecular Materials and Engineering, 2013. 298(6): p. 653-663.

87. Radhakrishnan, J., T. Kikutani, and N. Okui, High-speed melt spinning of sheath-core bicomponent polyester fibers: High and low molecular weight poly(ethylene terephthalate) systems. Textile Research Journal, 1997. 67(9): p. 684-694.

88. Shi, X.Q., H. Ito, and T. Kikutani, Structure development and properties of high-speed melt spun poly(butylene terephthalate)/poly(butylene adipate-co-terephthalate) bicomponent fibers. Polymer, 2006. 47(2): p. 611-616.

89. Perret, E., et al., Modified Crystallization in PET/PPS Bicomponent Fibers Revealed by Small-Angle and Wide-Angle X-ray Scattering. Macromolecules, 2013. 46(2): p. 440-448.

90. Salem, D.R., Draw-Induced Structure Development in Flexible-Chain Polymers, in Structure Formation in Polymeric Fibers, D.R. Salem, Editor. 2001, Carl Hanser Verlag: Munich. p. 118-184.

91. Emslie, C., Polymer Optical Fibers. Journal of Materials Science, 1988. 23(7): p. 2281-2293.

92. Murthy, N.S., et al., Structure of the Amorphous Phase in Oriented Polymers. Macromolecules, 1993. 26(7): p. 1712-1721.

93. Murthy, N.S., et al., Measurement of amorphous orientation in poly(ethylene terephthalate) fibers by X-ray diffraction and its significance. Journal of Applied Polymer Science, 1997. 64(7): p. 1363-1371.

94. Scherer, L.J., et al., Polymeric Optical Fiber Fabrics for Illumination and Sensorical Applications in Textiles, in The Fiber Society 2010 Spring Conference. 2010: Bursa, Turkey.

95. Scherer, L.J., et al., Polymeric Optical Fiber Fabrics for Medical Applications, in The Fiber Society 2012 Spring Conference. 2012: St. Gallen, Switzerland.

96. Fukazawa, Y., S. Kamiya, and M. Yamazaki, Optical Material. Japanese Patent JPS 6026024 (A), 1985-02-08.

97. Yamazaki, M., Industrialization and application development of cyclo-olefin polymer. Journal of Molecular Catalysis A: Chemical, 2004. 213(1): p. 81-87.

98. Hong, M.H. and J.L. White, Birefringence and mechanical property development in melt spinning cyclopolyolefin filaments. International Polymer Processing, 2002. 17(1): p. 53-59.

99. 3M™ Dyneon™ Products - Fluorothermoplastics - THV Polymer. [cited 2014-08-26; Available from: http://solutions.3m.com/wps/portal/3M/en_WW/3M_Dyneon/Home/Products/.

100. Oh, G.K. and T. Inoue, Dynamic birefringence of cyclic olefin copolymers. Rheologica Acta, 2005. 45(2): p. 116-123.

101. Teng, H., Overview of the Development of the Fluoropolymer Industry. Applied Sciences, 2012. 2(2): p. 496-512.

102. Hull, D.E., et al., THV Fluoroplastic, in Modern Fluoropolymers - High Performance Polymers for Diverse Applications, J. Scheirs, Editor. 1997, John Wiley & Sons Ltd: Cichester, England. p. 257-270.

103. Datasheets for ZEONEX and ZEONOR Cyclo Olefin Polymer (COP). [cited 2014-08-26; Available from: http://www.zeonex.com/datasheets.asp.

104. Yamazaki, M., Industrialization and application development of cyclo-olefin polymer. Journal of Molecular Catalysis a-Chemical, 2004. 213(1): p. 81-87.

105. Drobny, J.G., Technology of Fluoropolymers. 2nd ed. 2009, Boca Raton: CRC Press.

106. Hufenus, R., et al., Biodegradable Bicomponent Fibers from Renewable Sources: Melt-Spinning of Poly(lactic acid) and Poly[(3-hydroxybutyrate)-co-(3-hydroxyvalerate)]. Macromolecular Materials & Engineering, 2012. 297(1): p. 75-84.

107. ISO 2060:1994 - Textiles - Yarn from packages - Determination of linear density (mass per unit length) by the skein method. 1994, ISO International Organization for Standardization: Geneva, Switzerland.

108. Hall, M.M., et al., The Approximation of Symmetric X-Ray Peaks by Pearson Type VII Distributions. Journal of Applied Crystallography, 1977. 10: p. 66-68.

109. Migler, K.B., Sharkskin Instability in Extrusion, in Polymer Processing Instabilities - Control and Understanding, S.G. Hatzikiriakos and K.B. Migler, Editors. 2005, Marcel Dekker: New York. p. 121-159.

110. Hammer, A., Thermische Analyse von Polymeren; Teil 1: DSC an Thermoplasten, in Thermal Analysis UserCom. 2010, Mettler Toledo. p. 1-6.

111. Menczel, J.D., et al., Differential Scanning Calorimetry (DSC), in Thermal Analysis of Polymers: Fundamentals and Applications, J.D. Menczel and S. Swier, Editors. 2008, John Wiley & Sons, Inc.: Hoboken, NJ, USA. p. 7-239.

112. Alexander, L.E., X-Ray Diffraction Methods in Polymer Science. 1969, New York: John Wiley & Sons, Inc.

113. Schönhals, A. and F. Kremer, Amorphous Polymers, in Polymer Science: A Comprehensive Reference - Volume 1: Basic Concepts and Polymer Properties, K. Matyjaszewski and M. Möller, Editors. 2012, Elsevier B.V.: Amsterdam. p. 201-226.

114. Stribeck, N., X-Ray Scattering of Soft Matter. 2007, Berlin Heidelberg: Springer-Verlag.

115. Klug, H.P. and L.E. Alexander, X-Ray Diffraction Procedures. 2nd. ed. 1974, New York: John Wiley & Sons, Inc.

116. Rische, T., et al., Microstructure and morphology of cycloolefin copolymers. Macromolecules, 1998. 31(6): p. 1871-1874.

117. Kausch, H.-H. and J.L. Halary, Crazing and Fracture in Amorphous Polymers: Micromechanisms and Effect of Molecular Variables, in Mechanical Properties of Polymers based on Nanostructure and Morphology, G.H. Michler and F.J. Baltá-Calleja, Editors. 2005, Taylor & Francis: Boca Raton. p. 131-158.

118. Fourné, F., Synthetic Fibers. 1999, Munich: Carl Hanser Verlag.

119. Sumesh, P.T., T.P. Mathur, and U.S. Agarwal, Simulation of Polyester Melt Spinning with Axial Quench for Increasing Productivity. Journal of Applied Polymer Science, 2010. 116(5): p. 2541-2547.

120. Kumar, S. and A.K. Agrawal, How to produce PET POY at higher speeds? Chemical Fibers International, 2002. 52(6): p. 418-422.

121. Gröbe, A. and H. Herlinger, Method for reducing the yarn tension during the high-speed spinning of polyester. Chemiefasern/Textilindustrie, 1984. 34/86(4): p. E29.

122. Rosato, D.V., et al., Plastics engineering, manufacturing and data handbook. 2001: Kluwer Academic Publishers. 2006.

123. Perepelkin, K.E., The effect of the liquid and gas phase transitions on the extrusion stability in man-made fibre and film processes. Fibre Chemistry, 1972. 3(2): p. 115-123.

124. Wagner, M., Thermal Analysis in Practice - Mettler Toledo Collected Applications. 2009, Schwerzenbach, Switzerland: Mettler Toledo AG, Analytical.

125. Krehel, M., et al., Development of a luminous textile for reflective pulse oximetry measurements. Biomedical Optics Express, 2014. 5(8): p. 2537-2547.

126. Scanaill, C.N., et al., A review of approaches to mobility telemonitoring of the elderly in their living environment. Annals of Biomedical Engineering, 2006. 34(4): p. 547-563.

127. Post, E.R., et al., E-broidery: Design and fabrication of textile-based computing. Ibm Systems Journal, 2000. 39(3-4): p. 840-860.

128. Ziemann, O., et al., POF-Handbook. 2008, Berlin: Springer.

129. Pola, T. and J. Vanhala, Textile electrodes in ECG measurement. Proceedings of the 2007 International Conference on Intelligent Sensors, Sensor Networks and Information Processing, 2007: p. 635-639.

130. Krehel, M., et al., Characterization of Flexible Copolymer Optical Fibers for Force Sensing Applications. Sensors, 2013. 13(9): p. 11956-11968.

131. Balas, C., Review of biomedical optical imaging-a powerful, non-invasive, non-ionizing technology for improving in vivo diagnosis. Measurement Science & Technology, 2009. 20(10).

132. Narbonneau, F., et al., Smart Textile Embedding Optical Fibre Sensors for Healthcare

Monitoring during MRI. Advances in Science and Technology, 2008. Vol. 60: p. 134-143.

133. Ding, J.Y., M.R. Shahriari, and G.H. Sigel, Fiber Optic Ph Sensors Prepared by Sol-Gel Immobilization Technique. Electronics Letters, 1991. 27(17): p. 1560-1562.

134. Witt, J., et al., Medical Textiles With Embedded Fiber Optic Sensors for Monitoring of Respiratory Movement. Ieee Sensors Journal, 2012. 12(1): p. 246-254.

135. Rantala, J., J. Hannikainen, and J. Vanhala, Fiber optic sensors for wearable applications. Personal and Ubiquitous Computing, 2011. 15(1): p. 85-96.

136. Hanada, E., The electromagnetic environment of hospitals: how it is affected by the strength of electromagnetic fields generated both inside and outside the hospital. Ann Ist Super Sanita, 2007. 43(3): p. 208-17.

137. Edlich, R.F., et al., Pressure ulcer prevention. J Long Term Eff Med Implants, 2004. 14(4): p. 285-304.

138. Woodgate, R. and L.J. Kristjanson, A young child's pain: How parents and nurses 'take care'. International Journal of Nursing Studies, 1996. 33(3): p. 271-284.

139. Hufenus R., S.L.J., Hegemann D., Reifler F.A., Gaan, S., Developing base technologies for tomorrow's smart textiles. 18th International conference on composite materials, 2011.

140. Toth, B., A. Becker, and B. Seelbach-Gobel, Oxygen saturation in healthy newborn infants immediately after birth measured by pulse oximetry. Arch Gynecol Obstet, 2002. 266(2): p. 105-7.

141. Rheineck-Leyssius, A.T. and C.J. Kalkman, Influence of pulse oximeter settings on the frequency of alarms and detection of hypoxemia - Theoretical effects of artifact rejection, alarm delay, averaging, median filtering or a lower setting of the alarm limit. Journal of Clinical Monitoring and Computing, 1998. 14(3): p. 151-156.

142. Isbister, J.P., Physiology and pathophysiology of blood volume regulation. Transfusion Science, 1997. 18(3): p. 409-423.

143. Venema, B., et al., Advances in reflective oxygen saturation monitoring with a novel in-ear sensor system: Results of a human hypoxia study. IEEE Transactions on Biomedical Engineering, 2012. 59(7): p. 2003-2010.

144. Svanberg, E.K., et al., Physiological influence of basic perturbations assessed by non-invasive optical techniques in humans. British Journal of Anaesthesia, 2012. 108: p. 272-273.

145. Wolf, U., et al., Localized irregularities in hemoglobin flow and oxygenation in calf muscle in patients with peripheral vascular disease detected with near-infrared spectrophotometry. Journal of Vascular Surgery, 2003. 37(5): p. 1017-1026.

146. Wolf, U., et al., Regional differences of Hemodynamics and oxygenation in the human calf muscle detected with near-infrared spectrophotometry. Journal of Vascular and Interventional Radiology, 2007. 18(9): p. 1094-1101.

147. Dassel, A.C.M., et al., Reflectance pulse oximetry at the forehead of newborns: The influence of varying pressure on the probe. Journal of Clinical Monitoring, 1996. 12(6): p. 421-428.

148. Rahim, N.A.A., et al., Conjugated Polymer Nanoparticles for Two-Photon Imaging of Endothelial Cells in a Tissue Model. Advanced Materials, 2009. 21(34): p. 3492-+.

149. Van de Louw, A., et al., Accuracy of pulse oximetry in the intensive care unit. Intensive Care Medicine, 2001. 27(10): p. 1606-1613.

150. Wang, A.B., et al., Optical Fiber Pressure Sensor Based on Photoelasticity and Its Application. Journal of Lightwave Technology, 1992. 10(10): p. 1466-1472.

151. Urban, F., et al., Design of a Pressure Sensor Based on Optical Fiber Bragg Grating Lateral Deformation. Sensors, 2010. 10(12): p. 11212-11225.

152. De Jonckheere, J., et al. OFSETH: Optical Fibre Embedded into technical Textile for Healthcare, an efficient way to monitor patient under magnetic resonance imaging. in 29th Annual International Conference of the IEEE-Engineering-in-Medicine-and-Biology-Society. 2007. Lyon, FRANCE: Ieee.

153. Witt, J., M. Schukar, and K. Krebber, Medicinal Textiles with Integrated Polymer-Optical Fibers for Respiration Monitoring. Tm-Technisches Messen, 2008. 75(12): p. 670-677.

154. Zhang, Z.C., et al., A Film Pressure Sensor Based on Optical Fiber Bragg Grating. Smart Sensor Phenomena, Technology, Networks, and Systems 2010, 2010. 7648.

155. Tjin, S.C., et al., A pressure sensor using fiber Bragg grating. Fiber and Integrated Optics, 2001. 20(1): p. 59-69.

156. Kaczmarek, T. and Z. Kaczmarek, Modified Fiber Bragg grating pulse pressure sensor - art. no. 66081E. Lightguides and Their Applications III, 2007. 6608: p. E6081-E6081.

157. Tanaka, N., Y. Okabe, and N. Takeda, Temperature-compensated strain measurement using fiber Bragg grating sensors embedded in composite laminates. Smart Materials & Structures, 2003. 12(6): p. 940-946.

158. Guan, B.O., et al., Discrimination between strain and temperature with a single fiber Bragg grating. Microwave and Optical Technology Letters, 2002. 33(3): p. 200-202.

159. Rothmaier, M., Textile Pressure Sensor Made of Flexible Plastic Optical fibers. Sensors, 2008: p. 4319-4329.

160. Lymberis, A. and A. Dittmar, Advanced wearable health systems and applications. IEEE Eng. Med. Biol. Mag, 2007. May/June 2007: p. 29-399.

161. Meyer, J., P. Lukowicz, and G. Troster, Textile pressure sensor for muscle activity and motion detection. Tenth Ieee International Symposium on Wearable Computers, Proceedings, 2006: p. 69-72.

162. Lubliner, J., Plasticity theory. 2008, New York: Macmillan Publishing.

163. Cretikos, M.A., et al., Respiratory rate: the neglected vital sign. Medical Journal of Australia, 2008. 188(11): p. 657-659.

164. De Mayo, T., et al., Breathing type and body position effects on sternocleidomastoid and suprahyoid EMG activity. Journal of Oral Rehabilitation, 2005. 32(7): p. 487-494.

165. Krieger, B., et al., Continuous Noninvasive Monitoring of Respiratory Rate in Critically Ill Patients. Chest, 1986. 90(5): p. 632-634.

166. Dziuda, L., et al., Fiber Bragg grating-based sensor for monitoring respiration and heart activity during magnetic resonance imaging examinations. J Biomed Opt, 2013. 18(5): p. 57006.

167. Ł. Dziuda, M.K., and F. W. Skibniewski, Fiber Bragg grating strain sensor incorporated to monitor patient vital signs during MRI. IEEE Sens. J. , 2013: p. 4986-4991.

168. Chen, Z., et al., Simultaneous measurement of breathing rate and heart rate using a microbend multimode fiber optic sensor. J Biomed Opt, 2014. 19(5): p. 057001.

169. A. T. Augousti, F.-X.M., and J. Mason, The use of a figure-of-eight coil for fibre optic respiratory plethysmography: geometrical analysis and experimental characterisation. Opt. Fiber Technol., 2005: p. 346–360.

170. A. T. Augousti, F.-X.M., and J. Mason, Improved fiber-optic respiratory monitoring using a figure-of-eight coil. Physiol. Meas, 2005: p. 585-590.

171. W. J. Yoo, K.W.J., J. K. Seo, J. Y. Heo, J. S. Moon, J. Y. Park, and B. Lee, Development of respiration sensors using plastic optical fiber for respiratory monitoring inside MRI system. J. Opt. Soc. Korea, 2010: p. 235–239.

172. Krehel, M., et al., Characterization of flexible copolymer optical fibers for force sensing applications. Sensors (Basel), 2013. 13(9): p. 11956-68.

173. D. G. Altman, J.M.B., Measurement in Medicine: The Analysis of Method Comparison Studies. Journal of the Royal Statistical Society., 1983. 32: p. 307-317.

174. Dahl, W.Q.L.M.P.C.T.B.M., Comprehensive Medical Assisting: Administrative and Clinical Competencies. Cengage Learning. 2009. 573.

175. Schwartzstein RM, A.L.D.I.M.R., Broaddus VC, Martin TR, et al,, Murray and Nadel's Textbook of Respiratory Medicine. 5th ed. 2010, Philadelphia.

176. Allen, J.B., Short-Term Spectral Analysis, Synthesis, and Modification by Discrete Fourier-Transform. Ieee Transactions on Acoustics Speech and Signal Processing, 1977. 25(3): p. 235-238.